PROTUBERANCE HEATIN
TEST PROGRA

FEBRUARY 1966

DOUGLAS REPORT SM-47407

MISSILE & SPACE SYSTEMS DIVISION
DOUGLAS AIRCRAFT COMPANY, INC.
SANTA MONICA/CALIFORNIA

DOUGLAS

PROTUBERANCE HEATING TEST PROGRAM

FEBRUARY 1966
DOUGLAS REPORT SM-47497

PREPARED BY: W.D. SIEKER
AERO/THERMODYNAMICS SECTION

PREPARED FOR:
NATIONAL AERONAUTICS AND
SPACE ADMINISTRATION
UNDER NASA CONTRACT NAS7-101

APPROVED BY: A. P. O'NEAL
DIRECTOR, SATURN DEVELOPMENT ENGINEERING

DOUGLAS MISSILE & SPACE SYSTEMS DIVISION
SPACE SYSTEMS CENTER — HUNTINGTON BEACH, CALIFORNIA

PRECEDING PAGE BLANK NOT FILMED

ABSTRACT

This report presents the results of the Protuberance Heating Test Program. Four general protuberance shapes on a flat plate were tested. Presentation and evaluation of the data both on the protuberance and in the wake regions are made.

The test program is an extension of the General Protuberance Heat Transfer Test. The additional series of tests was conducted to define the extent of wake heating and to assess the effects of Reynolds number variation on heating both on and around the protuberances.

The protuberance models were mounted near the forward end of a six-foot instrumented test plate with stringers that simulated interstage and skirt structure of the Saturn S-IVB stage.

The tests were performed at Mach numbers of 2.49, 3.51, and 4.44. Reynolds numbers per foot of 3×10^6 and 1.5×10^6 were used for the two lower Mach numbers and 3×10^6 for a Mach number of 4.44. The test Mach numbers simulated the Saturn S-IVB flight conditions during the most severe aerodynamic heating period. The test Reynolds numbers were somewhat higher than the flight values, but lower values could not be used because of tunnel and instrumentation limitations.

Oil flow runs were made on two representative models at various combinations of Mach number and Reynolds number to help define the extent of wake heating.

The data are presented in the form of ratios of local heat transfer coefficient to flat plate (with stringers) heat transfer coefficient in undisturbed flow ($h_c/h_{co,s}$).

The results of the test show that wake heating effects are still present 25 diameters downstream of the body. It is not known at this time where normal flat plate heating returns. The results also show that wake heat transfer coefficient ratios ($h_c/h_{co,s}$) increase with increasing Mach number and also increase with decreasing Reynolds number. The disturbance effects in the wake region are shown to be dependent on protuberance size within the boundary layer and on the bluntness of the afterbody.

Wake heating data on a smooth plate (without stringers) are included. These runs were not specified in the test plan; therefore, calibration of the smooth plate was not performed.

D E S C R I P T O R S

Heat Transfer

Protuberance

Saturn

Test

Wake

Wind Tunnel

PREFACE

The Protuberance Heating Test Program was conducted for the George C. Marshall Space Flight Center under Contract No. NAS 7-101. The test program was requested by Engineering Change Proposal No. X066. Authorization was made by Change Order 558. The Test Plan was presented in Reference 1.

The three phases of testing (calibration, wake heating, and oil flow) were successfully completed with the accomplishment of all primary and secondary objectives specified in the test plan.

The information obtained from these tests supplements the information gained from the General Protuberance Heat Transfer Test (Reference 2) that was performed in April, 1964.

This report is the presentation and evaluation of the data obtained from the Protuberance Heating Test Program.

TABLE OF CONTENTS

Paragraph		Page
1.	INTRODUCTION	1
1.1	The Protuberance Heating Test Program.	1
1.2	Test Objectives.	1
1.3	Facility Installation and Schedule	2
2.	TEST PROCEDURE	3
3.	MODEL DESCRIPTION.	3
3.1	Test Plate	3
3.2	Stringers.	4
3.3	Models	4
3.4	Instrumentation.	5
4.	RUN SCHEDULE	5
5.	RESULTS AND DISCUSSION	6
5.1	Calibration Runs	6
5.2	Wake Heating Runs.	6
5.2.1	Heat Transfer Data for the Test Plate ($h_c/h_{co,s}$) and on the Models (h_c).	6
5.2.2	Wake Heating Along the Protuberance Centerline	7
5.2.3	Lateral Variation of $h_c/h_{co,s}$ in the Wake Region	11
5.2.4	Heating Effects on the Surfaces of Protuberances	13
5.3	Oil Flow Runs.	17
5.3.1	Oil Flow Photographs	17
5.3.2	Heating Profiles Compared to Observed Wake Patterns.	19
5.4	Pressure Coefficient Distributions in the Wake Region.	19
5.5	Data Repeatability and Accuracy.	20
5.5.1	Correlation of Theory and Data	22

TABLE OF CONTENTS (Continued)

Paragraph		Page
6.	CONCLUSIONS	24
	REFERENCES	26
	APPENDIX	135

LIST OF ILLUSTRATIONS

Figure		Page
1	General Protuberance Shape	32
2	Protuberance Models Basic Configuration (Side Views)	33
3	Langley Protuberance Heating Test-Sketch of Test Plate Model.	34
4	Typical Heat Bump Total Temperature Histories.	35
	MODEL DRAWINGS AND PHOTOGRAPHS	
5	Test Plate - Langley UPWT Test	36
6	Protuberance Model No. 2 - Langley UPWT Test	38
7	Protuberance Model No. 5 - Langley UPWT Test	40
8	Protuberance Model No. 9 - Langley UPWT Test	42
9	Protuberance Model No. 10 - Langley UPWT Test.	46
	LANGLEY PROTUBERANCE HEATING TEST-HEAT TRANSFER COEFFICIENTS AND PRESSURE COEFFICIENTS; CALIBRATION RUNS	
10	Plate With Stringers; M = 2.49, Re/Ft = 3.0439×10^6	48
11	Plate With Stringers; M = 2.49, Re/Ft = 1.5727×10^6	49
12	Plate With Stringers; M = 3.51, Re/Ft = 2.9434×10^6 (temperature only)	50
13	Plate With Stringers; M = 3.51, Re/Ft = 1.2896×10^6 (temperature only)	51
14	Plate With String ; M = 3.51, Re/Ft = 1.700×10^6 (pressure only).	52
15	Plate With Stringers; M = 4.44, Re/Ft = 3.1985×10^6	53
16	Smooth Plate; M = 2.49, Re/Ft = 3.0312×10^6 (taken from General Protuberance Heat Transfer Test).	54
17	Smooth Plate; M = 3.51, Re/Ft = 2.9667×10^6 (taken from General Protuberance Heat Transfer Test).	55
18	Smooth Plate; M = 4.44, Re/Ft = 3.2018×10^6 (taken from General Protuberance Heat Transfer Test).	56

Figure

Page

LANGLEY PROTUBERANCE HEATING TEST-HEAT TRANSFER COEFFICIENT RATIOS ($h_c/h_{co,n}$) AND PRESSURE COEFFICIENTS ON PLATE WITH STRINGERS AND HEAT TRANSFER COEFFICIENTS (h_c) ON MODEL NO. 9

19-20 M = 2.49 and Re/Ft = 3.0318×10^6. 57-58

21-22 M = 2.49 and Re/Ft = 1.5840×10^6. 59-60

23-24 M = 3.51 and Re/Ft = 2.9514×10^6. 61-62

25-26 M = 3.51 and Re/Ft = 1.5532×10^6. 63-64

27-28 M = 4.44 and Re/Ft = 3.2185×10^6. 65-66

LANGLEY PROTUBERANCE HEATING TEST-HEAT TRANSFER COEFFICIENT RATIOS ($h_c/h_{co,s}$) AND PRESSURE COEFFICIENTS ON PLATE WITH STRINGERS AND HEAT TRANSFER COEFFICIENTS (h_c) ON MODEL NO. 2

29-30 M = 2.49 and Re/Ft = 3.0695×10^6. 67-68

31-32 M = 2.49 and Re/Ft = 1.5705×10^6. 69-70

33-34 M = 3.51 and Re/Ft = 2.9789×10^6. 71-72

35-36 M = 4.44 and Re/Ft = 3.2592×10^6. 73-74

LANGLEY PROTUBERANCE HEATING TEST-HEAT TRANSFER COEFFICIENT RATIOS ($h_c/h_{co,s}$) AND PRESSURE COEFFICIENTS ON PLATE WITH STRINGERS AND HEAT TRANSFER COEFFICIENTS (h_c) ON MODEL NO. 10

37-38 M = 2.49 and Re/Ft = 3.0394×10^6. 75-76

39-40 M = 2.49 and Re/Ft = 1.5546×10^6. 77-78

41-42 M = 3.51 and Re/Ft = 2.9698×10^6. 79-80

43-44 M = 3.51 and Re/Ft = 1.5614×10^6. 81-82

45-46 M = 4.44 and Re/Ft = 3.1722×10^6. 83-84

Figure | Page

LANGLEY PROTUBERANCE HEATING TEST-HEAT TRANSFER COEFFICIENT RATIOS ($h_c/h_{co,B}$) AND PRESSURE COEFFICIENTS ON PLATE WITH STRINGERS AND HEAT TRANSFER COEFFICIENTS (h_c) ON MODEL NO. 5

47-48 M = 2.49 and Re/Ft = 3.0264 x 10^6 86-87

49-50 M = 2.49 and Re/Ft = 1.5586 x 10^6 87-88

51-52 M = 3.51 and Re/Ft = 2.9351 x 10^6 89-90

53-54 M = 3.51 and Re/Ft = 1.5426 x 10^6 91-92

55-56 M = 4.44 and Re/Ft = 3.1848 x 10^6 93-94

LANGLEY PROTUBERANCE HEATING TEST-HEAT TRANSFER COEFFICIENTS (h_c), RATIOS (h_c/h_{co}) AND PRESSURE COEFFICIENTS ON THE SMOOTH PLATE WITH MODEL NO. 9 ATTACHED

57 M = 2.49 and Re/Ft = 3.0529 x 10^6 95

58 M = 2.49 and Re/Ft = 1.5578 x 10^6 96

59 M = 3.51 and Re/Ft = 2.9475 x 10^6 97

60 M = 3.51 and Re/Ft = 1.5519 x 10^6 98

61 M = 4.44 and Re/Ft = 3.1983 x 10^6 99

DOWNSTREAM HEAT TRANSFER COEFFICIENT RATIOS ($h_c/h_{co,s}$) ALONG THE PROTUBERANCE CENTERLINE

62 Effects of Mach No. and Reynolds No. Variation on Heating Behind Model No. 9 100

63 Effects of Mach No. and Reynolds No. Variation on Heating Behind Model No. [illegible] 101

64 Effects of Mach No. and Reynolds No. Variation on Heating Behind Model No. 10. 102

65 Effects of Mach No. and Reynolds No. Variation on Heating Behind Model No. 5 103

LATERAL HEAT TRANSFER COEFFICIENT RATIOS ($h_c/h_{co,B}$) IN THE TURBULENT WAKE REGION

66 Effects of Mach No. and Reynolds No. Variation on Heating Behind Model No. 9 104

Figure		Page
67	Effects of Mach No. and Reynolds No. Variation on Heating Behind Model No. 2	105
68	Effects of Mach No. and Reynolds No. Variation on Heating Behind Model No. 10.	106
69	Effects of Mach No. and Reynolds No. Variation on Heating Behind Model No. 5	107
	THE RATIO OF MODEL HEAT TRANSFER COEFFICIENT TO FLAT PLATE HEAT TRANSFER COEFFICIENT	
70	Axial and Cross-Sectional Distribution on Model No. 9. . .	108
71	Axial and Cross-Sectional Distribution on Model No. 2. . .	110
72	Axial and Cross-Sectional Distribution on Model No. 10 . .	112
73	Axial and Cross-Sectional Distribution on Model No. 5. . .	114
74	Model No. 9 at M = 2.49 and Re/Ft = 1.5×10^6.	116
75	Model No. 9 at M = 2.49 and Re/Ft = 3×10^6.	117
76	Model No. 9 at M = 3.51 and Re/Ft = 3×10^6.	118
77	Model No. 9 at M = 4.44 and Re/Ft = 3×10^6.	119
78	Model No. 5 at M = 3.51 and Re/Ft = 3×10^6, Upstream Photograph	120
79	Model No. 5 at M = 3.51 and Re/Ft = 3×10^6, Downstream Photograph	121
	LATERAL HEAT TRANSFER COEFFICIENT RATIOS ($h_c/h_{co,s}$) SUPERIMPOSED ON OBSERVED OIL FLOW PATTERNS	
80	Model No. 9 at M = 2.49, 3.51, and 4.44 and Re/Ft = 3×10^6.	122
81	Model No. 5 at M = 3.51 and Re/Ft = 3×10^6.	123
	PRESSURE COEFFICIENTS IN THE WAKE REGION	
82	Model No. 9	124
83	Model No. 2	125

Figure		Page
84	Model No. 10	126
85	Model No. 5.	127
	COMPARISON OF THEORY AND DATA	
86	Test Plate	128
87	Centerline Surfaces of Model No. 9	129
88	Centerline Surfaces of Model No. 2	130
89	Centerline Surfaces of Model No. 10	131
90	Centerline Surfaces of Model No. 5	132

LIST OF TABLES

Table		Page
1	Location of Instrumentation Thermocouples and Pressure Taps - Langley Test	27
2	Langley Protuberance Heating Test-Run Schedule	30

1. INTRODUCTION

1.1 The Protuberance Heating Test Program

Following the first series of General Protuberance Heat Transfer Tests (Reference 2) at the Langley Research Center, Unitary Plan Wind Tunnel, it became apparent that additional tests would be desirable to further define the effects of wake heating and to determine the effects of Reynolds number variation on heating both on and around protuberances. The previous series of wind tunnel tests had given wake heating data up to ten protuberance diameters downstream where heating effects of the order of 1.1 times normal flat plate heating were seen to exist.

1.2 Test Objectives

The primary purpose of this test was to define the wake heating region behind various shaped protuberances so that structural temperatures and insulation requirements for Saturn stages could more accurately be determined. Secondary objectives were to define the effects of boundary layer immersion on protuberance forebody heating, assess the effects of Reynolds number variation on heating both on and around protuberances and determine flow field patterns using oil flow techniques.

The four model configurations tested (figures 1 and 2) were chosen to most nearly satisfy the specified test objectives.

1.3 Facility Installation and Schedule

The four test models and test plate were the same as those used in the General Protuberance Heat Transfer Test (Reference 2). The plate was installed on the tunnel door as had been done for previous testing (References 2 and 3). To effectively lengthen the instrumented wake heating region, the following modifications were made:

a. The model attach point was moved forward to the back-up plate, 36.4 inches from the original position on the test plate.

b. The stringers were extended 24 inches forward of the test plate onto the tunnel sidewall.

System continuity checks revealed that approximately 30 percent of the thermocouples were inoperative. Corrosion of the iron wires of the thermocouples during the one-year storage period between tests was responsible for the failure of the temperature sensors. All of the test plate and model thermocouples were reworked to insure the integrity of the instrumentation system.

The test plate was installed in the tunnel on 23 July 1965. Testing was started on 26 July 1965, and completed on 29 July 1965. The test models and stringers were removed from the tunnel and shipped back to Douglas, Santa Monica. The test plate was left at the Unitary Plan Wind Tunnel.

The entire Protuberance Heating Test Program proceeded very smoothly from the time of model delivery and test setup through the completion of testing.

2. TEST PROCEDURE

The instrumented test plate used in the previous series of tests was installed flush on the tunnel sidewall. The various models were attached to the forward end of the plate for testing (figure 3).

The method used for determining heat transfer coefficients (Reference 4) is outlined in detail in the Appendix. The method basically consisted of determining the heat transfer coefficient as a function of time by measuring the transient wall temperature (outside skin of the test plate) during a period in which the wall temperature was increasing. The total temperature differential for heat transfer testing was obtained by bypassing the tunnel cooling system. The rise in total temperature took place over a period of several seconds and was dependent on the Mach number. As the total temperature rose, the automatic data recording system was activated. The thermocouple readings were recorded after the peak total temperature was reached. Typical heat bumps for the three test Mach numbers are given in figure 4.

3. MODEL DESCRIPTION

3.1 Test Plate

The test plate was a flat laminated plate 60 inches long and 40.75 inches wide. as shown in figure 5. It consisted of a 0.047 inch stainless steel (347 cres) test surface insulated by a 0.375 inch thick hexagonal fiberglass honeycomb section bonded to a 0.125 inch stainless steel (347 cres) waffle backing plate. The plate was mounted flush with the tunnel wall on the

access door of the test section and was instrumented with 123 thermocouples and 12 pressure orifices.

3.2 Stringers

Ten removable stringers of sheet laminated phenolic, a material of low thermal conductivity, were spaced 2 inches apart (on centers) on the test plate surface. The stringers were 0.5 inch square with leading and trailing faces scarfed at an angle of 30 degrees with the plate surface. The stringers extended forward approximately 24 inches from the leading edge of the plate and were attached to the tunnel sidewall. Two of the stringers were channeled to allow for the routing of the model instrumentation wiring.

3.3 Models

The models were electroformed shells of nickel, 0.040 inch thick, with laminated phenolic bases for insulation. The following four models, shown with instrumentation locations in figures 6 through 9, were used in the test:

Model No.	Forebody Angle	Centerbody Height, Cal*	Centerbody Length, Cal*	Afterbody Angle
2(M_2)	15°	1.0	2.5	30°
5(M_5)	15°	1.0	2.5	90°
9(M_9)	30°	0.5	0.5	30°
10(M_{10})	30°	2.0	2.0	30°

*1 caliber = 5.0 inches

3.4 Instrumentation

Temperature measurements on the models and test plate were obtained as a function of time by means of thermocouples. The thermocouples were iron-constantan potted with pure tin into 0.030 inch diameter holes. The wires were insulated with No. 26 gage nylon. Pressure taps on the plate were 0.0625 inch O.D. by 0.012 inch wall stainless steel tubing.

Table 1 presents the locations of instrumentation for the plate and models. Dimensions are given in relation to the model attach point.

4. RUN SCHEDULE

The Protuberance Heating Test run schedule is presented in table 2.

The tunnel conditions (total pressure and temperature) measured after the heat bumps are listed for the various Mach numbers and Reynolds numbers:

Mach Number	Reynolds Number x 10^{-6}	P_T psfa	T_T °R
2.49	3.0439	3225	720
2.49	1.5727	1659	717
3.51	2.9434	5373	713
3.51	1.2896	2356	712
4.44	3.1085	8657	683

5. RESULTS AND DISCUSSION

5.1 Calibration Runs

The calibration data obtained from the flat plate with stringer configurations are given in figures 10 through 15 for the various combinations of Mach numbers and Reynolds numbers tested. The data from three calibration runs for the flat plate without stringers are included in figures 16, 17 and 18. These data are taken from the General Protuberance Heat Transfer Test (Reference 2). They are used as reference values to determine the flat plate heat transfer coefficient ratios with Model No. 9 on the smooth test plate (Runs 6-4 through 6-8). Calibration runs were made only on the test plate with stringers since all of the scheduled protuberance runs specified that configuration.

5.2 Wake Heating Runs

5.2.1 Heat Transfer Data for the Test Plate ($h_c/h_{co,s}$) and on the Models (h_c)

Heating effects both on the model surfaces and on the test plate surface in the wake region are presented in normal view layout in figures 19 through 56. Pressure coefficients on the test plate are also given for the entire range of Mach numbers and Reynolds numbers tested. The heating data on the models are presented in terms of local surface heat transfer coefficient, h_c. The heating data in the wake region are given as the ratio of surface heat transfer coefficient to flat plate (with stringers) heat transfer coefficient, $(h_c/h_{co,s})$.

Wake heating and pressure coefficient data are presented in figures 57 through 61 for Model No. 9 on the smooth test plate. These five runs were made to provide supplementary data. The data from the runs made at the high Reynolds number (3×10^6/ft) are presented in terms of h_c/h_{co} with the reference values of h_{co} taken from the data obtained during the General Protuberance Heat Transfer Tests (Reference 2, Runs: 1-1, 1-2, and 1-3). The data from the runs made at the low Reynolds number (1.5×10^6/ft) are presented as h_c.

It is noted that the heat transfer coefficient ratios tend to be somewhat higher in the wake region for the smooth plate without stringers.

5.2.2 Wake Heating Along the Protuberance Centerline

A presentation of the wake heating data along the centerline of the protuberances showing the effects of Mach number and Reynolds number is made for the four models in figures 62 through 65. The data are presented in the dimensionless form of $h_c/h_{co,s}$ versus x/d (distance behind the protuberance/protuberance diameter).

The size of the test models and stringers with respect to the boundary layer thickness (z/δ) simulates the range of Saturn vehicle protuberance z/δ's.

The test Mach numbers correspond to the local Saturn V/S-IVB flight values during the period of significant aerodynamic heating. Test Reynolds numbers are substantially higher than the flight values through most of the aerodynamic heating regime. Tunnel and instrumentation limitations prevented

a closer simulation of Reynolds number. The relationship between the flight and test parameters is shown below:

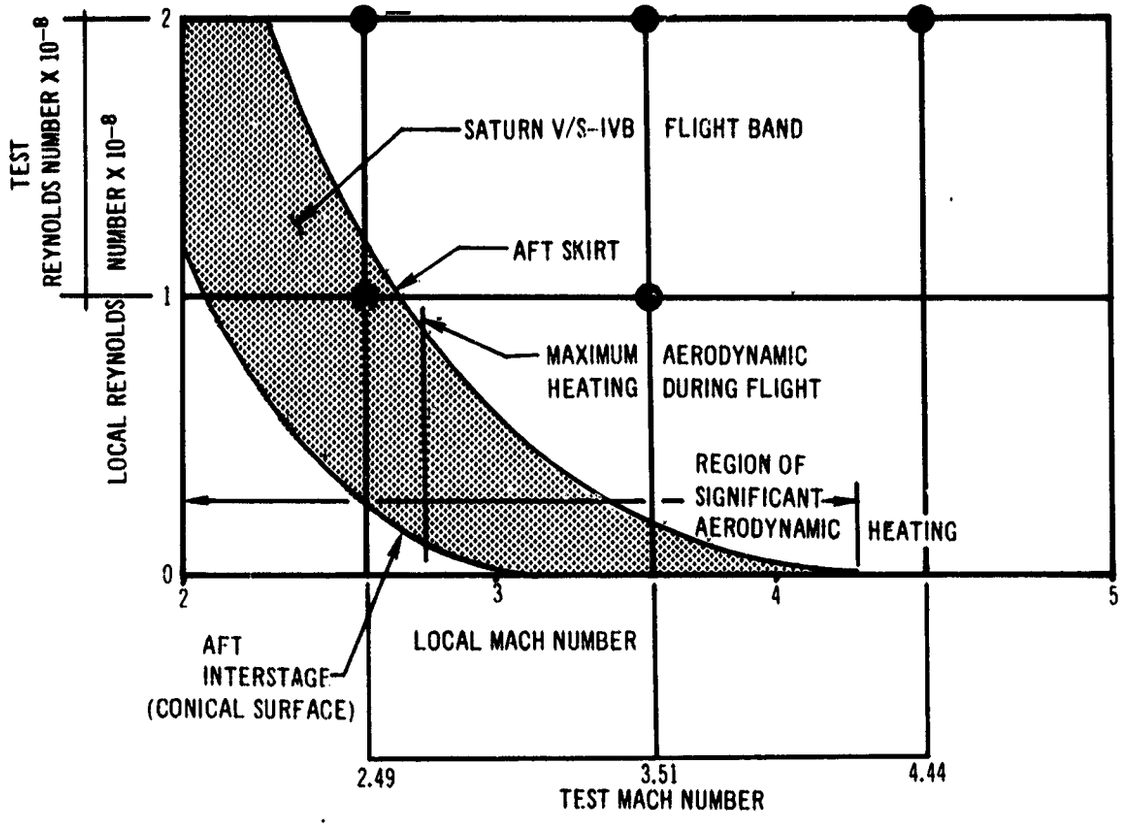

It has been determined from the test data that $h_c/h_{co,s}$ in the wake region after the point of flow reattachment generally varies directly with Mach number and inversely with Reynolds number. The local Reynolds numbers on the S-IVB stage are from 15 to 85 percent lower than the lowest test Reynolds number (Re = 10^8 or Re/ft = 1.5 x 10^6) at the time of maximum aerodynamic heating. Using a linear relationship, this represents a 5 to 20 percent increase in $h_c/h_{co,s}$. The divergence between flight and test Reynolds numbers increases after the point of maximum aerodynamic heating; however, the percentage increase of $h_c/h_{co,s}$ (between the high and

low test Reynolds numbers) diminishes with increasing Mach number. The extent of the increase in $h_c/h_{co,s}$ due to flight and test Reynolds number variation over the entire aerodynamic heating regime can only be estimated. As an example, the Saturn V/S-IVB $h_c/h_{co,s}$ values would be increased 5 to 20 percent (depending on the location being analyzed on the S-IVB stage) over the values determined at M = 2.40 and Re/ft = 1.5×10^6.

Additional wake heating data at Mach numbers 2.49 and 3.51 would be useful in order to better determine the extent of the increased $h_c/h_{co,s}$ due to Reynolds number reduction.

5.2.2.1 Model No. 9 ($M_9 + P_1$)

It can be seen in figure 62 that the $h_c/h_{co,s}$ ratios reach a maximum value just aft of the conical afterbody of Model No. 9. The decrease in $h_c/h_{co,s}$ is small for x/d greater than 10. At M = 4.44, heating up to 1.6 times the flat plate value still exists 23 diameters downstream.

The trend of increased $h_c/h_{co,s}$ with an increase of Mach number and a decrease in Reynolds number is apparent. However, it is noted that as the Mach number increases, the incremental rise in $h_c/h_{co,s}$ due to the Reynolds number variation decreases.

5.2.2.2 Model No. 2 ($M_2 + P_1$)

Contrary to the trend observed for Model No. 9, there is a sharp decrease in $h_c/h_{co,s}$ with Mach number just downstream of the afterbody of Model No. 2 (figure 63). At approximately three diameters downstream, the heating approaches flat plate values for M = 3.51 and 4.44. At six diameters

downstream, the heating approaches the same direct relationship to Mach number as was observed with Model No. 9.

The variation in $h_c/h_{co,s}$ between Model No. 9 and No. 2 results from the differences of protuberance height (z) and boundary layer height (δ). For Model No. 9 and No. 2, z/δ = 0.42 and 0.83, respectively. Data from Reference 2 have shown that forebody angle has little effect on wake heating.

5.2.2.3 Model No. 10 ($M_{10} + P_1$)

Values of $h_c/h_{co,s}$ peak directly behind the afterbody of Model No. 10 in inverse relation to Mach number (figure 64). At 3.5 diameters aft, the direct relationship of Mach number to $h_c/h_{co,s}$ exists as was noted in the previous models. It is noted that the $h_c/h_{co,s}$ increase due to the reduction in Reynolds number (Re/ft = 1.5×10^6) approaches 25 percent for M = 2.49, but the incremental increase of $h_c/h_{co,s}$ diminishes as the Mach number increases.

The effect of protuberance height on the magnitude of wake $h_c/h_{co,s}$ is apparent. Values of $h_c/h_{co,s}$ in the wake region behind Model No. 10 (z/δ = 1.66 inches) are up to 150 percent higher than the values in the wake region of Model No. 9 (z/δ = 0.42).

5.2.2.4 Model No. 5 ($M_5 + P_1$)

The heating in the separated region directly behind the blunt afterface of Model No. 5 (figure 65) is as low as 20 percent of flat plate values. The pressure returns to freestream values at 3 to 4 diameters downstream

accompanied by an increase in wake heating. The direct relationship of $h_c/h_{co,s}$ to Mach number exists after one diameter downstream, but the heating levels for the various test parameters are somewhat lower than those for the conical afterbody configurations.

5.2.3 Lateral Variation of $h_c/h_{co,s}$ in the Wake Region

The lateral variations of $h_c/h_{co,s}$ in the wake region (figures 66 through 69) show the effects of Mach number and Reynolds number for the four model configurations. The profiles of $h_c/h_{co,s}$ are given as functions of x/d and y/d (downstream distance/model diameter and lateral distance from centerline/model diameter, respectively). It is noted that the lateral disturbance patterns vary inversely with z/δ (model height/ boundary layer height). This is particularly evident at the highest Mach number.

5.2.3.1 Model No. 9 ($M_9 + P_1$)

The disturbed heating effect in the wake region of Model No. 9 (figure 66) is restricted to a relatively narrow width ($y/d < 1$) for the test Mach numbers of 2.49 and 3.51. The disturbance pattern widens substantially at the highest test Mach number, 4.44, and appears to extend beyond the lateral limits of the instrumentation in the wake region up to 16 diameters downstream. For y/d greater than one, the effect of Reynolds number on $h_c/h_{co,s}$ is negligible.

5.2.3.2 Model No. 2 ($M_2 + P_1$)

The disturbed heating effect in the wake region of Model No. 2 extends approximately 2.5 diameters laterally from the model centerline for all Mach numbers (figure 67). The reduction in Reynolds number (from Re/ft = 3×10^6 to 1.5×10^6) generally results in a small increase in $h_c/h_{co,s}$.

5.2.3.3 Model No. 10 ($M_{10} + P_1$)

The disturbance pattern in the wake region of Model No. 10 is confined to approximately one model diameter from the centerline for all Mach numbers (figure 68). The increase in $h_c/h_{co,s}$ with reduction in Reynolds number (from Re/ft = 3×10^6 to 1.5×10^6) is more apparent for this model than for the smaller models (Nos. 9, 2, and 5).

5.2.3.4 Model No. 5 ($M_5 + P_1$)

The lateral dimensions of Model No. 5 (figure 69) are the same as Model No. 2. The heat transfer coefficient ratios just behind the blunt afterface are low as noted in the discussion of $h_c/h_{co,s}$ along the centerline (Section 5.2.2.4). The heating ratios generally increase with a reduction in Reynolds number (Re/ft = 1.5×10^6). As in the case of Model No. 2, the disturbed heating pattern diminishes at approximately 2.5 diameters from the centerline.

5.2.4 Heating Effects on the Surfaces of Protuberances

The heat transfer coefficient ratio distributions both axially along the centerline of the models and at various instrumented cross-sections are presented for the four models in figures 70 through 73. The axial distributions of $h_c/h_{co,s}$ are plotted versus the dimensionless parameter x/ℓ (station distance from the forebody tip/total protuberance length) for all test Mach numbers and Reynolds numbers. The cross-sectional plots of $h_c/h_{co,s}$ versus z/δ are presented for all Mach numbers at Re/ft = 3 x 10^6 at instrumented points on the forebodies, centerbodies, and afterbodies of the models. It is noted that $h_c/h_{co,s}$ on the surfaces of the protuberances increases with increasing Mach number and also increases with decreasing Reynolds number as was the condition in the wake region.

The heat transfer data on the surfaces of the models are presented in the form of ratios of heat transfer coefficient on the model surface to flat plate (with stringers) heat transfer coefficient ($h_c/h_{co,s}$). This method of presentation is intended only for the purpose of comparison between models and a given set of flow parameters. It is not suggested that the $h_c/h_{co,s}$ values be used to determine the heating rates on the surfaces of protuberances. Analytical studies (unpublished internal reports) using the $h_c/h_{co,s}$ values on the protuberance surface have resulted in poor correlation.

5.2.4.1 Model No. 9

It is seen in figure 70(a) that heating on the forebody increases with increasing z/δ as expected. However, it would be expected that heating at the forward end of the centerbody would be somewhat lower than at the aft

end of the centerbody. It can be seen from the data that apparently the heating was much higher at the forward end of the centerbody. Because of this peculiar trend in the data, it was suspected that two-dimensional heat transfer effects for this small model were significant. From an analysis, it has been determined that a substantial amount of heat was conducted from the hot forebody to the relatively cool forward section of the centerbody. This condition resulted in a centerbody skin temperature rise (ΔT) that was greater than would occur from one dimensional convective aerodynamic heating alone. The same type of conduction effects occurred at the forward end of the afterbody, i.e., receiving heat from the centerbody. The effects of conduction were the most prominent on Model No. 9 which was the smallest model tested.

The heat transfer coefficients calculated from the temperature response (see Appendix) of the thermocouple do not include the effects of conduction. The heat transfer coefficients in the areas discussed have been adjusted to account for the conduction effects in Model No. 9 (Section 5.5.1.1).

The heat transfer coefficient ratios ($h_c/h_{co,s}$) generally vary directly with Mach number and vary inversely with Reynolds number.

Distribution of $h_c/h_{co,s}$ along the model periphery at various station planes are given in figure 70(b). The heating gradients are large on the high heating areas of the forebody due to immersion of the surface in the boundary layer. The heating ratios are essentially constant for each Mach number at the aft portion of the centerbody. A small reverse heating gradient occurs on the afterbody.

5.2.4.2 Model No. 2

The $h_c/h_{co,s}$ values on the forebody of Model No. 2 (Figure 71(a)) are somewhat higher than those on Model No. 9 (Figure 70 (a)) and are over seven times the flat plate value at M = 4.44. As expected, the heating on the forebody is dependent on the forebody surface angle and the immersion in the boundary layer. Model No. 2 has a forebody angle of 15 degrees and is approximately 89 percent of the boundary layer height. Model No. 9 has a forebody angle of 30 degrees and is approximately 42 percent of the boundary layer height. The compensating effects of forebody angle and boundary layer immersion on $h_c/h_{co,s}$ can be seen by comparing the two models at each Mach number. The $h_c/h_{co,s}$ values show the usual direct relationship to Mach number and inverse relationship to Reynolds number except on the afterbody. Here the inverse relationship to Mach number is noted. The $h_c/h_{co,s}$ values approach 1.0 as x/ℓ approaches 1.0. Conduction effects along the surface of Model No. 2 are not as apparent as was noted for Model No. 9. The thermocouples are located a greater distance from the juncture points making the conduction effects less pronounced. The $h_c/h_{co,s}$ profiles along the centerline of the model are essentially those that would be expected except at the aft end of the centerbody. Theoretically the heating on the centerbody increases in the aft direction. Conductive heat losses from the aft end of the centerbody into the relatively cool afterbody result in heat transfer coefficients that are somewhat lower than would be expected.

Distribution of $h_c/h_{co,s}$ along the model periphery at five station locations are given in figure 71(b). The heating gradients $[\Delta(h_c/h_{co,s})/\Delta(z/\delta)]$

vary directly with Mach number except on the afterbody. The effect of boundary layer immersion on $h_c/h_{co,s}$ is most pronounced on the forebody. The $h_c/h_{co,s}$ values at the forward end of the afterbody are approximately equal to those on the afterface of Model No. 5 (figure 73(a) and 73(b)) that is located in a region of separated flow. This similarity would indicate that flow separation is occurring at the forward end of the afterbody of Model No. 2.

5.2.4.3 Model No. 10

The heat transfer coefficient ratios on the forebody surface of Model No. 10 (figure 72(a)) are highest where the surface extends outside of the boundary layer ($x/\ell = 0.35$). The heating on the forebody decreases with immersion in the boundary layer.

The $h_c/h_{co,s}$ profiles along the centerline of the model are in agreement with theory. The magnitude of $h_c/h_{co,s}$ varies directly with Mach number and inversely with Reynolds number on the forebody and centerbody. On the afterbody, the opposite condition exists. The $h_c/h_{co,s}$ values approach 1.0 as x/ℓ approaches 1.0 (except for $M = 2.49$ and $Re/ft = 3 \times 10^6$ where the $h_c/h_{co,s}$ value approaches 2.0).

Distribution of $h_c/h_{co,s}$ along the model periphery at four station locations are given in figure 72(b). Large $h_c/h_{co,s}$ gradients exist on the forebody and are in direct relation to the Mach number. The variation in $h_c/h_{co,s}$ around the periphery of the centerbody and afterbody is small.

5.2.4.4 Model No. 5

The axial and cross-sectional distributions of $h_c/h_{co,s}$ for Model No. 5 are given in figures 73(a) and 73(b), respectively. The Model No. 5 forebody and centerbody configurations are the same as Model No. 2. Heating profiles in these areas are similar to those of Model No. 2 (see Section 5.2.4.2) considering the variation in tunnel flow parameters.

The heat transfer on the afterface is from 20 to 50 percent of flat plate values as would be expected.

5.3 Oil Flow Runs

The oil flow phase of the test was conducted to determine flow field patterns that develop in the wake region behind a protuberance. The oil flow patterns, although not a sensitive indicator of all the flow parameters affecting the heat transfer, were expected to delineate the flow boundaries and possibly to indicate the types of flow involved in wake heating. Two model configurations (No. 5 and No. 9) were tested on the smooth plate without stringers at various combinations of Mach number and Reynolds number. The testing was conducted on the smooth plate because it was believed that the oil flow patterns would not develop clearly on the irregular surface of the plate with stringers. Further, previous test data (Reference 2) indicated that stringers have little effect on wake patterns.

5.3.1 Oil Flow Photographs

Oil flow photographs of the wake region behind the two model configurations were obtained by means of a wide-angle-lens camera. The oil flow technique (Reference 5) consists of coating the test surface behind the protuberance

with a high viscosity oil. The oil has a fluorescent dye in suspension that becomes luminescent when exposed to ultraviolet light, making it possible to observe the formation of the wake patterns.

5.3.1.1 Model No. 9 ($M_9 + P_2$)

Figures 74 through 77 show the wake patterns behind Model No. 9 for the three test Mach numbers. Oil flow patterns were taken at Re/ft = 3×10^6 and 1.5×10^6 for M = 2.49 (figures 74 and 75, respectively). Oil flow tests at M = 3.51 and 4.44 were run only at Re/ft = 3×10^6 (figures 76 and 77, respectively).

The wake asymmetry noted in the photographs indicates some cross flow in the tunnel sidewall boundary layer. Also, the asymmetry may be partially attributable to the oil pattern sagging on the sidewall (gravitational effects) for the lower flow rates at M = 3.51 and 4.44.

The wake patterns at M = 2.49 appear to be very similar for the two Reynolds numbers except in the area directly behind the afterbody where a darker (scrubbed) surface appears for the lower Reynolds number. A somewhat higher heating rate is associated with this region. The dark region near the tip of the model afterbody is an area of high pressure and is also accompanied by an increase in heating. The lighter area forward on the afterbody is a region of low pressure associated with a low heating rate.

The oil flow patterns taken at M = 3.51 and 4.44 are similar to each other and are somewhat narrower than the patterns observed at M = 2.49. This trend of wake narrowing with increase in Mach number is reversed from the trend of the heating profiles where it was observed (Section 5.2.3.1) that the lateral disturbance effect increases with Mach number.

5.3.1.2 Model No. 5 ($M_5 + P_2$)

The upstream and downstream portions of the wake at M = 3.51 and Re/ft = 3×10^6 are shown in figures 78 and 79, respectively. The formation of the highly separated region behind the blunt afterbody is readily apparent. The existence of eddies on the test plate directly behind the model is visible. The maximum width of the observed wake is approximately 3.5 model diameters compared to 4 diameters for Model No. 9 at the same tunnel conditions.

5.3.2 Heating Profiles Compared to Observed Wake Patterns

The lateral heating profiles, $h_c/h_{co,s}$, are superimposed on the associated oil flow wake patterns in figures 80 and 81 for Models No. 9 and No. 5, respectively. The disturbance area is confined to the observed wake region behind Model No. 9 at M = 2.49. However, the high heating region is seen to extend laterally well beyond the observed wake at M = 4.44.

The observed wake pattern behind Model No. 5 (figure 81) generally corresponds to the disturbed heating profiles.

5.4 Pressure Coefficient Distributions in the Wake Regions

Pressure coefficient (C_p) profiles are presented in figures 82 through 85 for the four models at all test conditions. These profiles are developed from data obtained from a row of pressure taps running the length of the test plate between the second and third stringers (from the centerline). The geometrical relationship of the pressure sensors to the wake regions of each model varies. Therefore, the profiles cannot be directly compared to each other.

It is noted that freestream pressure ($C_p = 0$) essentially exists from 3 to 6 diameters downstream of the models. The negative pressure coefficients that appear at the rear of the plate are possibly due to faulty calibration of these sensors. This negative C_p condition exists on the calibration runs also. Previous tests using the same configuration do not show this negative C_p condition to exist.

A low pressure region (negative C_p) is observed 1 to 2 diameters behind all of the models except Model No. 9 (figure 82) where data are not obtained until 4.5 diameters downstream.

It can generally be stated that the absolute values of the pressure coefficients:

a. Vary directly with Mach number.

b. Vary inversely with Reynolds number in the low pressure regions.

c. Vary directly with Reynolds number in the high pressure regions.

5.5 Data Repeatability and Accuracy

The means for determining the repeatability of the data are limited due to most of the instrumentation on the test plate being located in disturbed air flow regions. The comparison of heating rates on surfaces of protuberances that have the same forebody angle and height (figures 71 and 73) show good repeatability considering some variation in tunnel flow parameters. A good indication of the repeatability of the data is obtained by comparing

the heating profiles in the wake regions at constant Mach numbers and varying Reynolds numbers (figures 66(b), 66(c), 67(b), 68(b), 68(c), 69(b) and 69(c)). The published accuracy limits (Reference 6) for determining heat transfer coefficients in the Langley Unitary Wind Tunnel Facility are:

HEAT TRANSFER COEFFICIENTS (BTU/sec-ft^2-$^\circ$R)	ACCURACY	CORRESPONDING TEST PARAMETERS	
		Mach Number	Re/ft
>0.0150	±10%	2.49	3×10^6
0.0010 to 0.0150	±15%	2.49	1.5×10^6
		3.51	3.0×10^6
<0.0010	±20%	3.51	1.5×10^6
		4.44	3×10^6

The instrumentation used for measuring pressures has an accuracy of 1 percent of full scale (720 psf). The possible pressure error of 7.2 psf is unaffected by Mach number. However, the error in pressure coefficient depends on Mach number as follows:

MACH NUMBER	RE/FT	ΔC_p
2.49	1.5×10^6	0.0170
	3.0×10^6	0.0090
3.51	1.5×10^6	0.0229
	3.0×10^6	0.0120
4.44	3.0×10^6	0.0161

5.5.1 Correlation of Theory and Data

5.5.1.1 Test Plate

Theoretical Stanton numbers (Reference 7) are plotted in figure 86 as a function of Reynolds number for the three test Mach numbers and temperature ratios (T_w/T_∞). The experimental data points are in all cases substantially lower than the theory predicts. This lack of correlation has been noted in past Langley Wind Tunnel Tests that were run under similar conditions. However, it should be noted that good agreement between experimental data and theory has been achieved in Langley tests (Reference 8) that were run with relatively thin (0.7 and 1.5 inches) boundary layers. It can generally be stated that agreement between theory and data improves with increasing Mach number and Reynolds number and also improves with decreasing boundary layer thickness. The reason for this is that thick boundary layers are associated with relatively low heating rates, making the departure from adiabatic wall conditions (conduction losses through the test plate) significant. However, the heat transfer coefficient ratios ($h_c/h_{co,s}$) are not greatly affected since the data have been normalized.

5.5.1.2 Centerline Surfaces of the Protuberance Models

Correlation of the heat transfer coefficient test data with theoretical values using the method of Van Driest (Reference 7) is given in figures 87 through 90. The data have been adjusted to account for the difference in the local recovery temperature and the flat plate recovery temperature from which the coefficients were derived.

In general, the theoretical heat transfer coefficients are determined on the various surfaces by the following procedure:

a. Forebody Surface

A conical shockwave is developed on the protuberance forebody corresponding to the upstream tunnel flow parameters. In the case of protuberances that are submerged in the boundary layer (Models No. 2, 5, and 9), a computer program is used to determine the local flow conditions within the boundary layer. The flow behind the shockwave is isentropically compressed to the conical forebody surface and the local flow conditions are determined.

b. Centerbody, Forward End

The flow at the outside edge of the boundary layer on the forebody surface is expanded around the cone/cylinder juncture using the Prandtl-Meyer relationships. Local properties are determined and the heat transfer coefficients are then calculated.

c. Centerbody, Aft End

The flow at the aft end of the protuberance centerbody is assumed to recompress from Prandtl-Meyer expansion to freestream conditions ($C_p = 0$). Heat transfer coefficients are based on flow properties behind the shockwave and freestream pressure.

d. Afterbody

Flow from the aft end of the centerbody is expanded to the forward end of the afterbody using Prandtl-Meyer relationships. Static pressure is assumed to return to freestream values at the tip of the afterbody.

The theoretical heat transfer coefficients agree reasonably well with the test data on all surfaces of Models No. 2, 10, and 5 (figures 88, 89, and 90, respectively).

A computer program was used to analytically adjust the data on Model No. 9 (figure 87) to account for the conduction effects. The heat transfer coefficient data were taken to be directly proportional to the ratio of the incremental temperature rise of an analytical model that considered no conduction to one that considered conduction.

$$h_{c_{adjusted}} = h_{c_{data}} \times \frac{(\Delta T/\Delta\theta) \text{ no conduction}}{(\Delta T/\Delta\theta) \text{ with conduction}}$$

6. CONCLUSIONS

The Protuberance Heating Test Program has provided additional knowledge on wake heating phenomena. A more complete description of the protuberance wake in terms of disturbance heating effects ($h_c/h_{co,s}$) has been obtained for various shaped protuberances. The effects of Mach number and Reynolds number variation on wake heating both on the protuberance and in the wake region have been determined.

A summary of the data evaluation shows the following trends:

a. Wake heating effects produced from conical forebody/conical afterbody protuberances are still present up to 25 diameters downstream of the body (to the end of the test plate). It is not known at this time where normal flat plate heating returns.

b. Heat transfer coefficient ratios on the protuberance surfaces and in the wake region increase with increasing Mach number and also increase with decreasing Reynolds number. The test Reynolds numbers are from 2 to 4 times higher than flight values due to tunnel and instrumentation limitations. The magnitude of the $h_c/h_{co,s}$ values for Reynolds numbers equal to those during flight at the time of maximum aerodynamic heating can only be approximated.

c. Wake heating effects are confined to the observed (oil flow patterns) wake region for Mach numbers up to 3.51. At a Mach number of 4.44, the lateral disturbed heating region extends outside of the observed wake pattern. This disturbance effect is seen to be larger in terms of protuberance diameters for small models.

d. The magnitude of the disturbance effect ($h_c/h_{co,s}$) in the wake region is strongly dependent on the size of the protuberance with respect to the boundary layer thickness.

e. The downstream increased heating effects in the wake region behind the boundary layer reattachment point are somewhat less for blunt afterbodies than for conical afterbodies.

f. The magnitudes of the flat plate heat transfer coefficient data, h_c, are from 45 to 60 percent lower than theoretical predictions. This occurrence is consistent with past Langley Wind Tunnel tests that were run with relatively thick (6 inch) boundary layers. It is concluded, however, that the heat transfer coefficient ratios ($h_c/h_{co,s}$) are not greatly affected since the experimental data have been normalized.

g. The heat transfer data on the surfaces of the protuberances correlate reasonably well with theoretical predictions.

REFERENCES

1. Test Control Drawing 1T08925, Protuberance Heating Test, dated July 1965.

2. Wilson, S.C. and Beckman, R.G., General Protuberance Heat Transfer Test Final Report: Volume I, Langley Data Report, DAC Report DM-46735, dated August 1964.

3. Yip, P.C., Test Reports For Phase I of the Aerodynamic Heating Tests at the NASA Langley Unitary Plan Wind Tunnel, Convair Report No. ZT-7-020, dated August 1958.

4. Burbank, Paige B. and Hodge, B. Leon, Distribution of Heat Transfer on a 10° Cone at Angles of Attack From 0° to 15° for Mach Numbers of 2.49 to 4.65 and a Solution To The Heat Transfer Equation That Permits Complete Machine Calculations, NASA Memo 6-4-59L, dated 1959.

5. Loving, D.L. and Katzoff, S., The Fluorescent Oil Film Method and Other Techniques For Boundary Layer Flow Visualization, NASA Memo 3-17-59L, dated 1959.

6. Taylor, Nancy L., Hodge, Ward F., and Burbank, Paige B., Heat Transfer and Pressure Measurements of a 1/7-scale Model of a Mercury Capsule at Angles of Attack From 0° to ±20° at Mach Numbers of 3.50 and 4.44, NASA TM X-522, dated 1961.

7. Van Driest, E.R., The Problem of Aerodynamic Heating, Aero. Engr. Review, Vol. 15, No. 10, Oct. 1956, pp 26-41.

8. Burbank, Paige B., Newlander, R.A., and Collins, Ida K., Heat Transfer and Pressure Measurements on a Flat-Plate Surface and Heat Transfer Measurements on Attached Protuberances in a Supersonic Turbulent Boundary Layer at Mach Numbers of 2.65, 3.51, and 4.44, NASA TN D-1372, dated December 1962.

TABLE 1. LOCATION OF INSTRUMENTATION THERMOCOUPLES – LANGLEY TEST

Model No. 2			
No.	x	y	z
300	-12.5	0	2.0
301	-10.1	-1.3	1.7
302	- 7.8	0	3.3
303	- 3.1	0	4.6
304	- 3.1	-2.2	2.0
305	- 3.1	-2.3	1.5
306	0.2	0	5.0
307	0.2	-2.5	2.9
308	0.2	-2.5	1.5
309	4.9	0	5.0
310	4.9	-2.5	2.9
311	4.9	-2.5	1.5
312	9.7	0	5.0
313	9.7	-2.5	1.5
314	12.7	0	4.1
315	12.7	-2.0	1.5
316	19.5	-1.5	1.9
317	16.3	0	2.0

Model No. 9			
No.	x	y	z
700	- 3.9	0	1.0
701	- 2.9	-0.8	0.8
702	- 1.9	0	2.2
703	- 1.9	-1.1	1.4
704	- 1.9	-1.1	0.8
705	- 0.9	0	2.9
706	- 0.9	-1.2	1.5
707	- 0.9	-1.2	0.8
708	0.6	0	2.5
709	0.6	-1.2	1.5
710	0.6	-1.3	0.8
711	1.6	0	2.2
712	1.6	-1.1	1.4
713	1.6	-1.1	0.8
714	2.6	-0.8	0.8
715	3.6	0	1.1

Model No. 5			
No.	x	y	z
500	-13.7	0	2.0
501	-11.3	-1.3	1.5
502	- 8.9	0	3.3
503	- 3.6	0	4.7
504	- 3.6	-2.3	2.9
505	- 3.6	-2.4	1.5
506	- 1.1	0	5.0
507	- 1.1	-2.4	3.1
508	- 1.1	-2.5	1.5
509	3.7	0	5.0
510	3.7	-2.4	3.1
511	3.7	-2.5	1.5
512	8.4	0	5.0
513	8.4	-2.4	3.1
514	8.4	-2.5	1.5
515	9.9	0	4.0
516	9.9	-1.2	1.5
517	9.9	0	1.5

Model No. 10			
No.	x	y	z
800	-14.5	0	4.5
801	-10.6	-3.1	4.2
802	- 6.6	0	9.1
803	- 6.6	-4.1	5.6
804	- 6.6	-4.5	1.5
805	- 3.5	0	10.0
806	- 3.5	-4.7	6.7
807	- 3.5	-5.0	1.5
808	3.5	0	10.0
809	3.5	-4.7	6.7
810	3.5	-5.0	1.5
811	6.5	0	9.1
812	6.5	-4.1	5.6
813	6.5	-4.5	1.5
814	10.6	-3.1	4.2
815	14.5	0	4.5

TABLE 1. LOCATION OF INSTRUMENTATION THERMOCOUPLES – LANGLEY TEST (Continued)

Tank Plate			Tank Plate (Cont.)		
No.	x	y	No.	x	y
1	7.4	0	43	53.4	0
2	8.4	0	44	54.4	0
3	9.4	0	45	55.4	0
4	10.4	0	46	56.4	0
5	11.4	0	47	57.4	0
6	12.4	0	48	58.4	0
7	13.4	0	49	59.4	0
8	14.4	0	50	60.4	0
9	15.4	0	51	61.4	0
10	16.4	0	52	62.4	0
11	17.4	0	53	63.4	0
12	18.4	0	54	8.1	2.0
13	19.4	0	55	11.9	2.0
14	20.4	0	56	11.9	4.0
15	21.4	0	57	11.9	6.0
16	22.4	0	58	11.9	8.0
17	23.4	0	59	11.9	10.0
18	24.4	0	60	11.9	14.0
19	25.4	0	61	16.9	2.0
20	26.4	0	62	16.9	4.0
21	27.4	0	63	16.9	6.0
22	28.4	0	64	16.9	10.0
23	29.4	0	65	19.4	4.0
24	30.4	0	66	19.4	10.0
25	31.4	0	67	21.4	2.0
26	32.4	0	68	21.4	4.0
27	32.8	0	69	21.4	6.0
28	33.1	0	70	21.4	8.0
29	39.9	0	71	21.4	10.0
30	40.4	0	72	21.4	12.0
31	41.4	0	73	21.4	16.0
32	42.4	0	74	23.4	4.0
33	43.4	0	75	23.4	10.0
34	44.4	0	76	25.4	2.0
35	45.4	0	77	25.4	4.0
36	46.4	0	78	25.4	10.0
37	47.4	0	79	27.4	4.0
38	48.4	0	80	27.4	10.0
39	49.4	0	81	29.4	4.0
40	50.4	0	82	29.4	10.0
41	51.4	0	83	31.4	2.0
42	52.4	0	84	31.4	4.0

TABLE 1. LOCATION OF INSTRUMENTATION THERMOCOUPLES AND PRESSURE TAPS – LANGLEY TEST (Continued)

Test Plate (Cont.)			Test Plate		
No.	x	y	No.	x	y
85	31.4	6.0	P1	12.1	-4.0
86	31.4	8.0	P2	16.0	-4.0
87	31.4	10.0	P3	16.0	-8.0
88	31.4	12.0	P4	23.7	-4.0
89	31.4	14.0	P5	31.4	-4.0
90	31.4	16.0	P6	31.4	-8.0
91	36.4	4.0	P7	31.4	-12.0
92	36.4	10.0	P8	36.4	-4.0
93	41.4	2.0	P9	41.4	-4.0
94	41.4	4.0	P10	51.4	-4.0
95	41.4	6.0	P11	61.4	-4.0
96	41.4	8.0	P12	61.4	-8.0
97	41.4	10.0			
98	41.4	12.0			
99	41.4	14.0			
100	41.4	16.0			
101	46.4	2.0			
102	46.4	10.0			
103	51.4	2.0			
104	51.4	4.0			
105	51.4	6.0			
106	51.4	10.0			
107	51.4	14.0			
108	56.4	2.0			
109	56.4	10.0			
110	61.4	2.0			
111	61.4	4.0			
112	61.4	6.0			
113	61.4	8.0			
114	61.4	10.0			
115	61.4	12.0			
116	61.4	14.0			
117	11.9	-6.0			
118	17.6	-10.0			
119	21.4	-6.0			
120	29.4	-10.0			
121	31.4	-10.0			
122	46.4	-10.0			
123	56.4	-10.0			

TABLE 2. LANGLEY PROTUBERANCE HEATING TEST RUN SCHEDULE

RUN	MODEL CONFIGURATION	PARAMETER INVESTIGATED	DATA h, p*	REYNOLDS NO. x 10^{-6}	MACH NO.
1-1	P_1**	Calibration	h,p	3.9439	2.49
1-2	P_1	Calibration	h,p	1.5727	2.49
1-3	P_1	Calibration	h	2.9434	3.51
1-4	P_1	Calibration	h	1.2896	3.51
1-5	P_1	Calibration	p	1.7000	3.51
1-6	P_1	Calibration	h,p	3.1985	4.44
2-1	$P_1 + M_9$	Wake Heating	h,p	3.0318	2.49
2-2	$P_1 + M_9$	Wake Heating	h,p	1.5804	2.49
2-3	$P_1 + M_9$	Wake Heating	h,p	2.9514	3.51
2-4	$P_1 + M_9$	Wake Heating	h,p	1.5532	3.51
2-5	$P_1 + M_9$	Wake Heating	h,p	3.2185	4.44
3-1	$P_1 + M_2$	Wake Heating	h,p	3.0695	2.49
3-2	$P_1 + M_2$	Wake Heating	h,p	1.5705	2.49
3-3	$P_1 + M_2$	Wake Heating	h,p	2.9789	3.51
3-4	$P_1 + M_2$	Wake Heating	h,p	3.2592	4.44
4-1	$P_1 + M_{10}$	Wake Heating	h,p	3.0394	2.49
4-3	$P_1 + M_{10}$	Wake Heating	h,p	1.5546	2.49
4-4	$P_1 + M_{10}$	Wake Heating	h,p	2.9698	3.51
4-5	$P_1 + M_{10}$	Wake Heating	h,p	1.5614	3.51
4-6	$P_1 + M_{10}$	Wake Heating	h,p	3.1722	4.44
5-1	$P_1 + M_5$	Wake Heating	h,p	3.0264	2.49
5-2	$P_1 + M_5$	Wake Heating	h,p	1.5586	2.49

TABLE 2. LANGLEY PROTUBERANCE HEATING TEST RUN SCHEDULE (Continued)

RUN	MODEL CONFIGURATION	PARAMETER INVESTIGATED	DATA h,p*	REYNOLDS NO. x 10^{-6}	MACH NO.
5-3	$P_1 + M_5$	Wake Heating	h,p	3.1848	4.44
5-4	$P_1 + M_5$	Wake Heating	h,p	2.9351	3.51
5-5	$P_1 + M_5$	Wake Heating	h,p	1.5426	3.51
6-4	P_2** $+ M_9$	Oil Flow	h,p	3.0529	2.49
6-5	$P_2 + M_9$	Oil Flow	h,p	1.5578	2.49
6-6	$P_2 + M_9$	Oil Flow	h,p	3.1983	4.44
6-7	$P_2 + M_9$	Oil Flow	h,p	2.9475	3.51
6-8	$P_2 + M_9$	Oil Flow	h,p	1.5519	3.51

*h- heat transfer
p- pressure

**P_1- plate with stringers
P_2- plate without stringers

MODEL NO.	FOREBODY	BODY	AFTERBODY
M_2	15°	2.5 CAL	30°
M_5	15°	2.5 CAL	0°
M_9	30°	0.5 CAL	30°
M_{10}	30°	2 CAL	30°

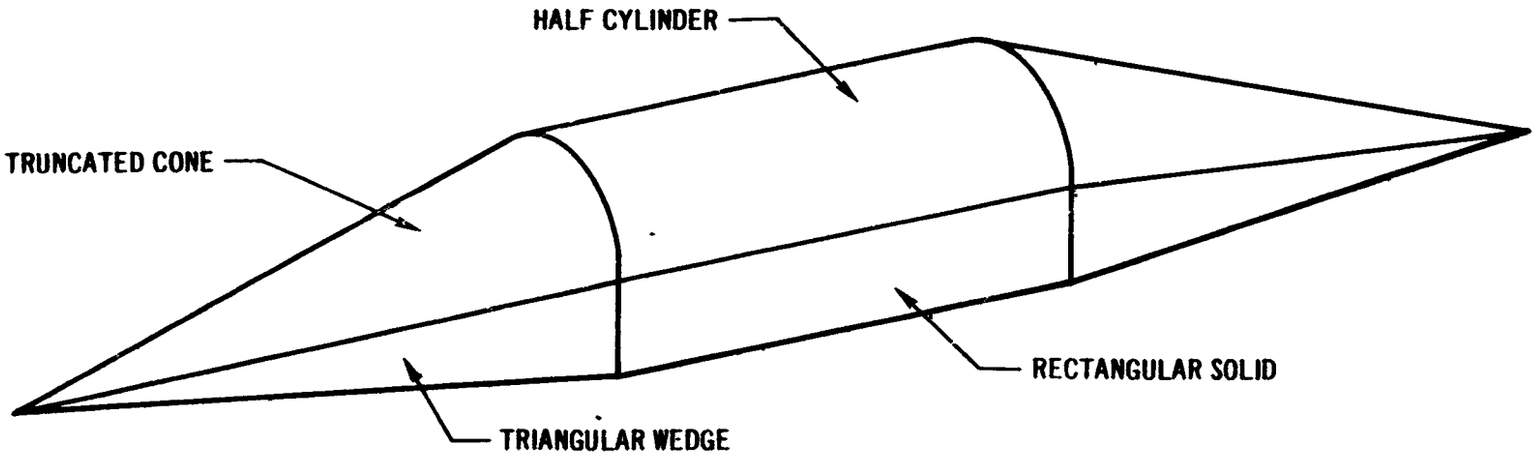

Figure 1. General Protuberance Shape

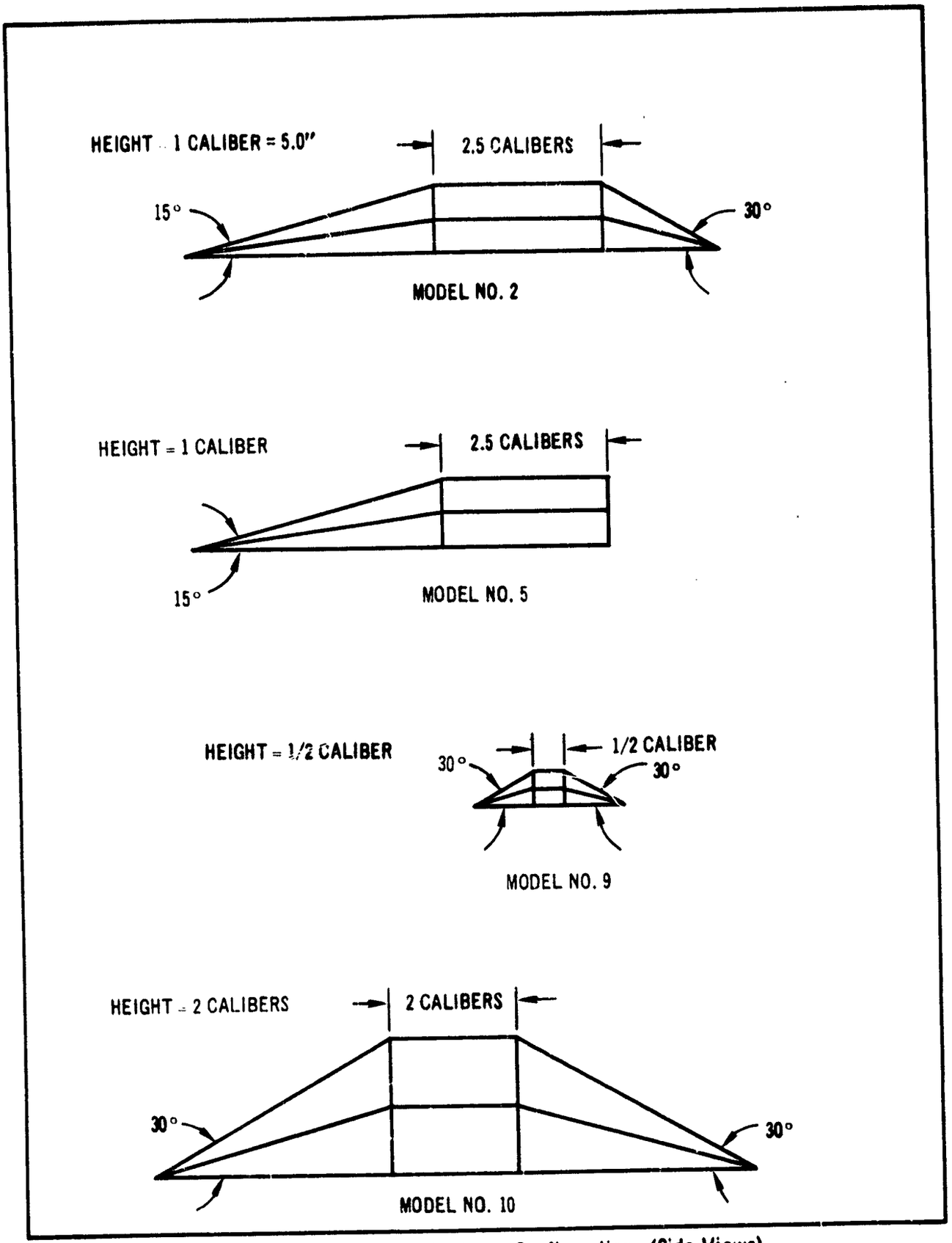

Figure 2. Protuberance Models Basic Configurations (Side Views)

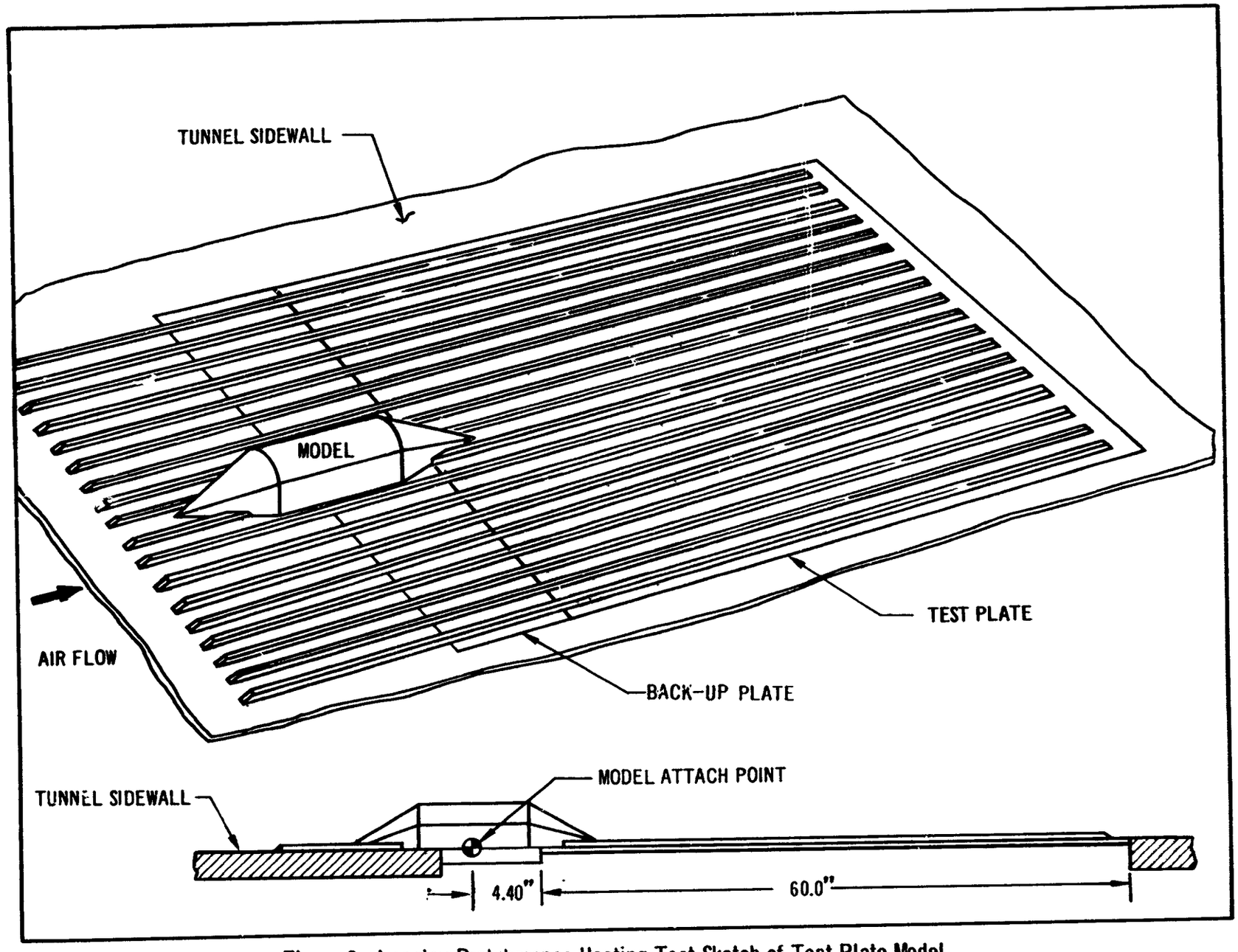

Figure 3. Langley Protuberance Heating Test-Sketch of Test Plate Model

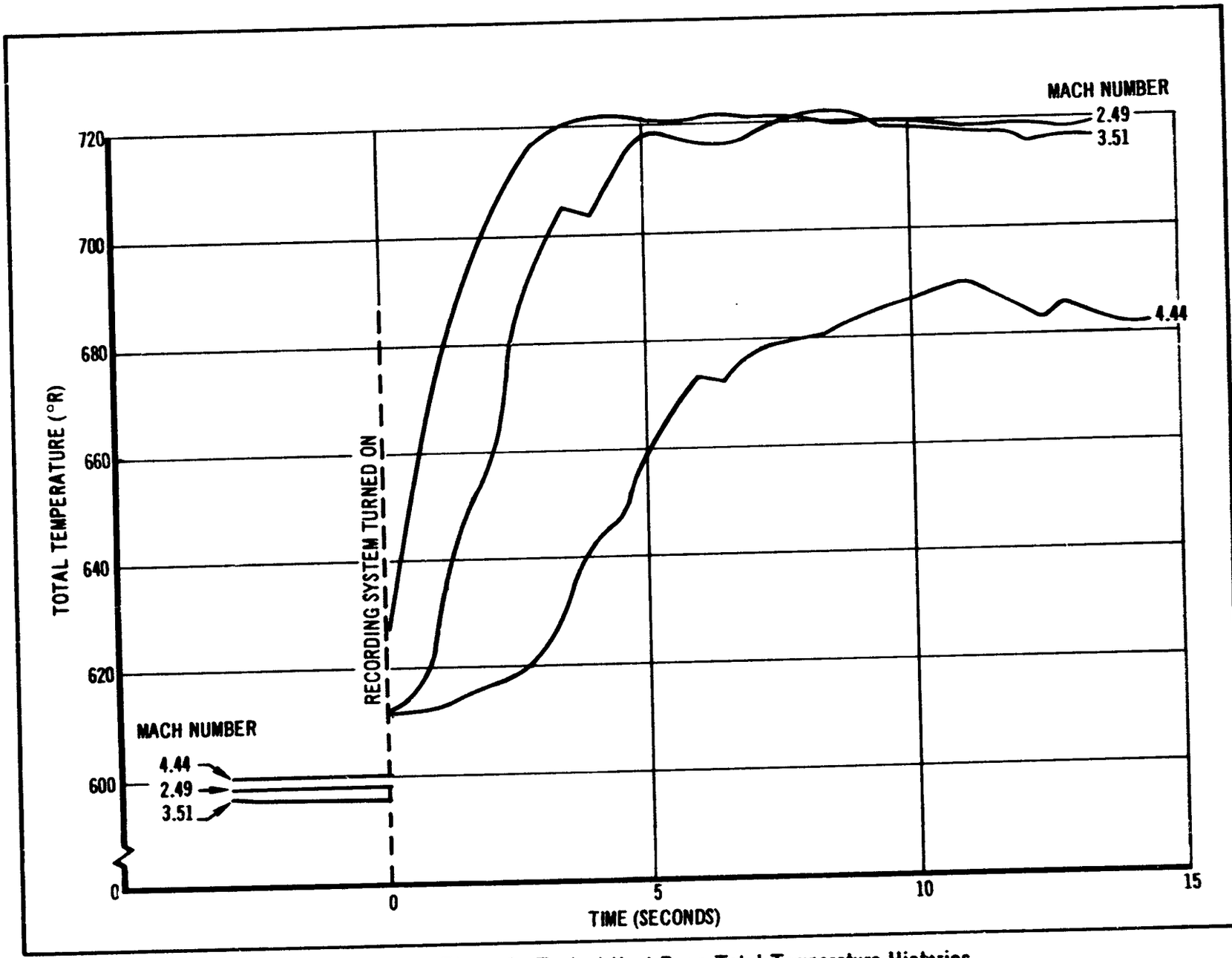

Figure 4. Typical Heat Bump Total Temperature Histories

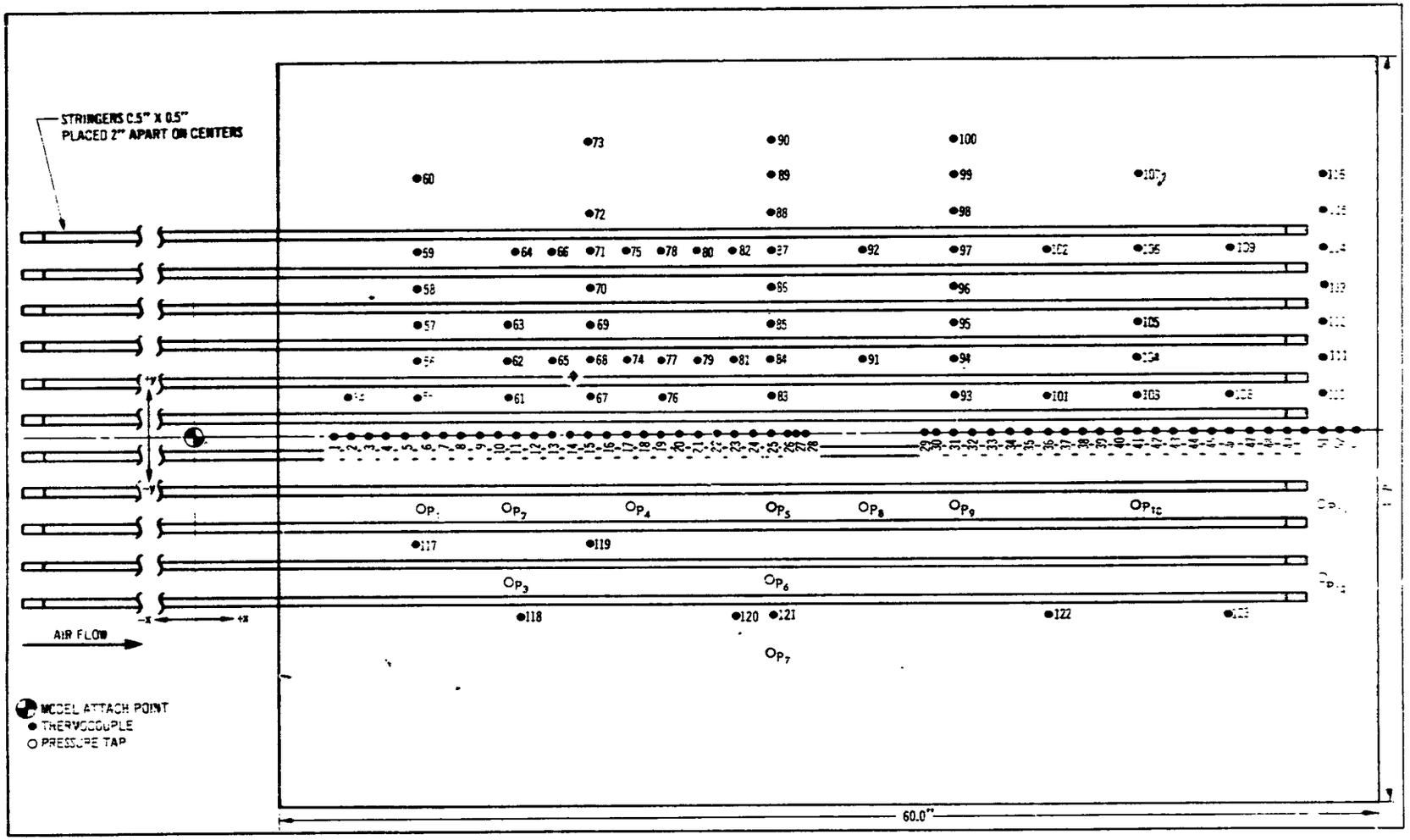

Figure 5. Test Plate – Langley UPWT Test

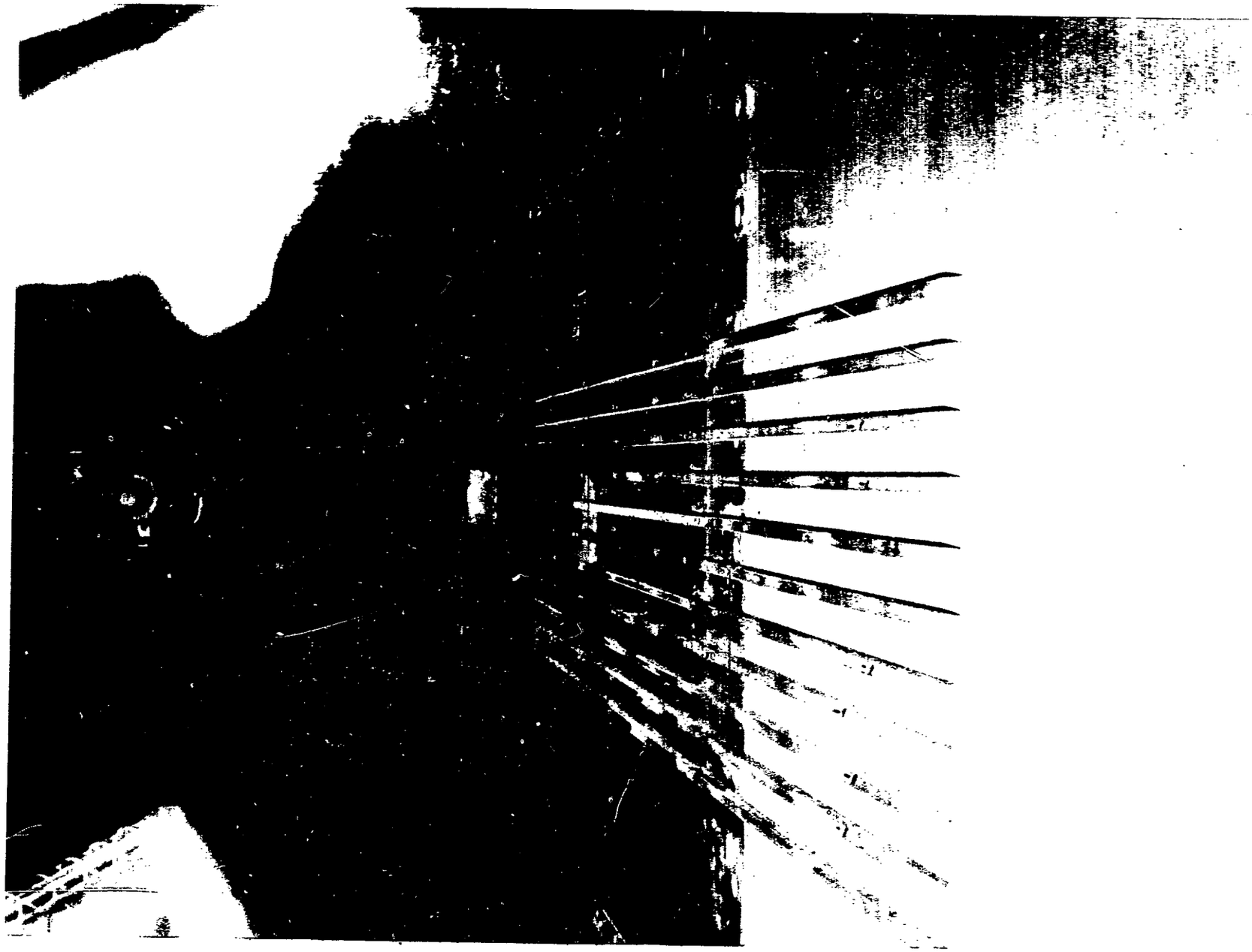

Figure 5. (Cont) Langley Test Plate P_1

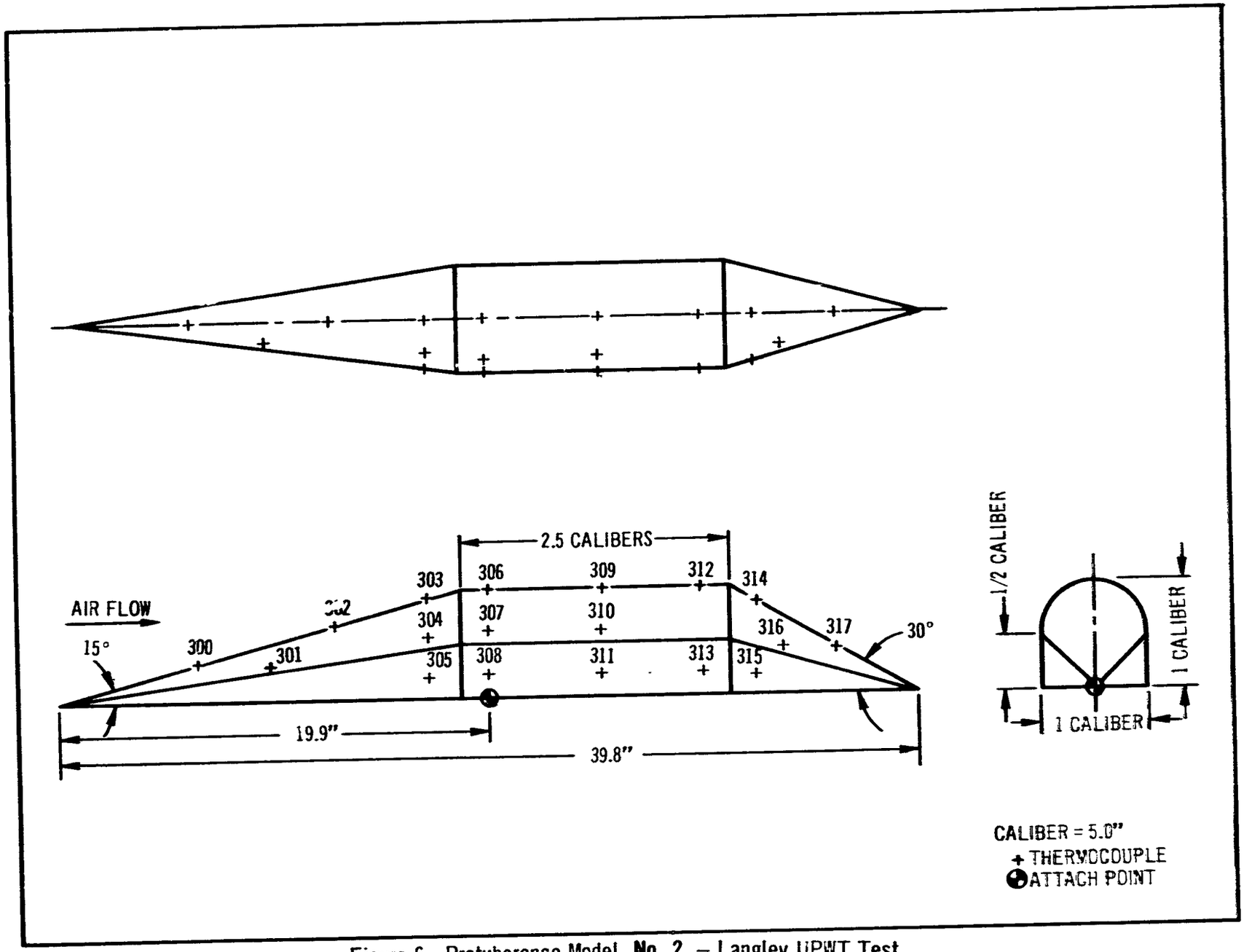

Figure 6. Protuberance Model No. 2 – Langley UPWT Test

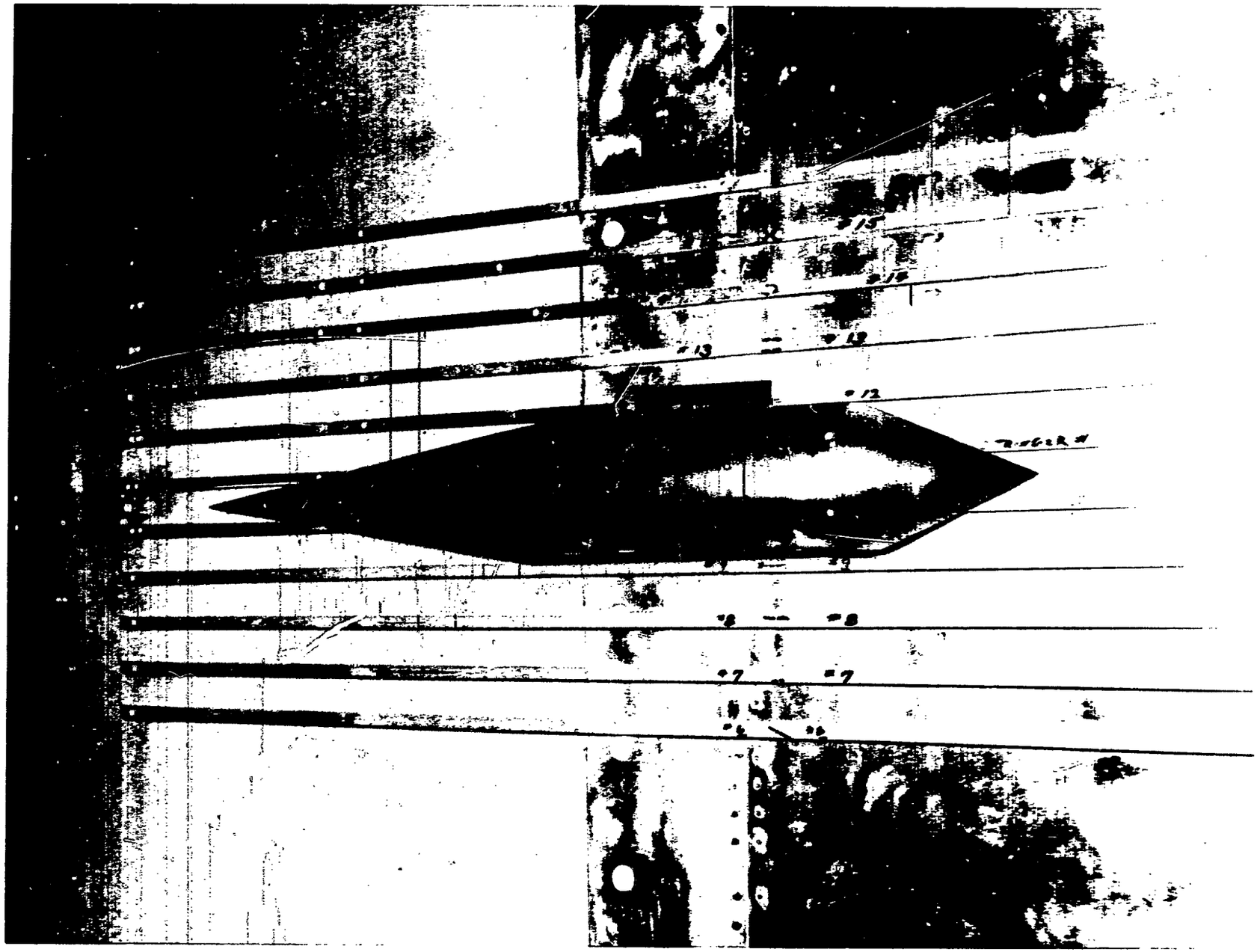

Figure 6. (Cont)– Model No. 2 on Plate P_1

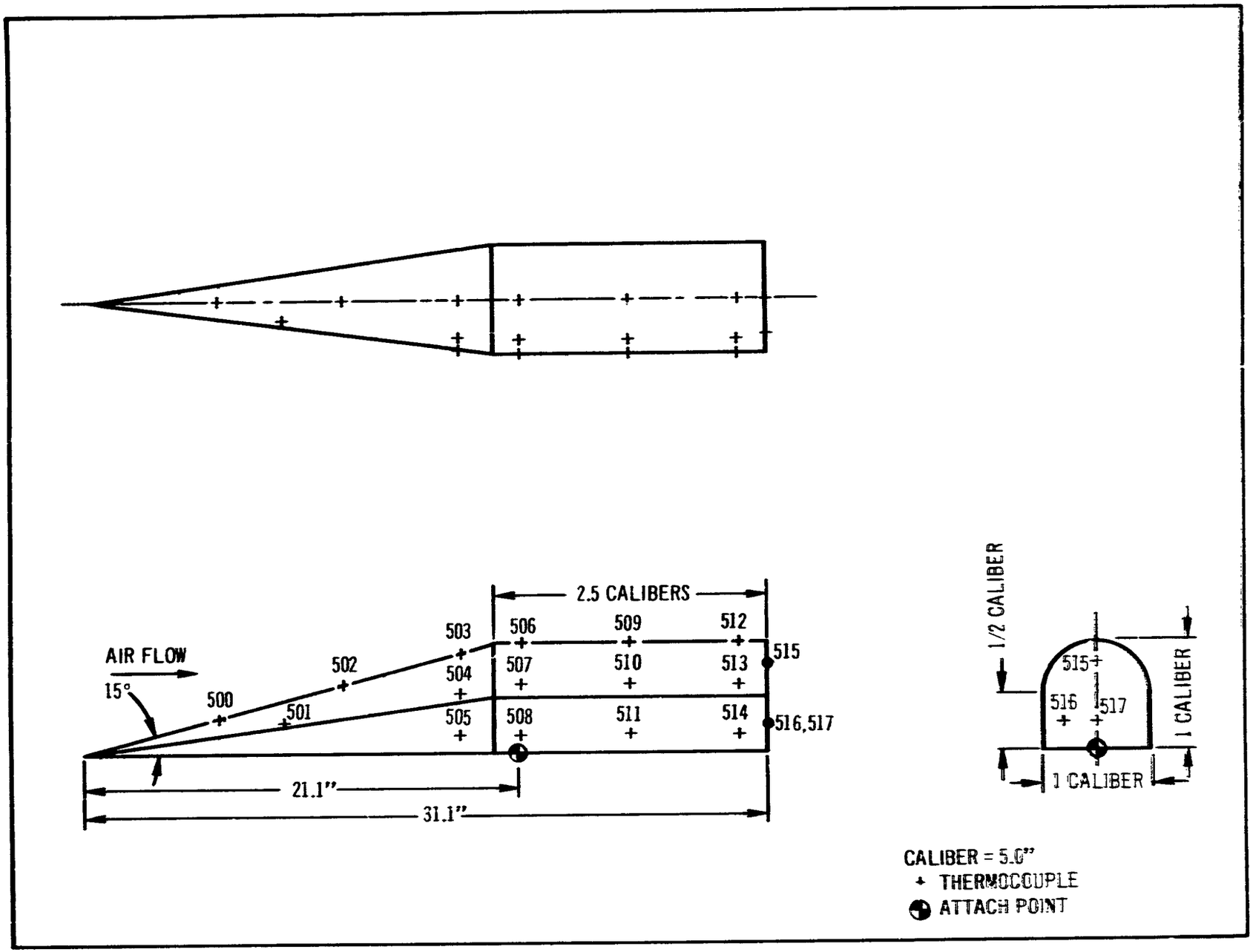

Figure 7. Protuberance Model No. 5 – Langley UPWT Test

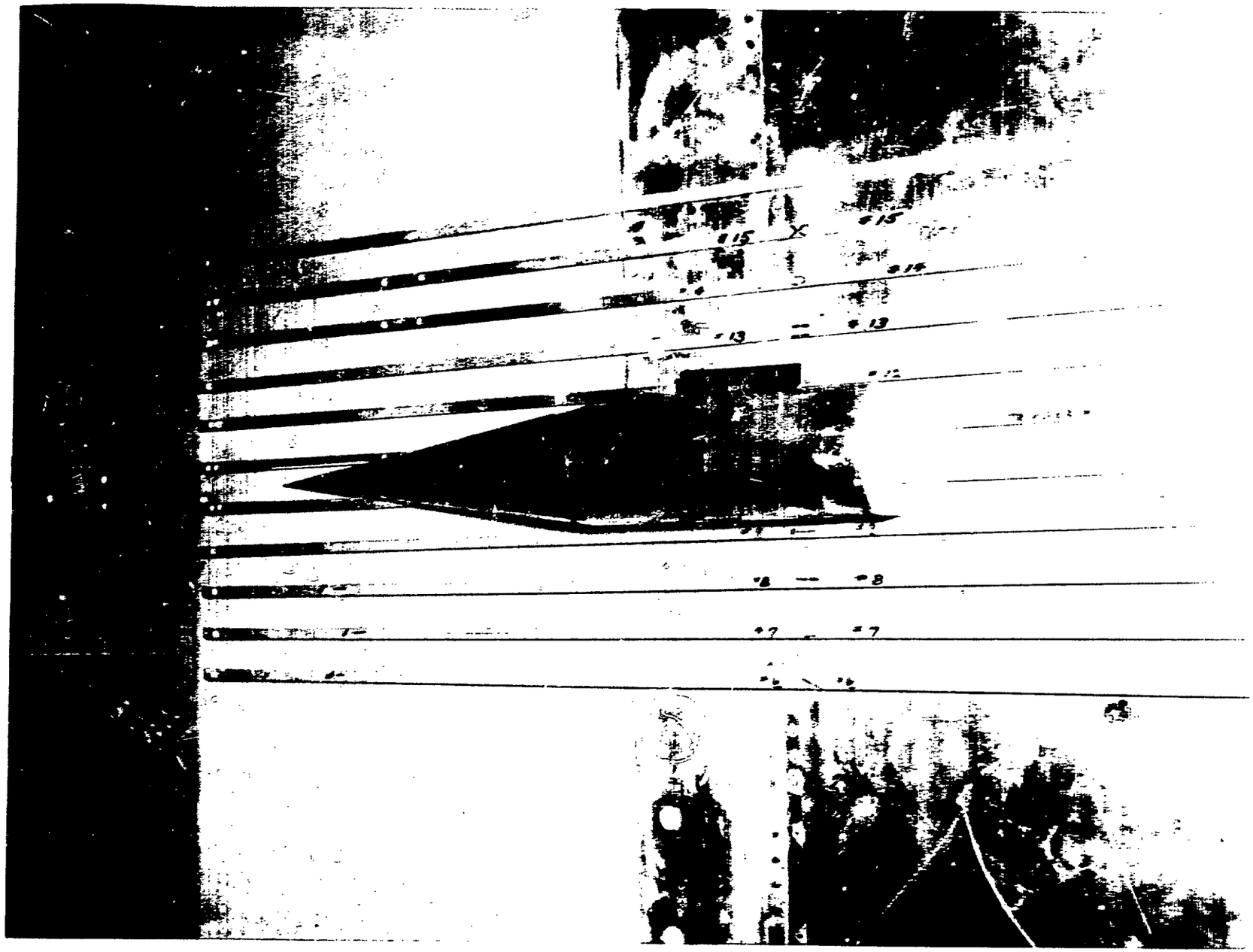

Figure 7. (Cont) Model No. 5 on Plate P_1

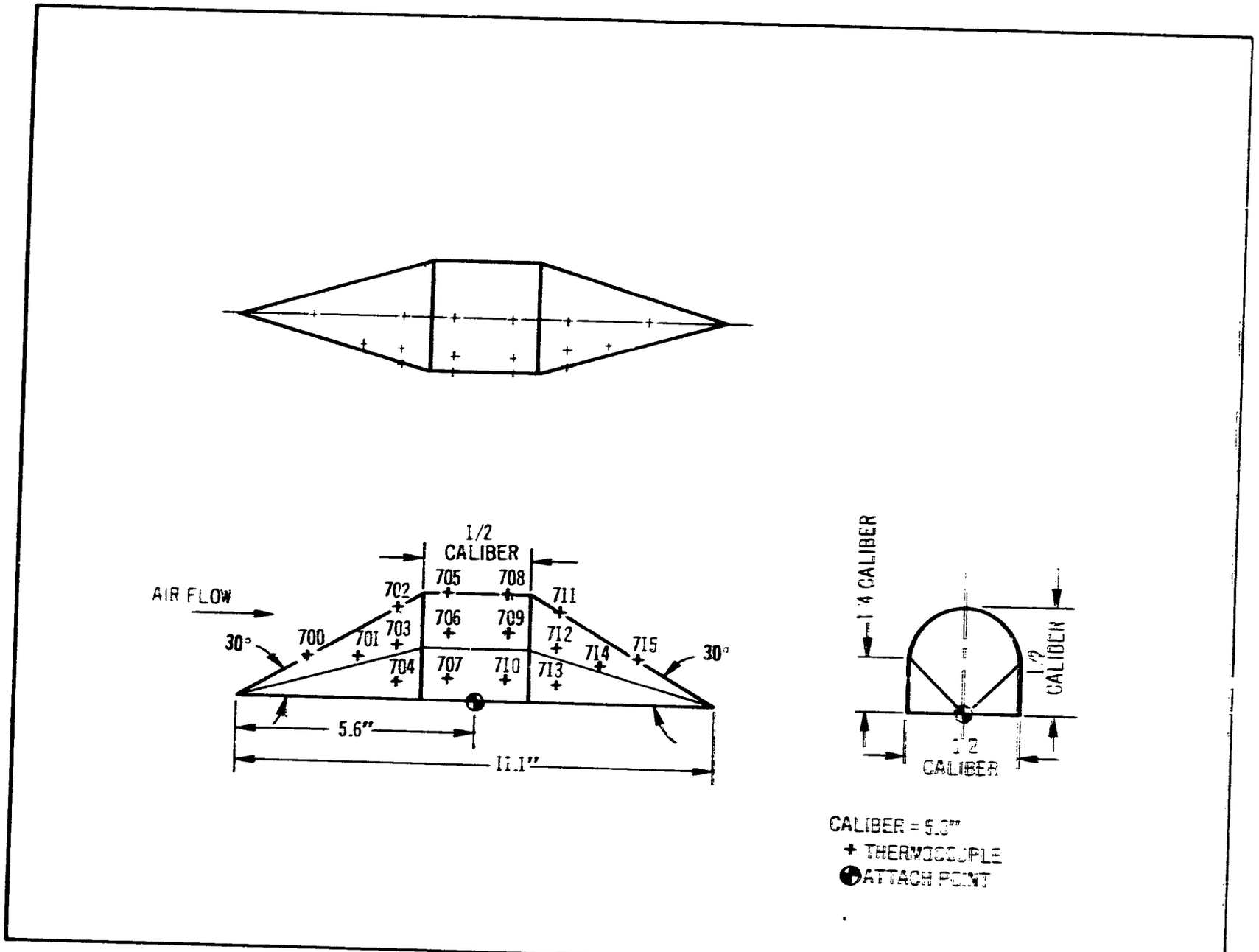

Figure 8. Protuberance Model No. 9 – Langley UPWT Test

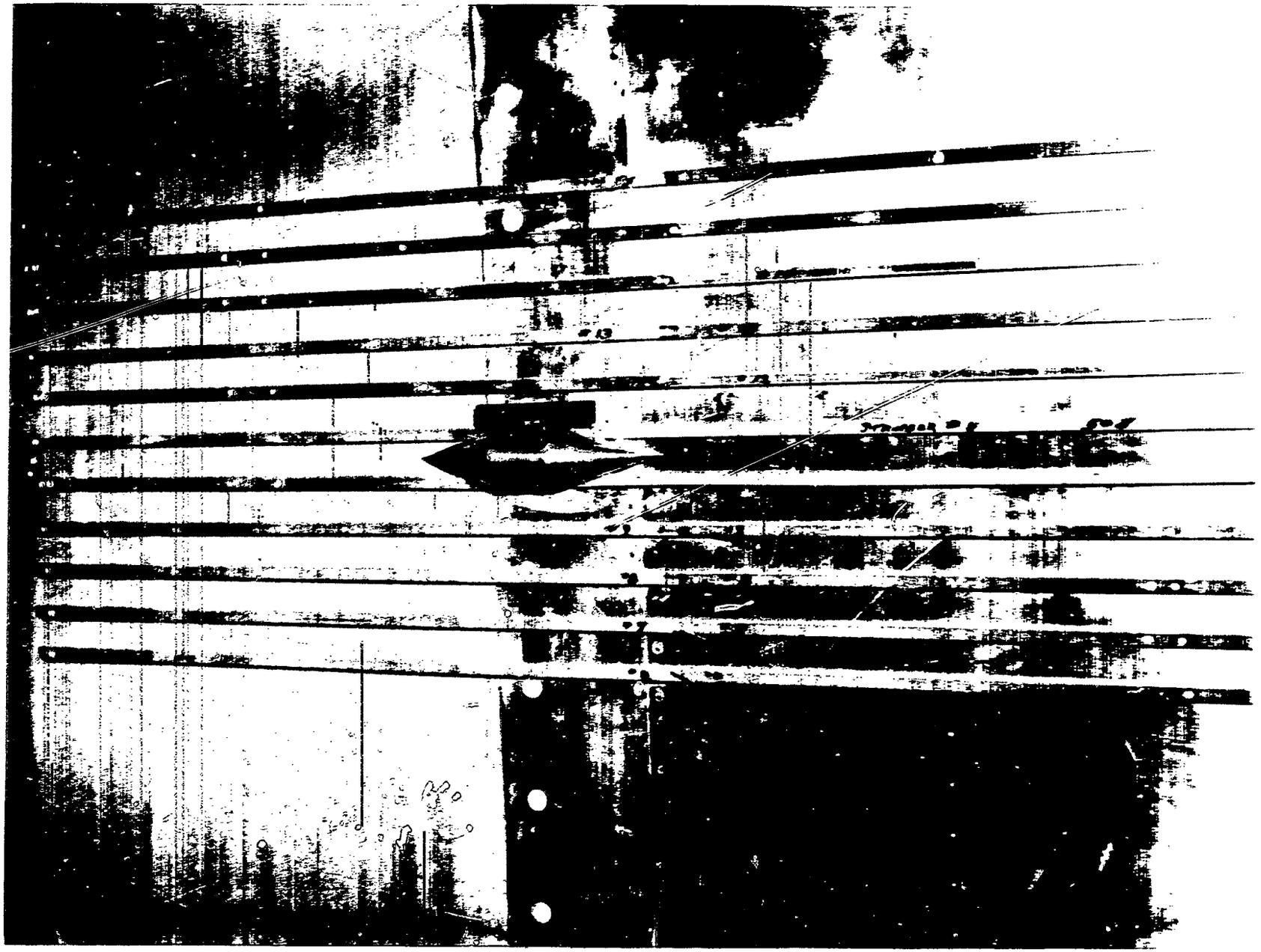

Figure 8. (Cont) Model No. 9 on Plate P_1

Figure 8. (Cont) Model No. 9 on Plate P_2

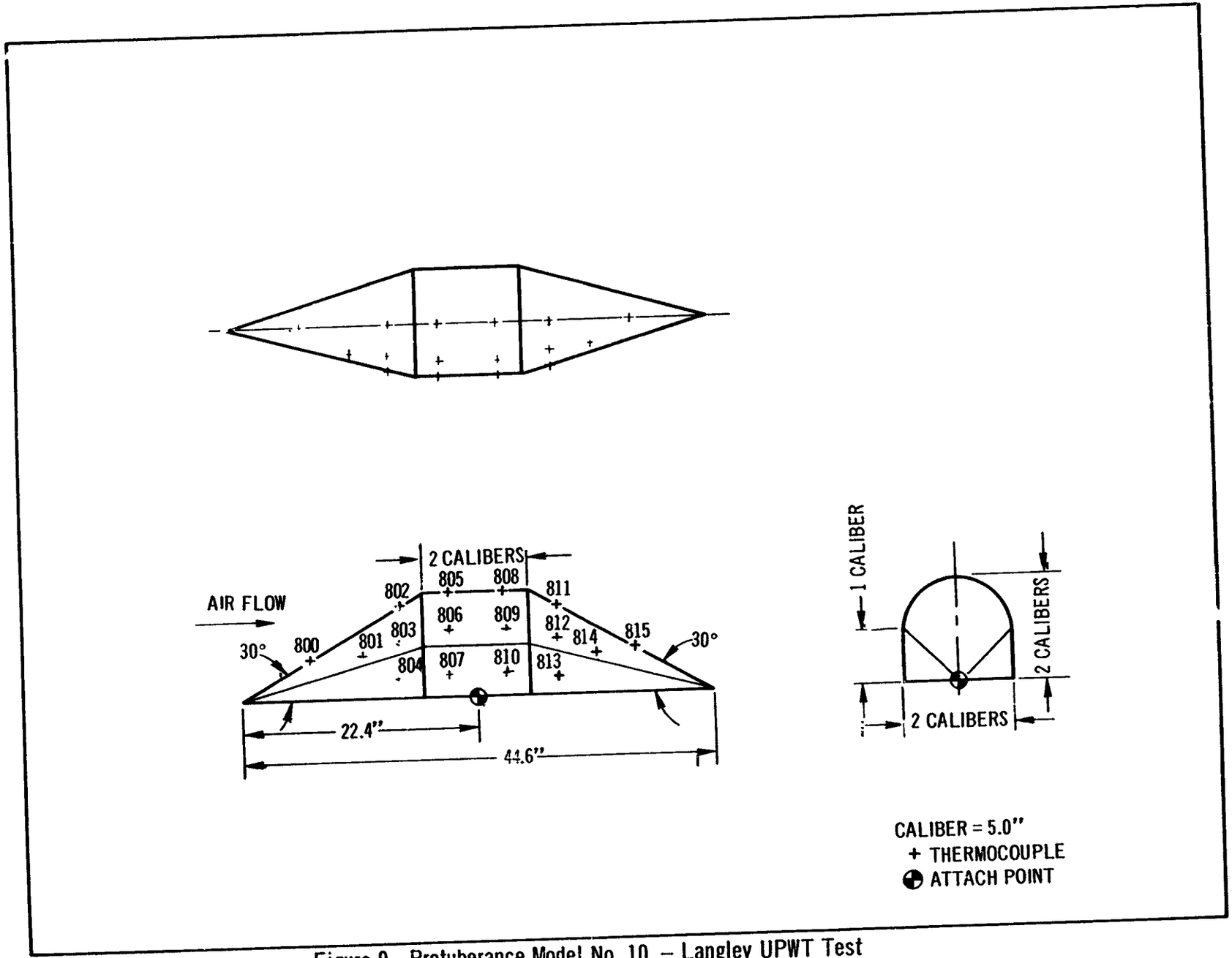

Figure 9. Protuberance Model No. 10 – Langley UPWT Test

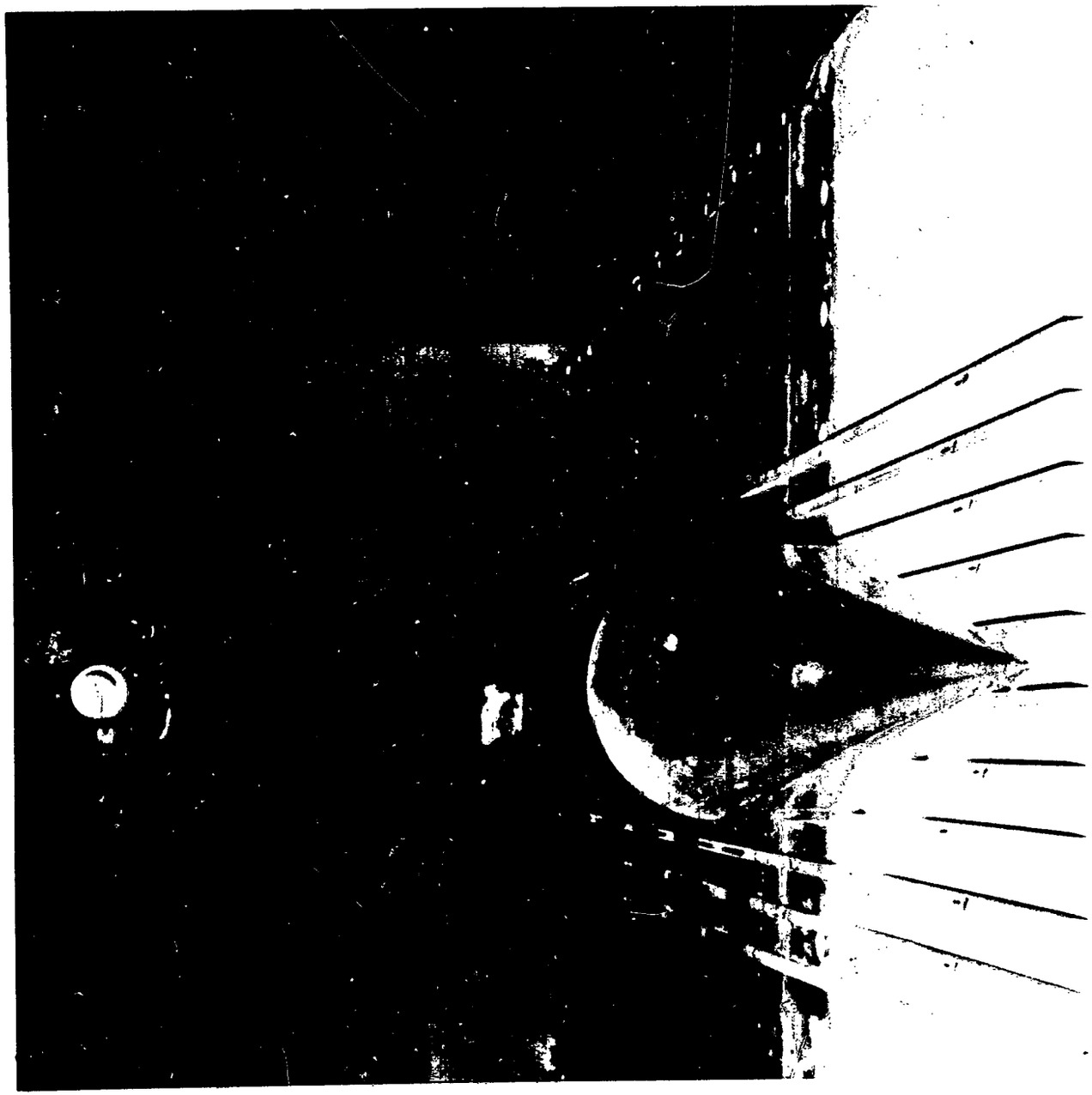

Figure 9. (Cont) Model No. 10 on Plate P_1

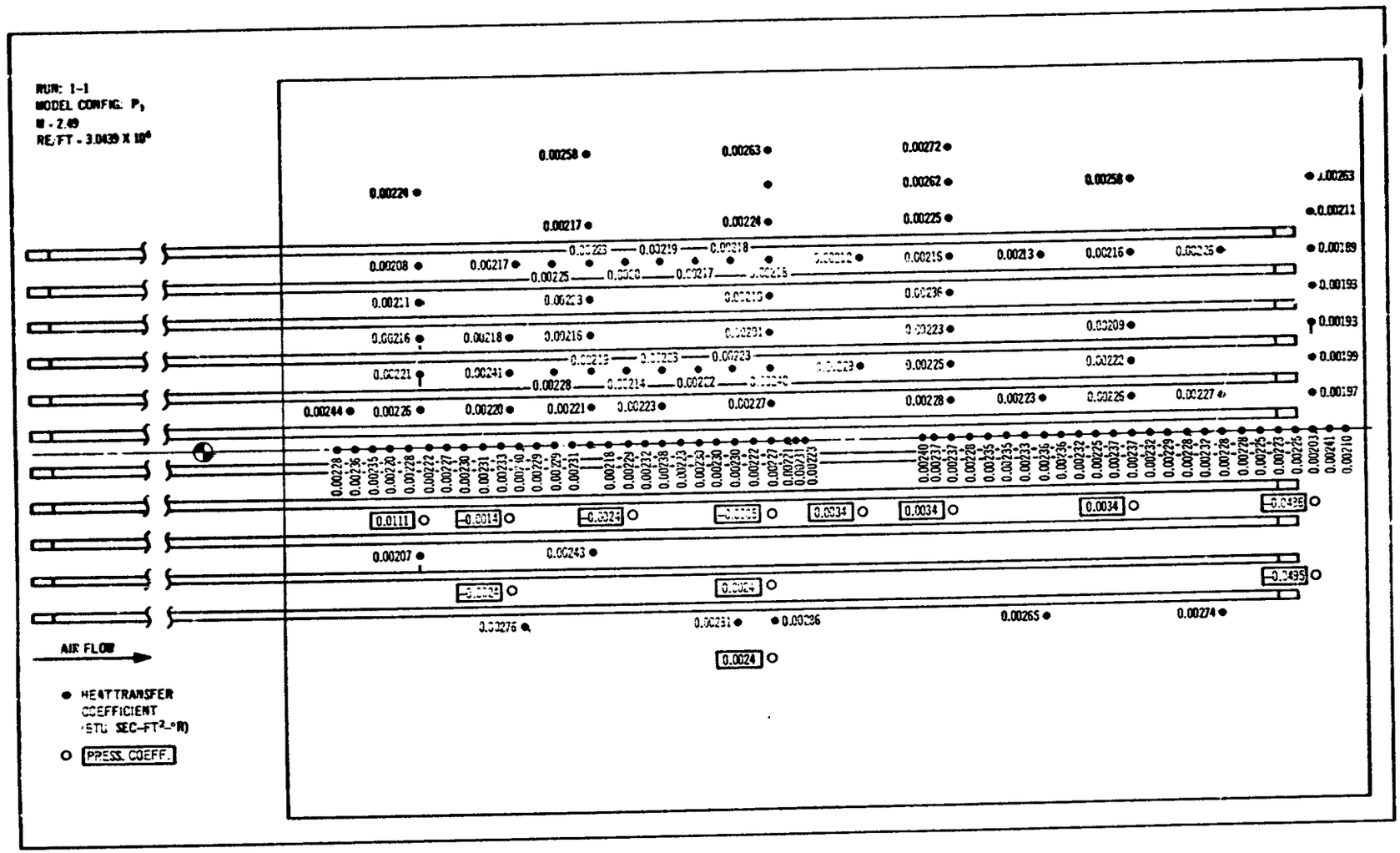

Figure 10. Langley Protuberance Heating Test-Heat Transfer Coefficients and Pressure Coefficients; Calibration Runs

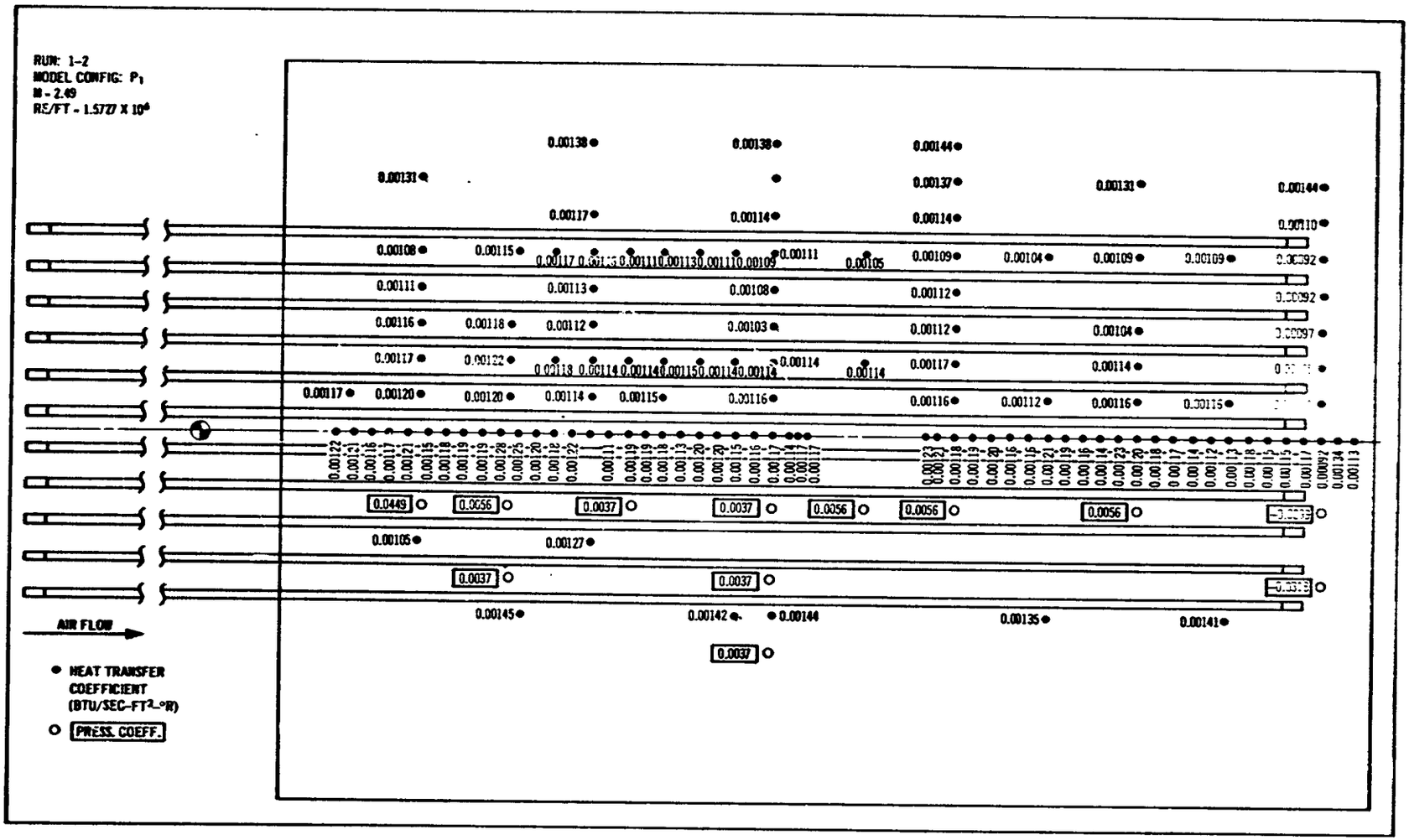

Figure 11. Langley Protuberance Heating Test-Heat Transfer Coefficients and Pressure Coefficients; Calibration Runs

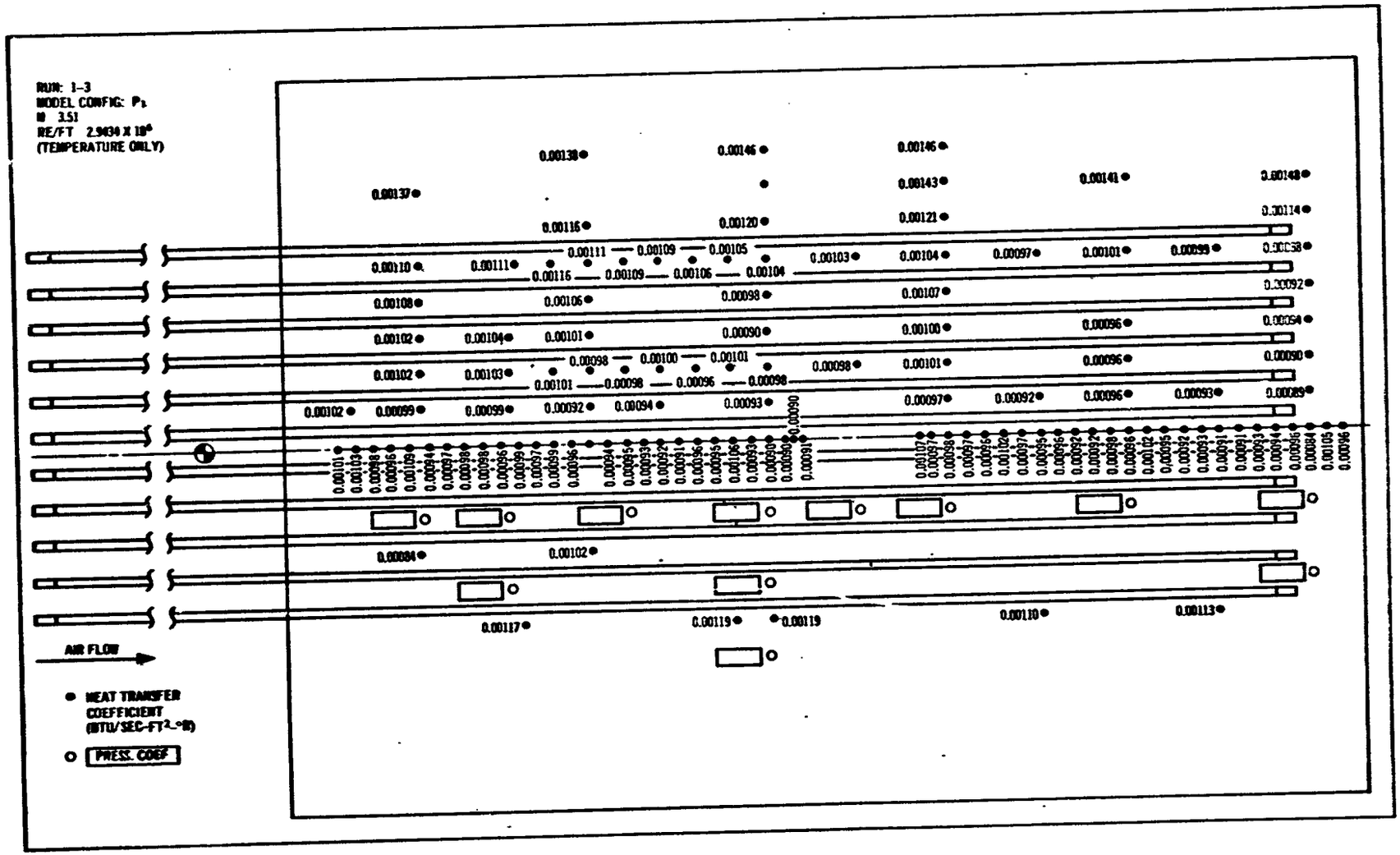

Figure 12. Langley Protuberance Heating Test-Heat Transfer Coefficients ; Calibration Runs

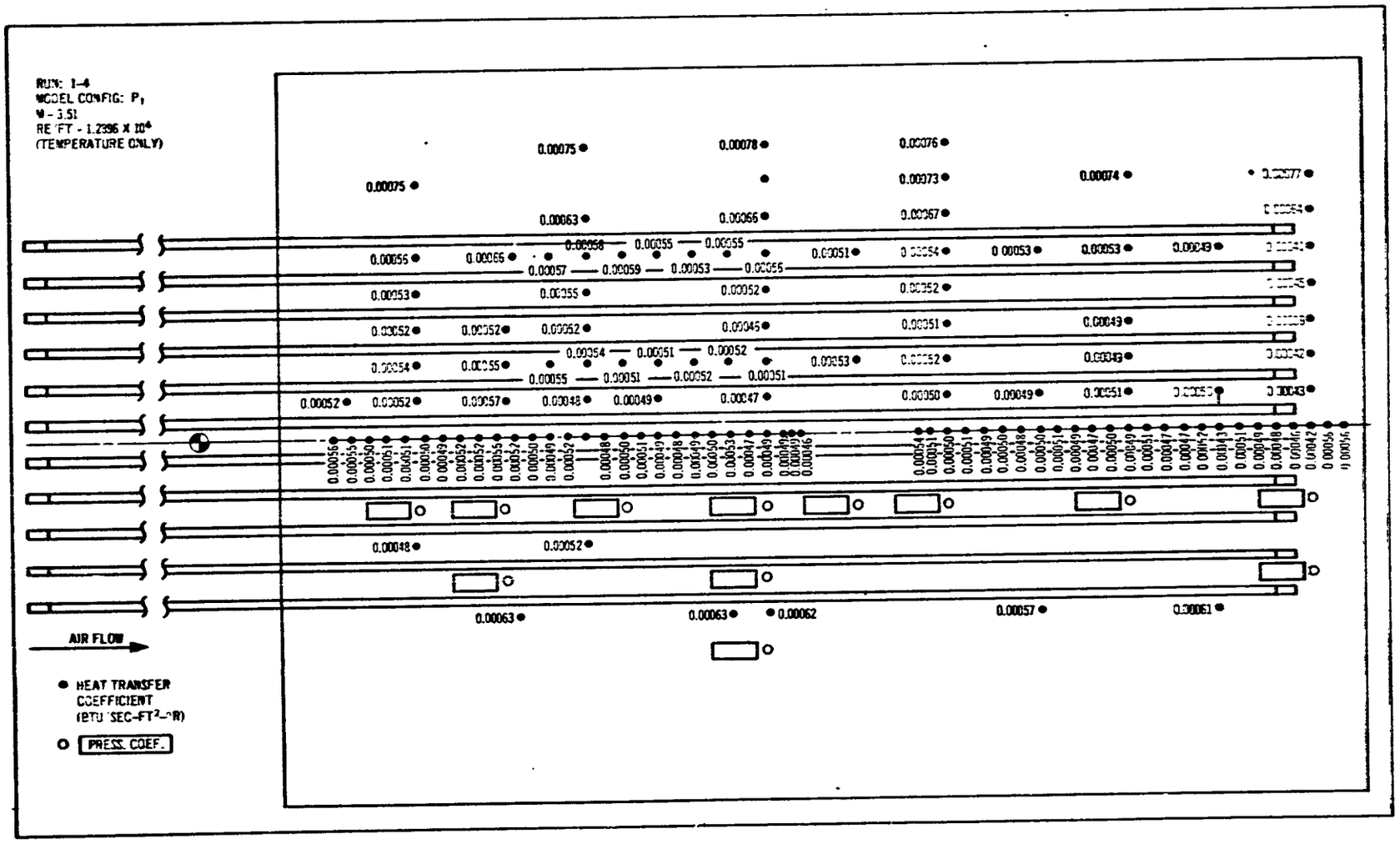

Figure 13. Langley Protuberance Heating Test-Heat Transfer Coefficients ; Calibration Runs

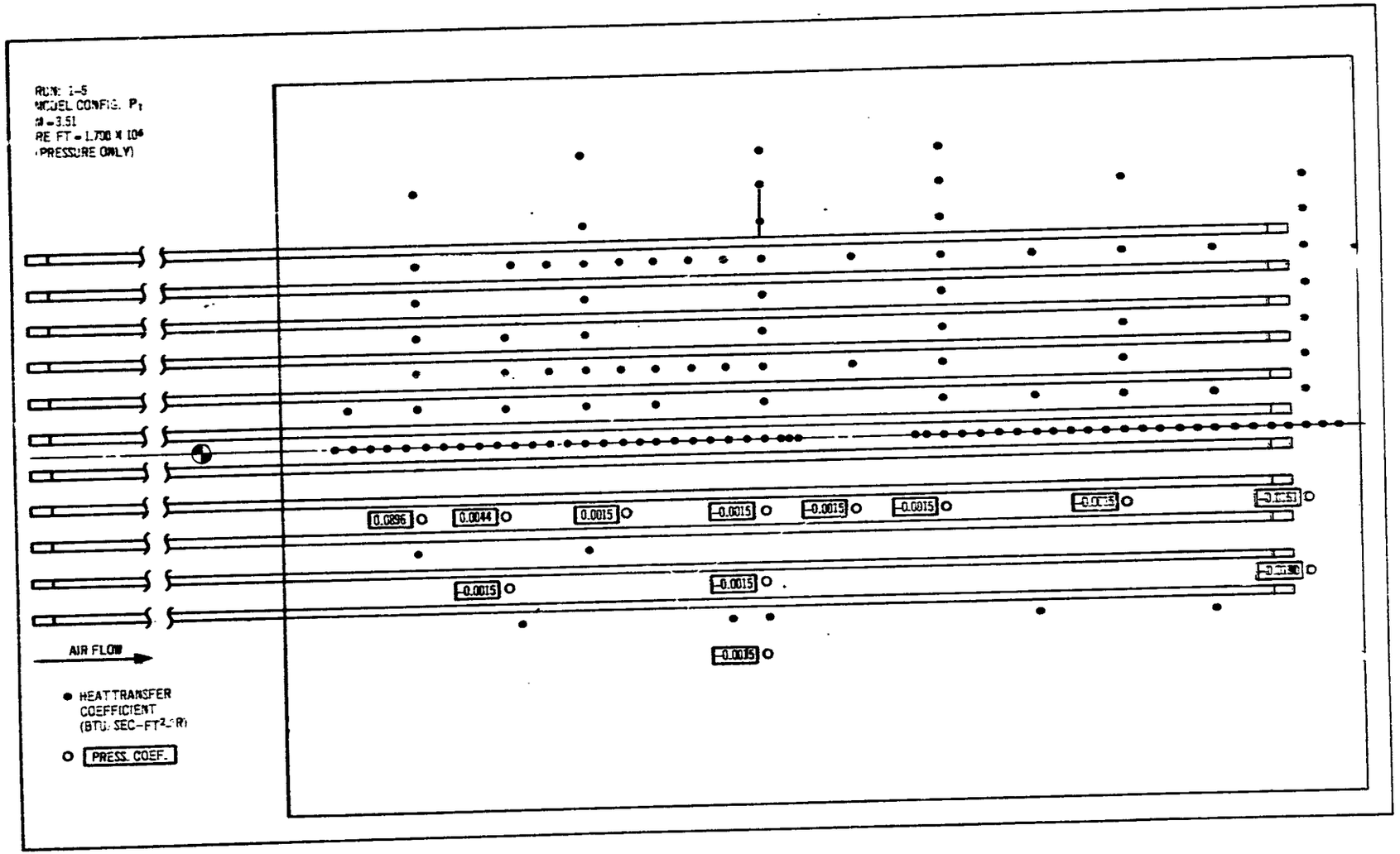

Figure 14. Langley Protuberance Heating Test-Pressure Coefficients; Calibration Runs

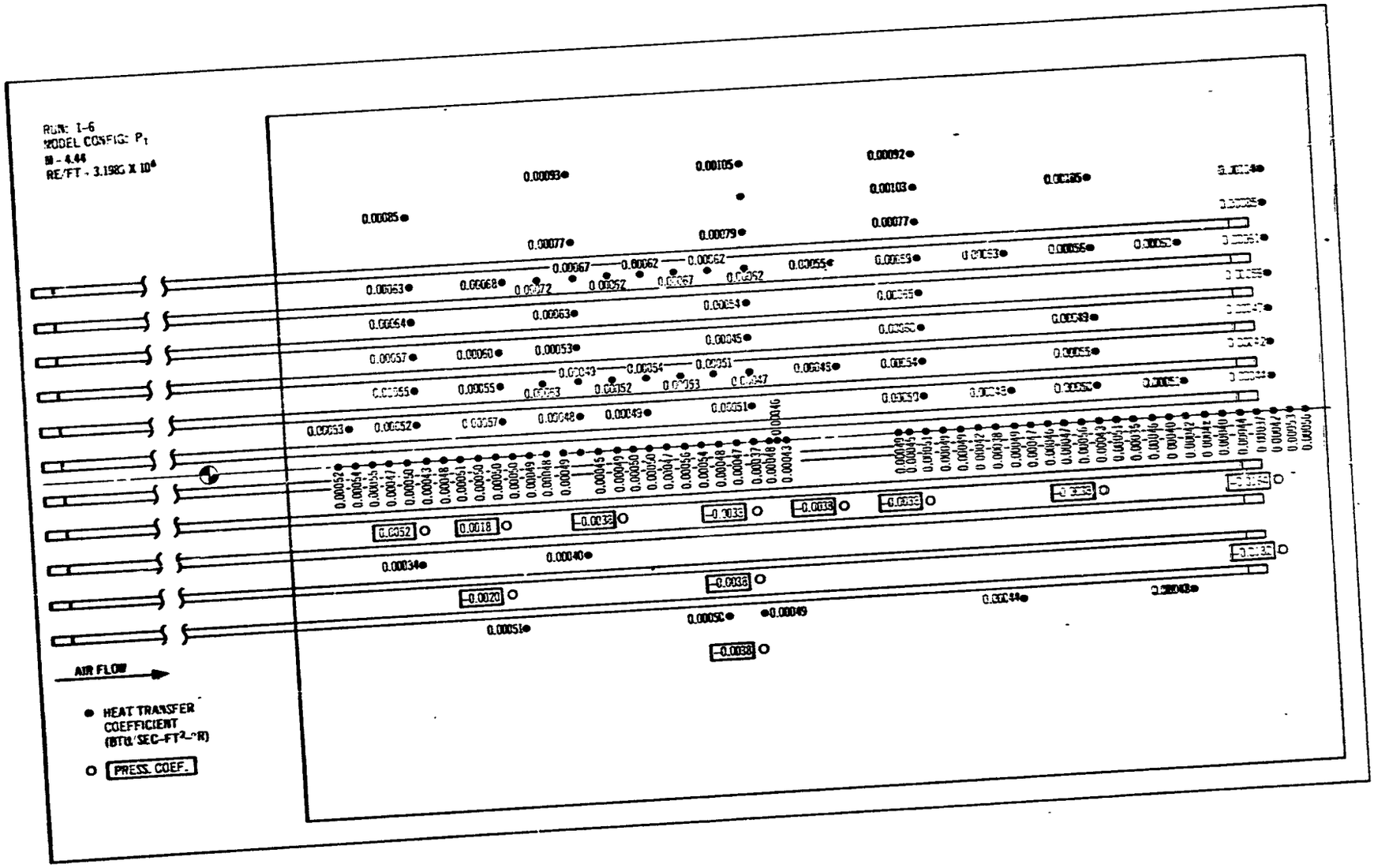

Figure 15. Langley Protuberance Heating Test-Heat Transfer Coefficients and Pressure Coefficients; Calibration Runs

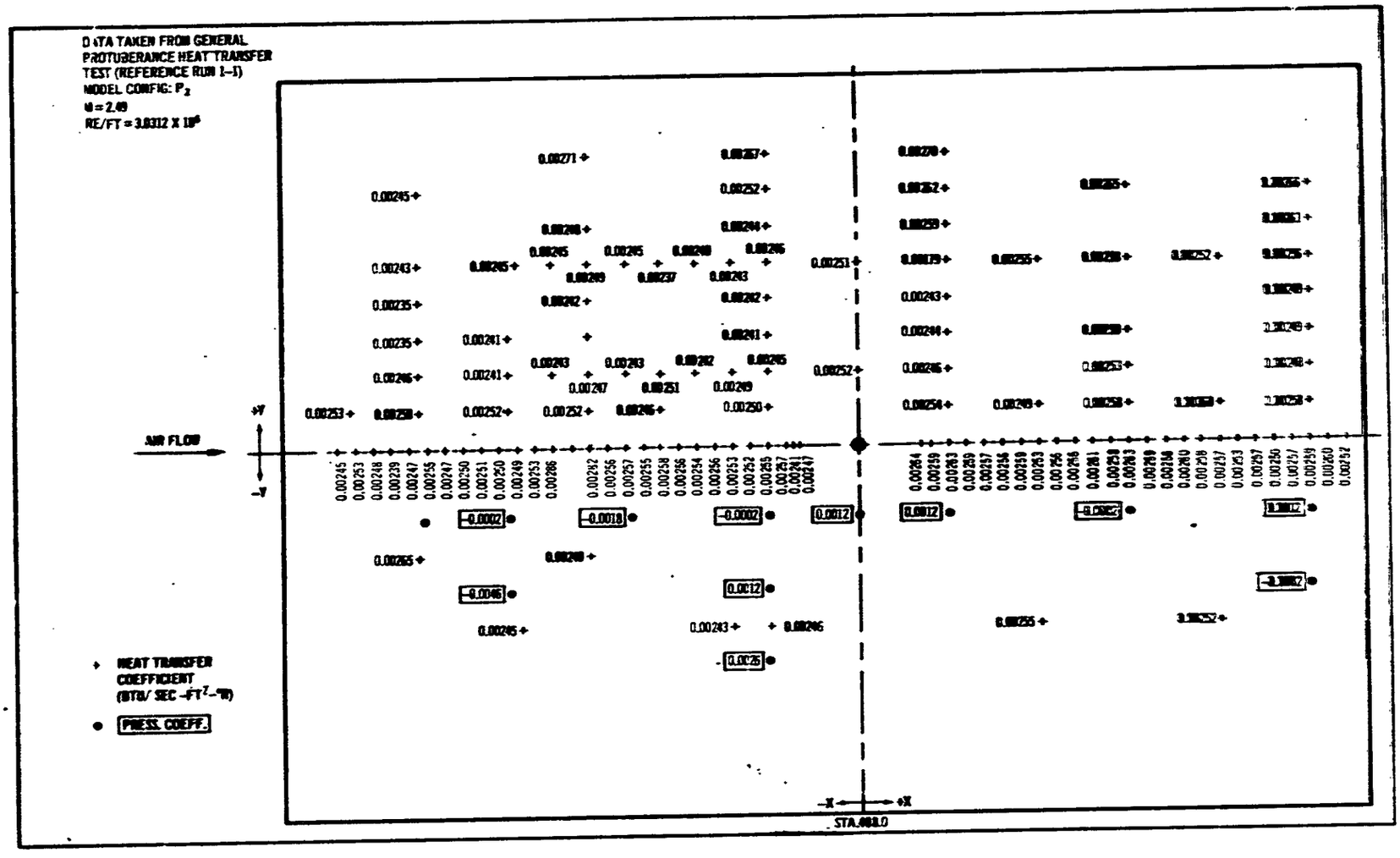

Figure 16. Langley Protuberance Heating Test-Heat Transfer Coefficients (h_c) and Pressure Coefficients on Smooth Plate

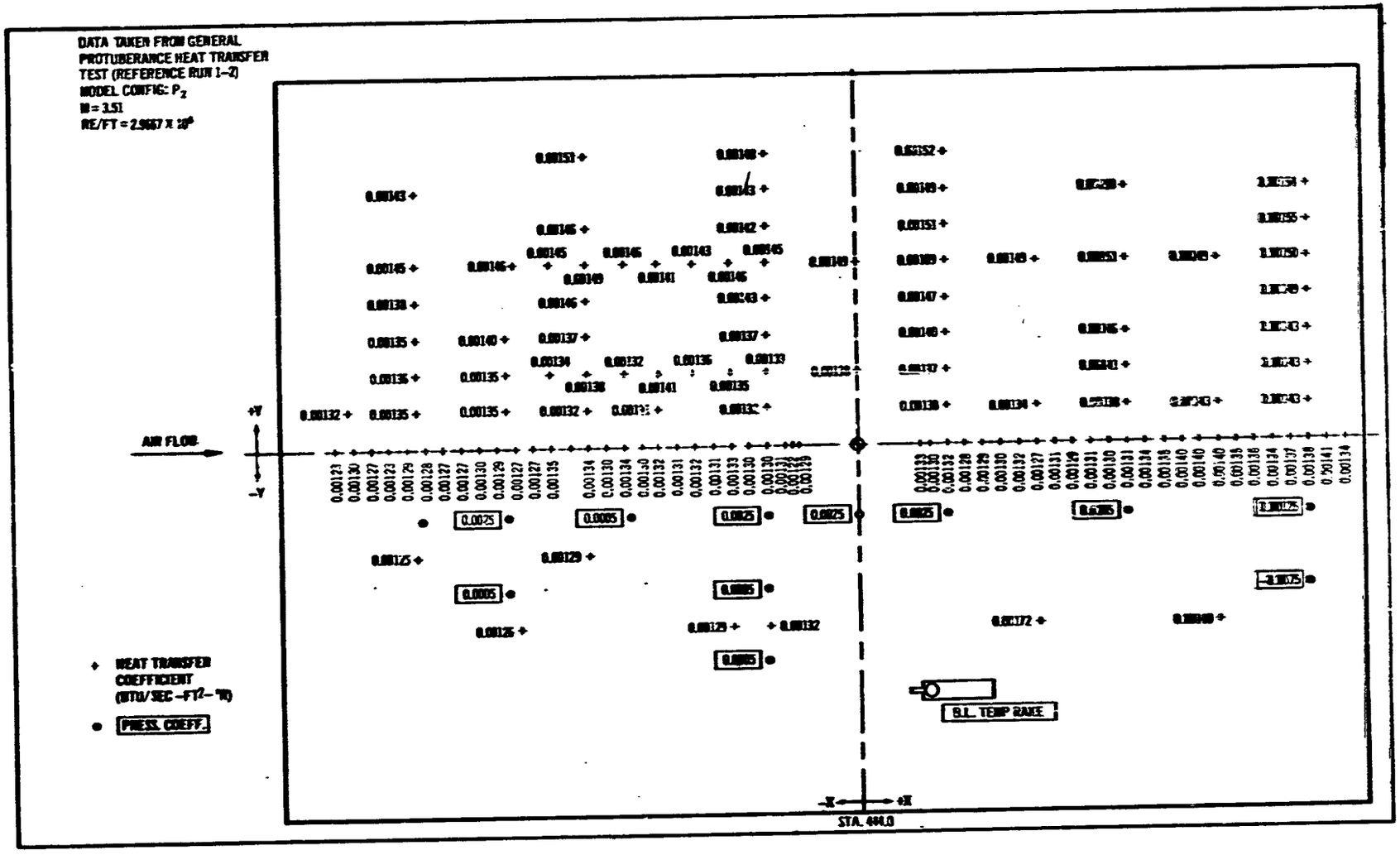

Figure 17. Langley Protuberance Heating Test-Heat Transfer Coefficients (h_C) and Pressure Coefficients on Smooth Plate

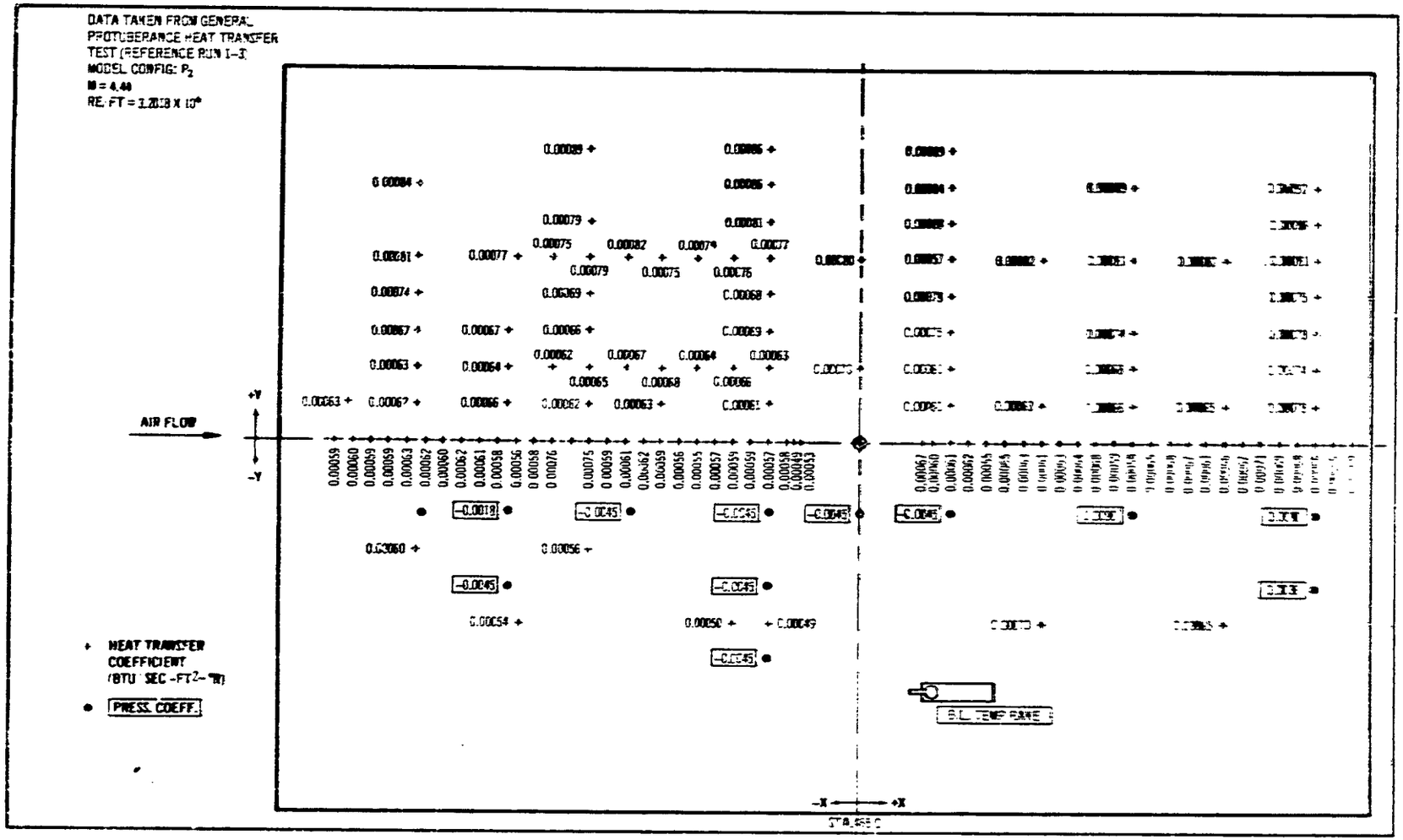

Figure 18. Langley Protuberance Heating Test-Heat Transfer Coefficients (h_C) and Pressure Coefficients on Smooth Plate

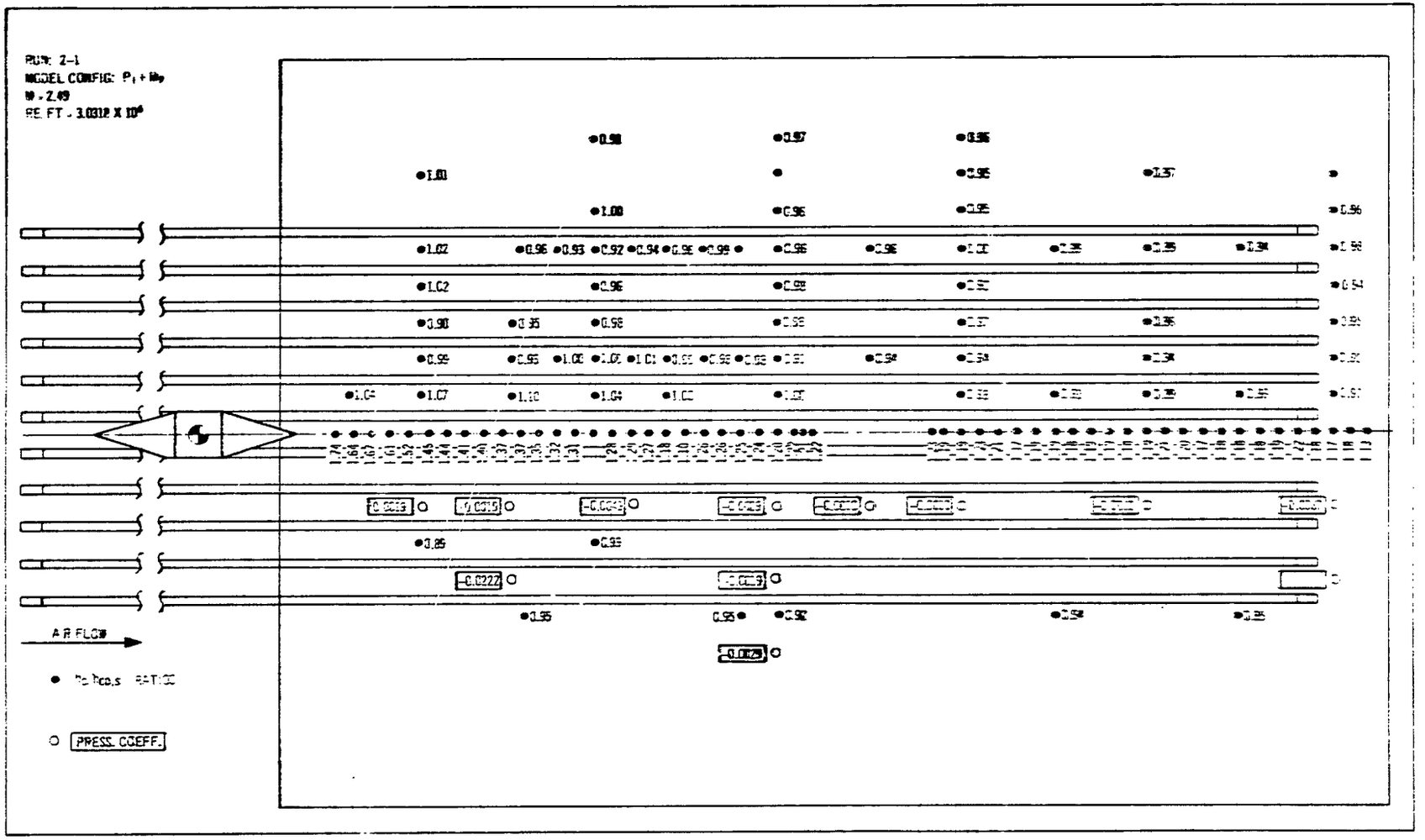

Figure 19. Langley Protuberance Heating Test-Heat Transfer Coefficient Ratios ($h_C/h_{CO,S}$) and Pressure Coefficients on Plate with Stringers

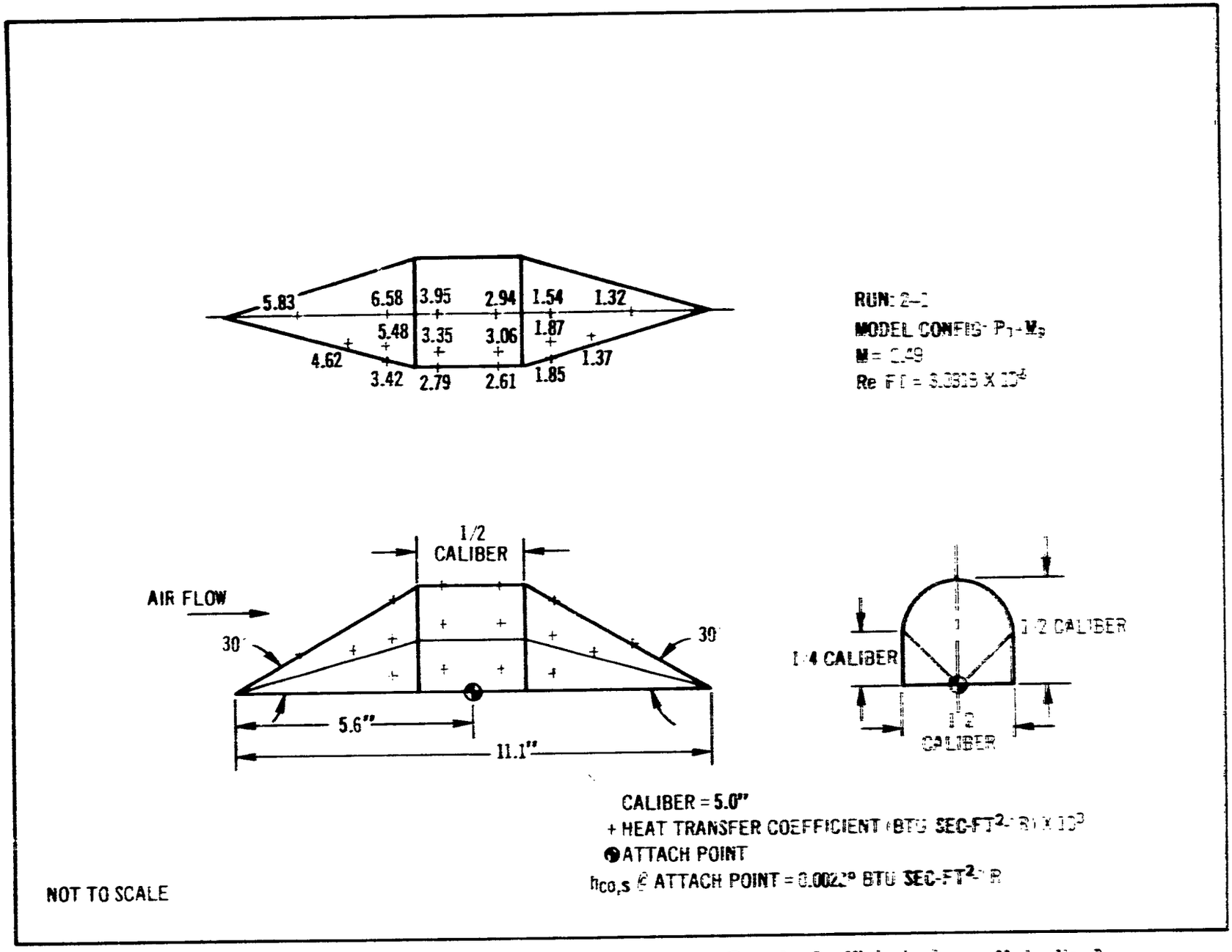

Figure 20. Langley Protuberance Heating Test-Heat Transfer Coefficients [illegible] Model No. 5

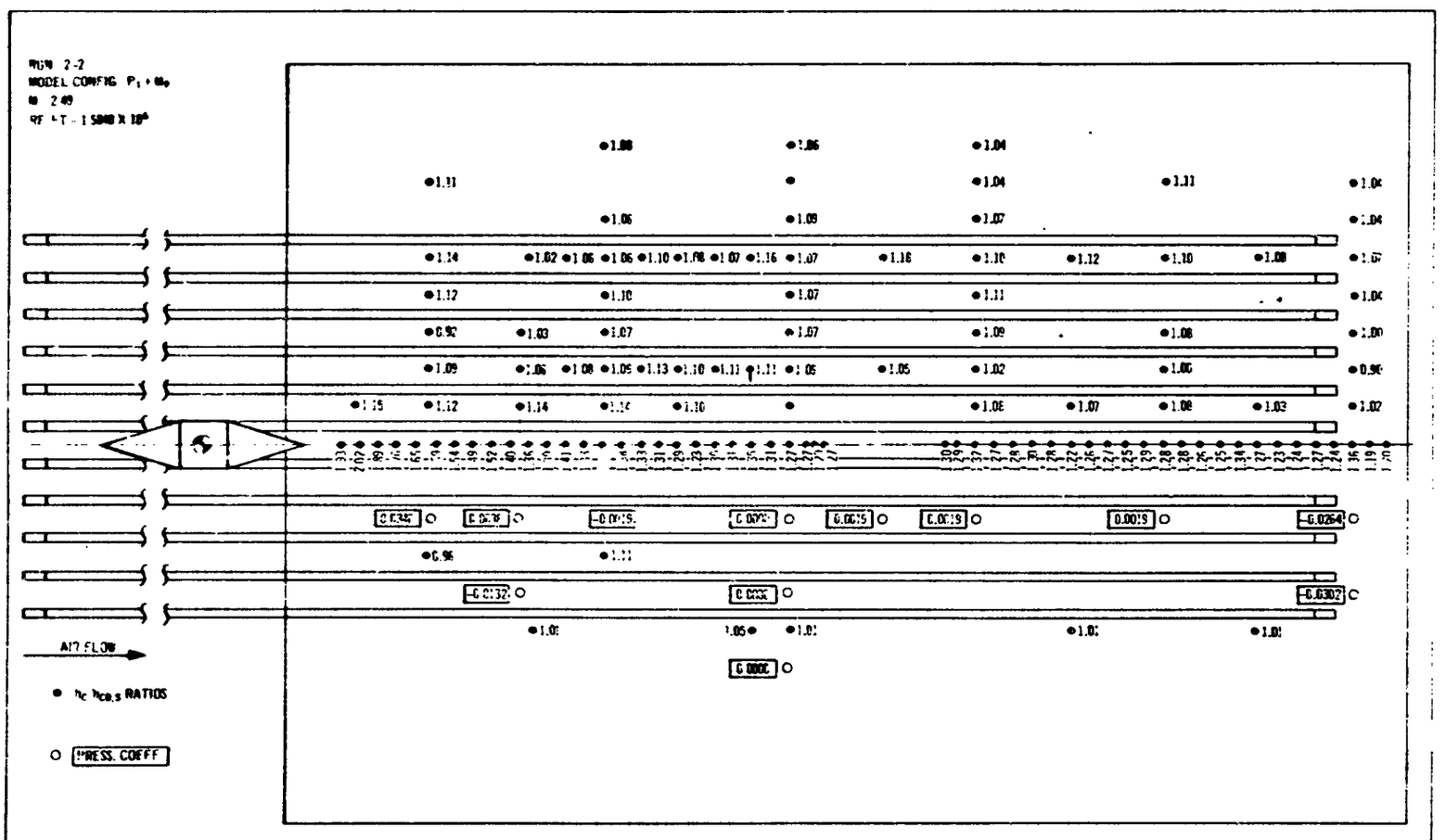

Figure 21. Langley Protuberance Heating Test-Heat Transfer Coefficient Ratios ($h_c/h_{co,s}$) and Pressure Coefficients on Plate with Stringers

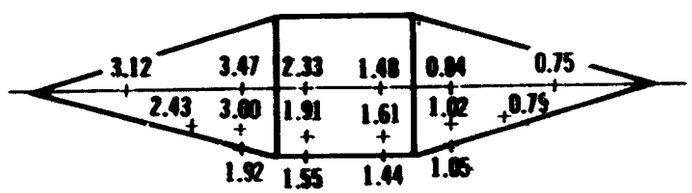

RUN: 2–2
MODEL CONFIG: $P_1 + M_9$
$M_\infty = 3.51$
$Re/FT = 1.5840 \times 10^6$

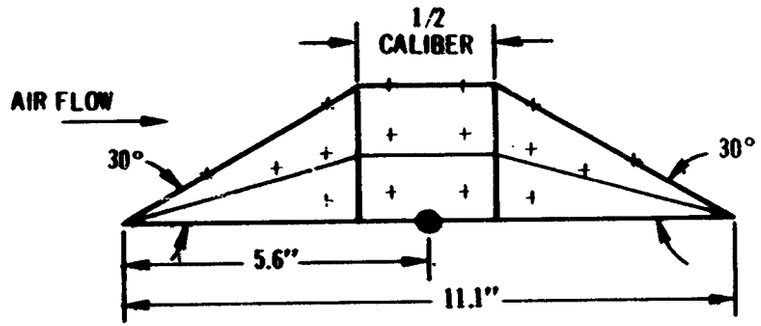

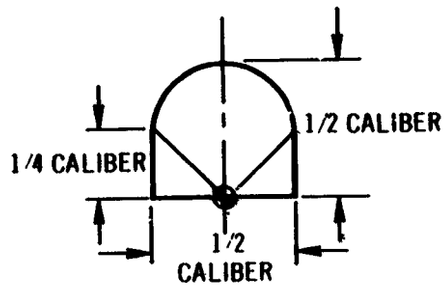

CALIBER =
+ HEAT TRANSFER COEFFICIENT (BTU/SEC-FT^{2}-° R) X 10^3
⊕ ATTACH POINT
$h_{co,s}$ @ ATTACH POINT = 0.00056 BTU/SEC-FT^{2}-° R

NOT TO SCALE

Figure 22. Langley Protuberance Heating Test-Heat Transfer Coefficients (h_C) on Model No. 9

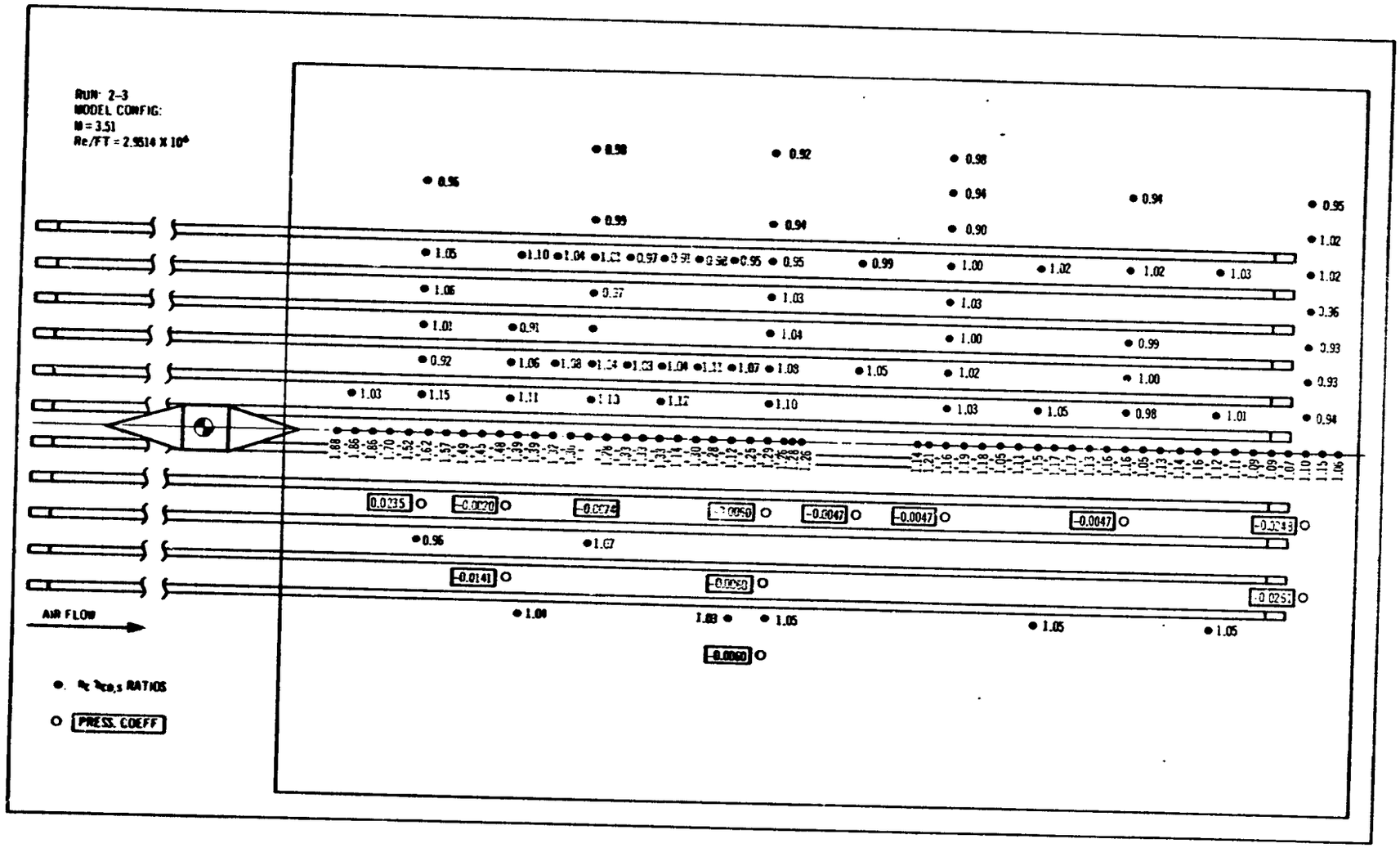

Figure 23. Langley Protuberance Heating Test-Heat Transfer Coefficient Ratios ($h_c/h_{co,s}$) and Pressure Coefficients on Plate with Stringers

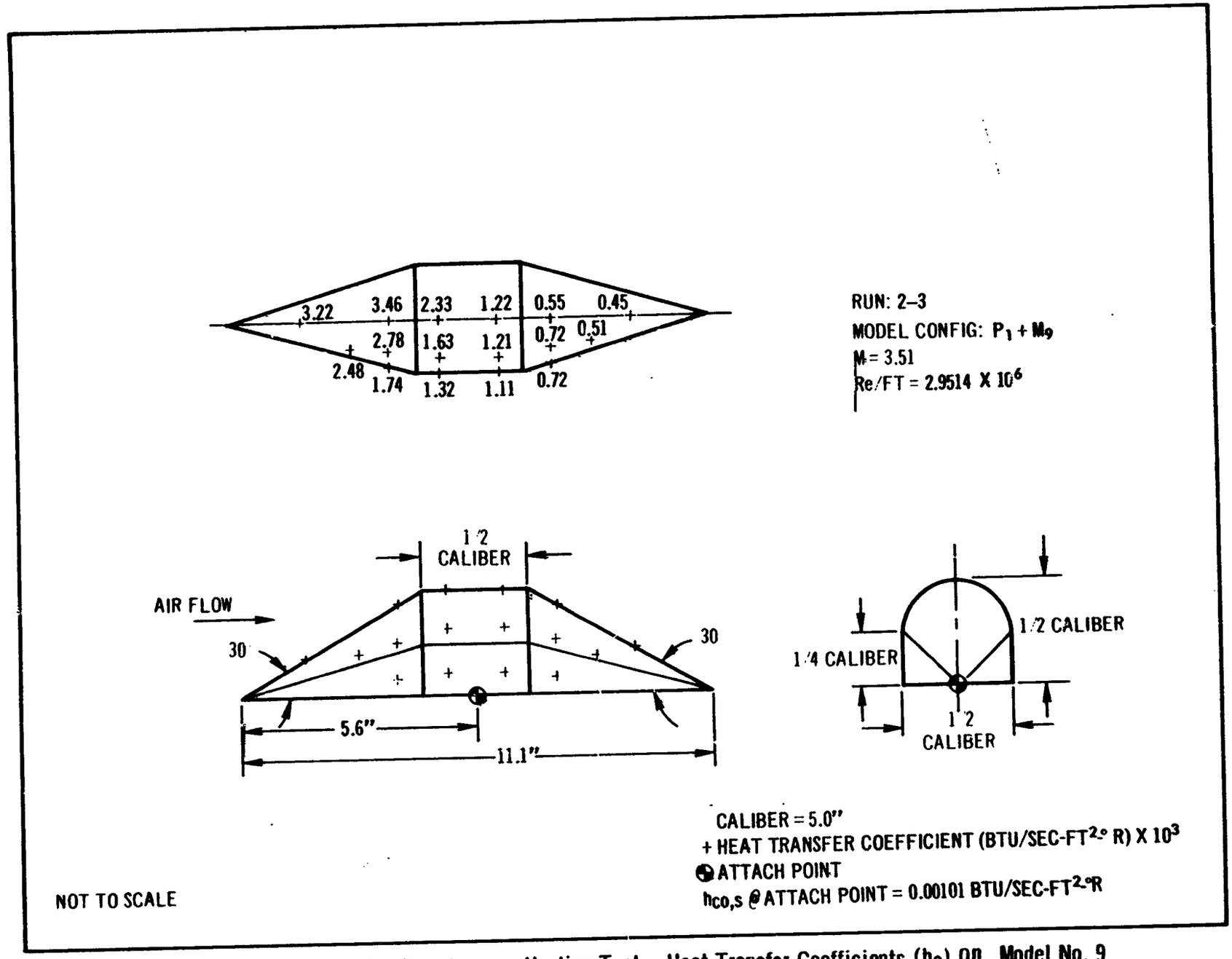

Figure 24. Langley Protuberance Heating Test – Heat Transfer Coefficients (h_C) on Model No. 9

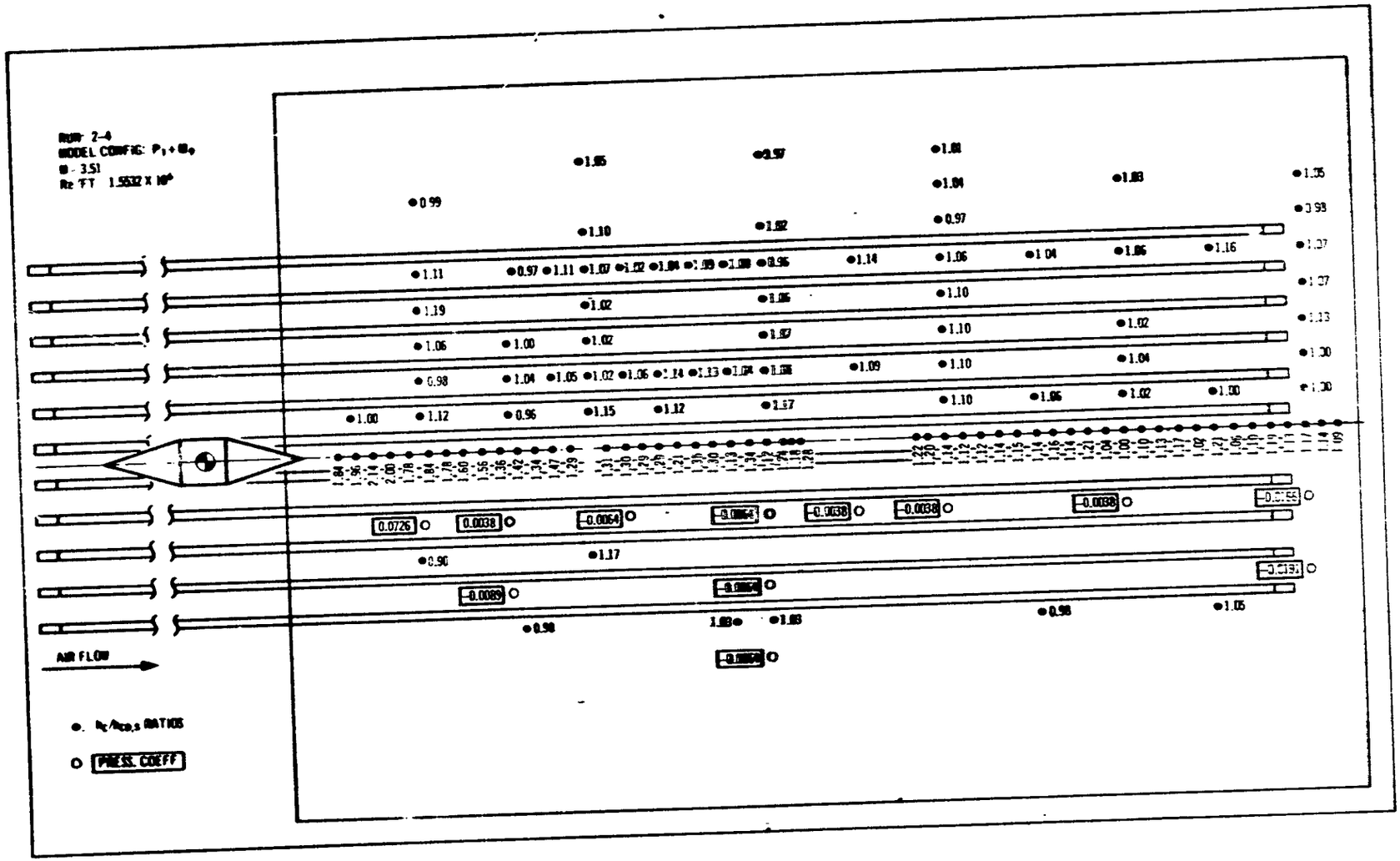

Figure 25. Langley Protuberance Heating Test-Heat Transfer Coefficient Ratios ($h_c/h_{co,s}$) and Pressure Coefficients on Plate with Stringers

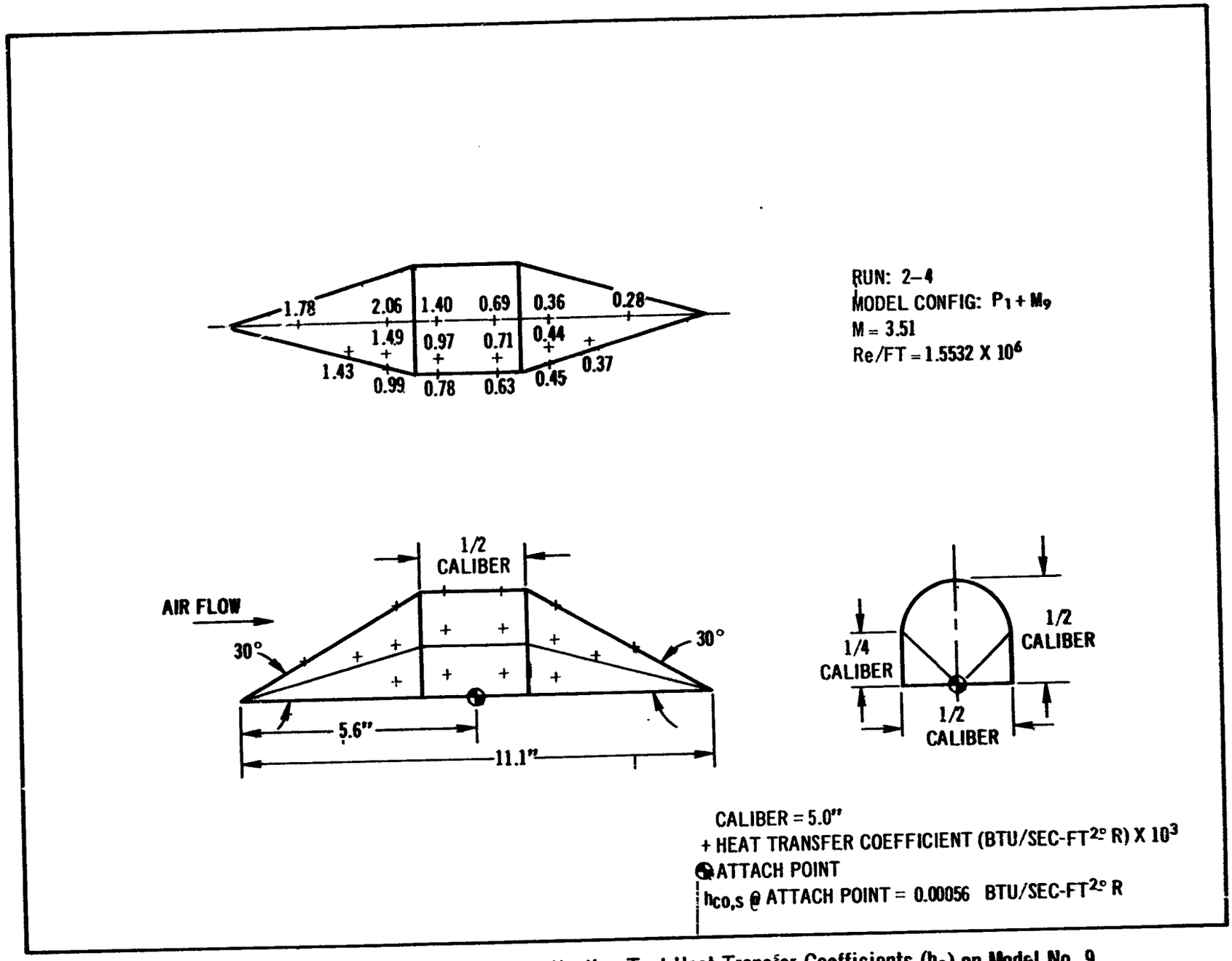

Figure 26. Langley Protuberance Heating Test-Heat Transfer Coefficients (h_C) on Model No. 9

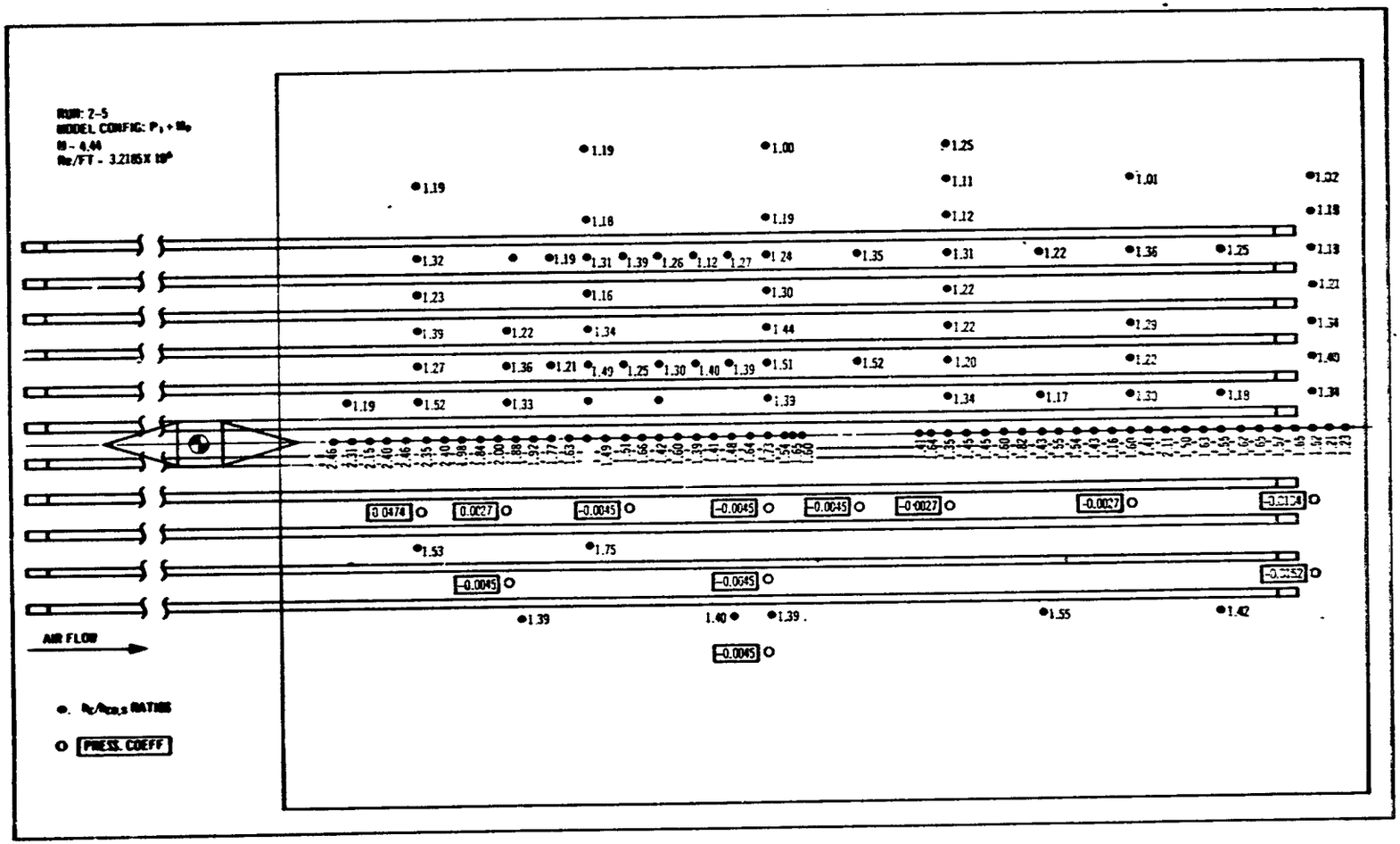

Figure 27. Langley Protuberance Heating Test-Heat Transfer Coefficient Ratios ($h_g/h_{co,s}$) and Pressure Coefficients on Plate with Stringers

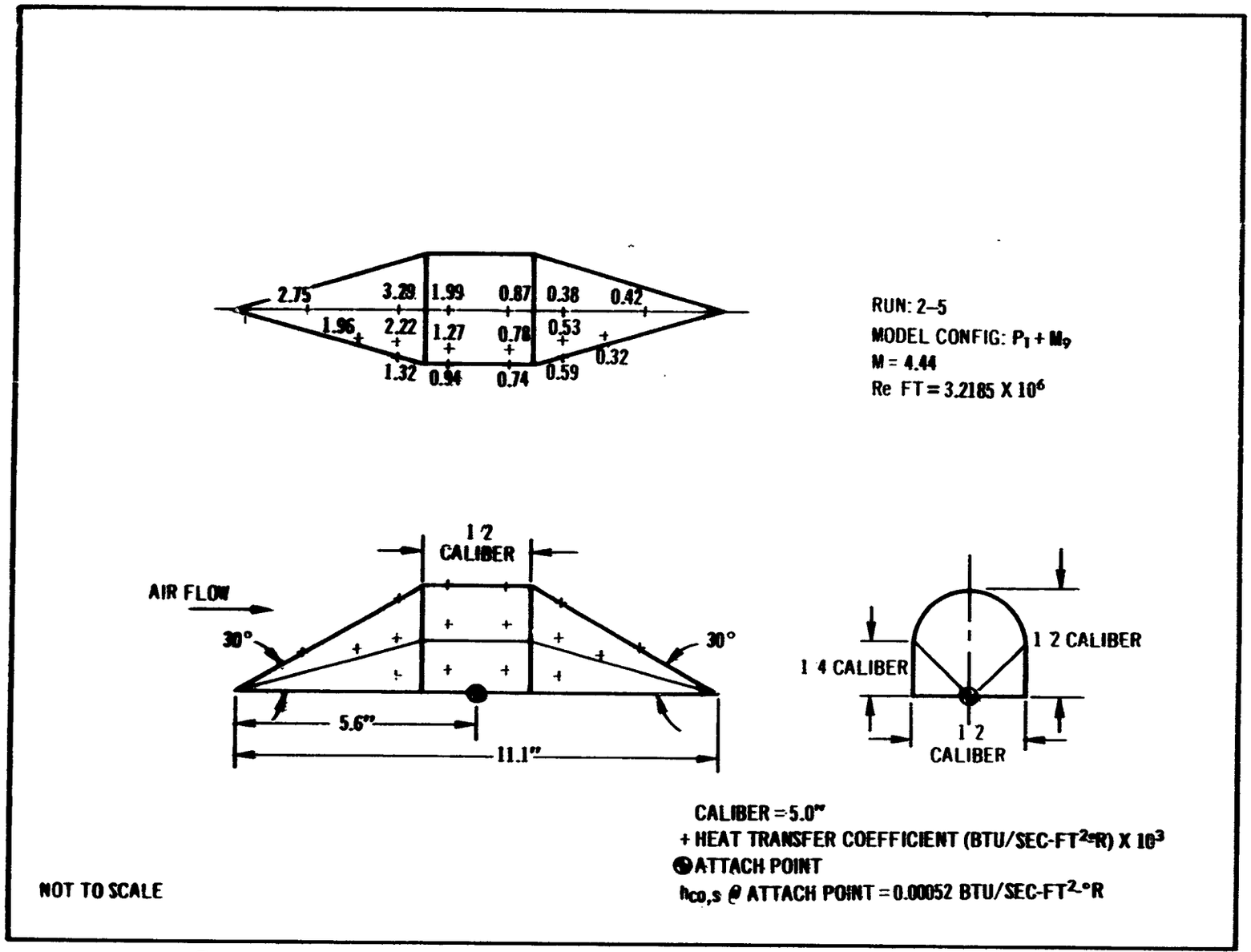

Figure 28. Langley Protuberance Heating Test-Heat Transfer Coefficients (h_c) on Model No. 9

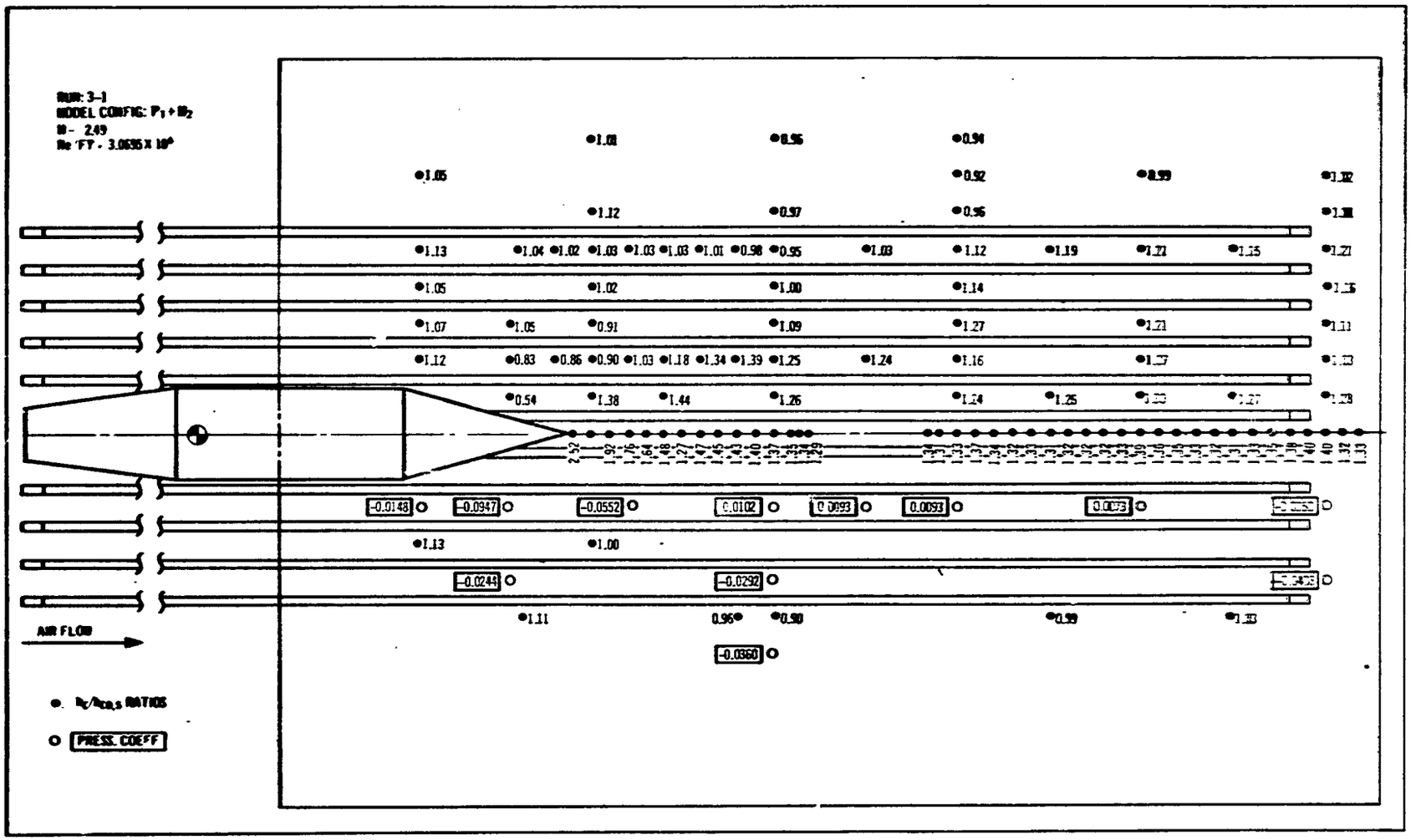

Figure 29. Langley Protuberance Heating Test-Heat Transfer Coefficient Ratios ($h_C/h_{CO,S}$) and Pressure Coefficients on Plate with Stringers

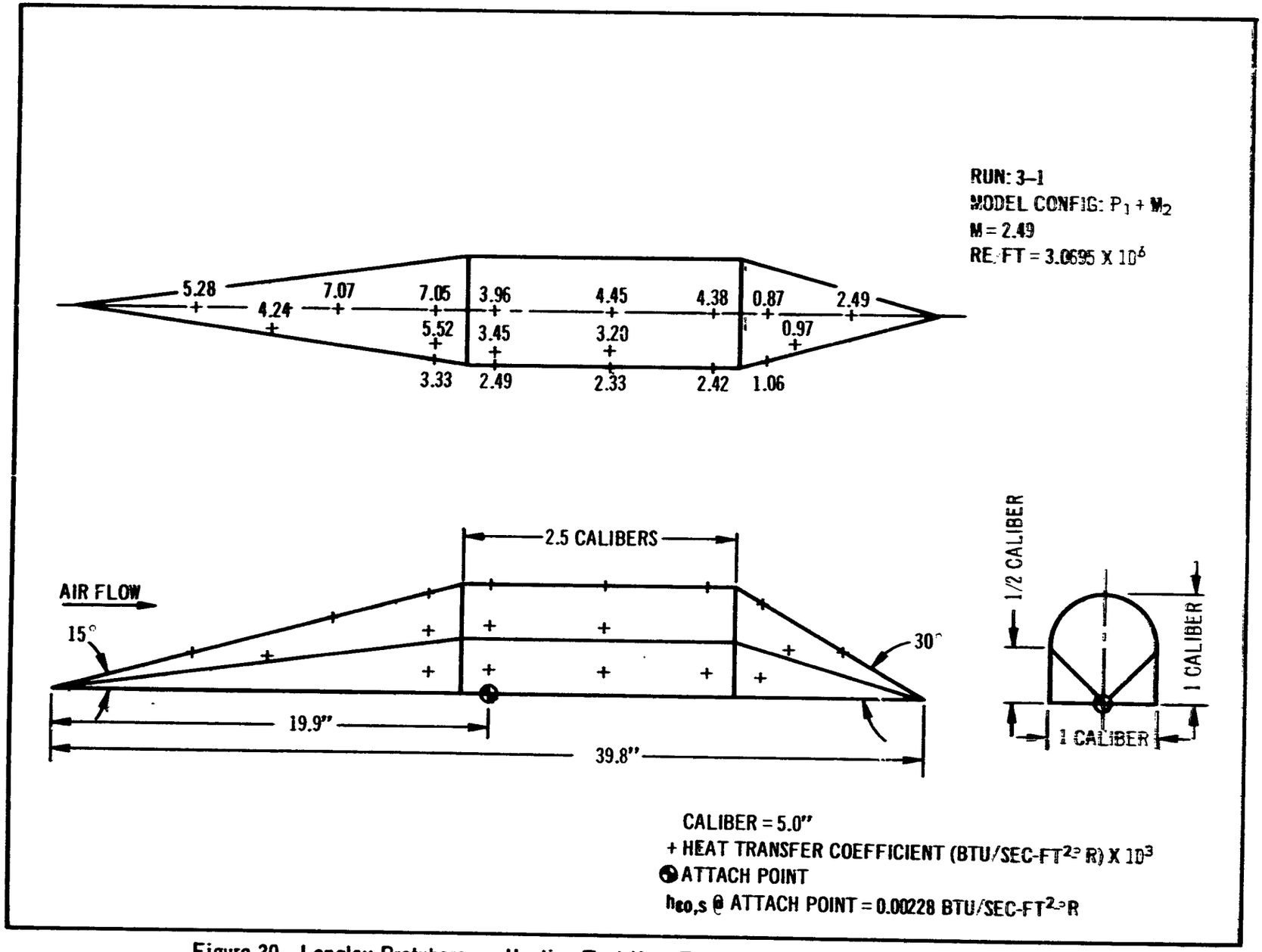

Figure 30. Langley Protuberance Heating Test-Heat Transfer Coefficients (h_c) on Model No. 2

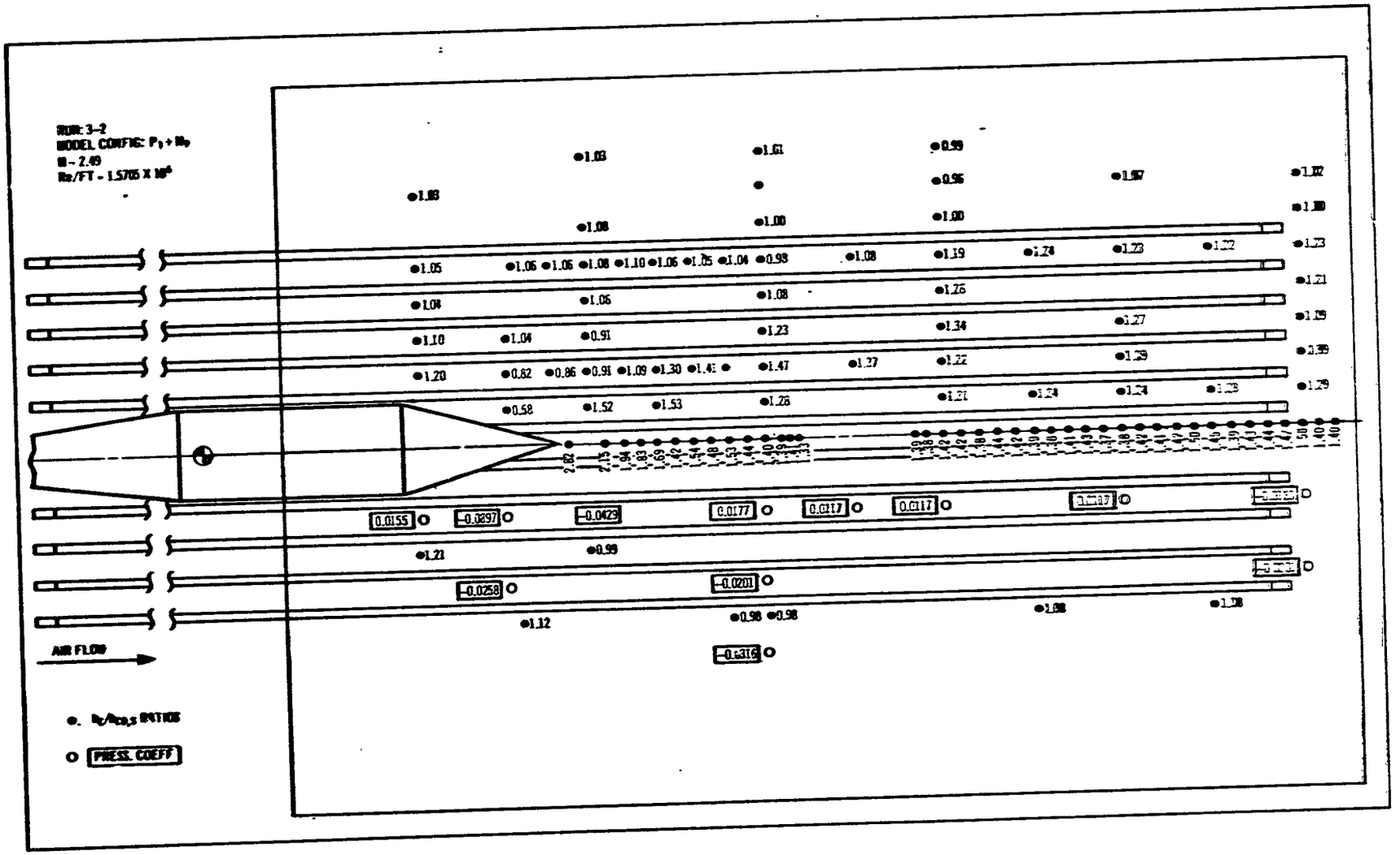

Figure 31. Langley Protuberance Heating Test-Heat Transfer Coefficient Ratios ($h_{\ell}/h_{co,s}$) and Pressure Coefficients on Plate with Stringers

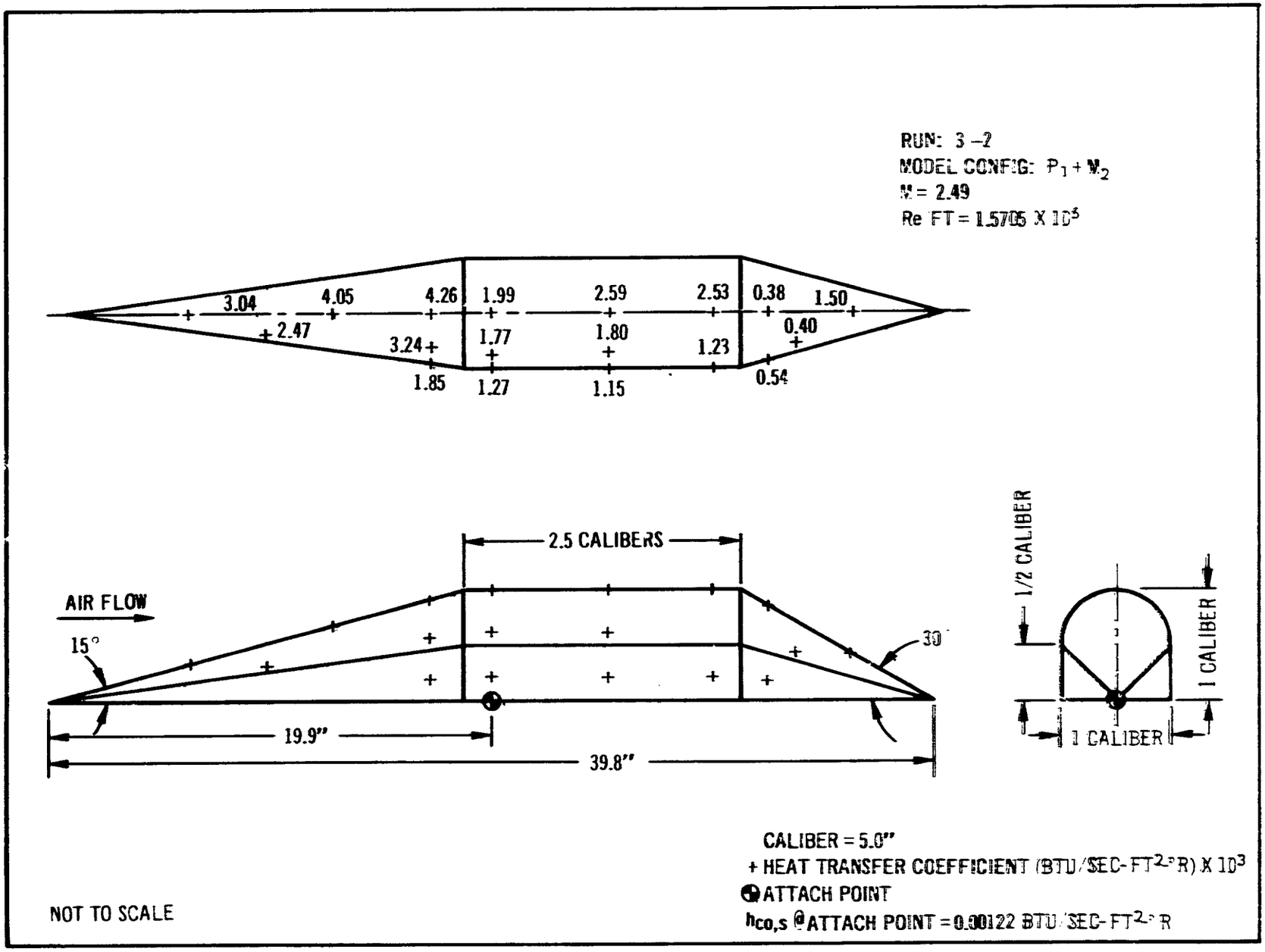

Figure 32. Langley Protuberance Heating Test-Heat Transfer Coefficients (h_C) on Model No. 2

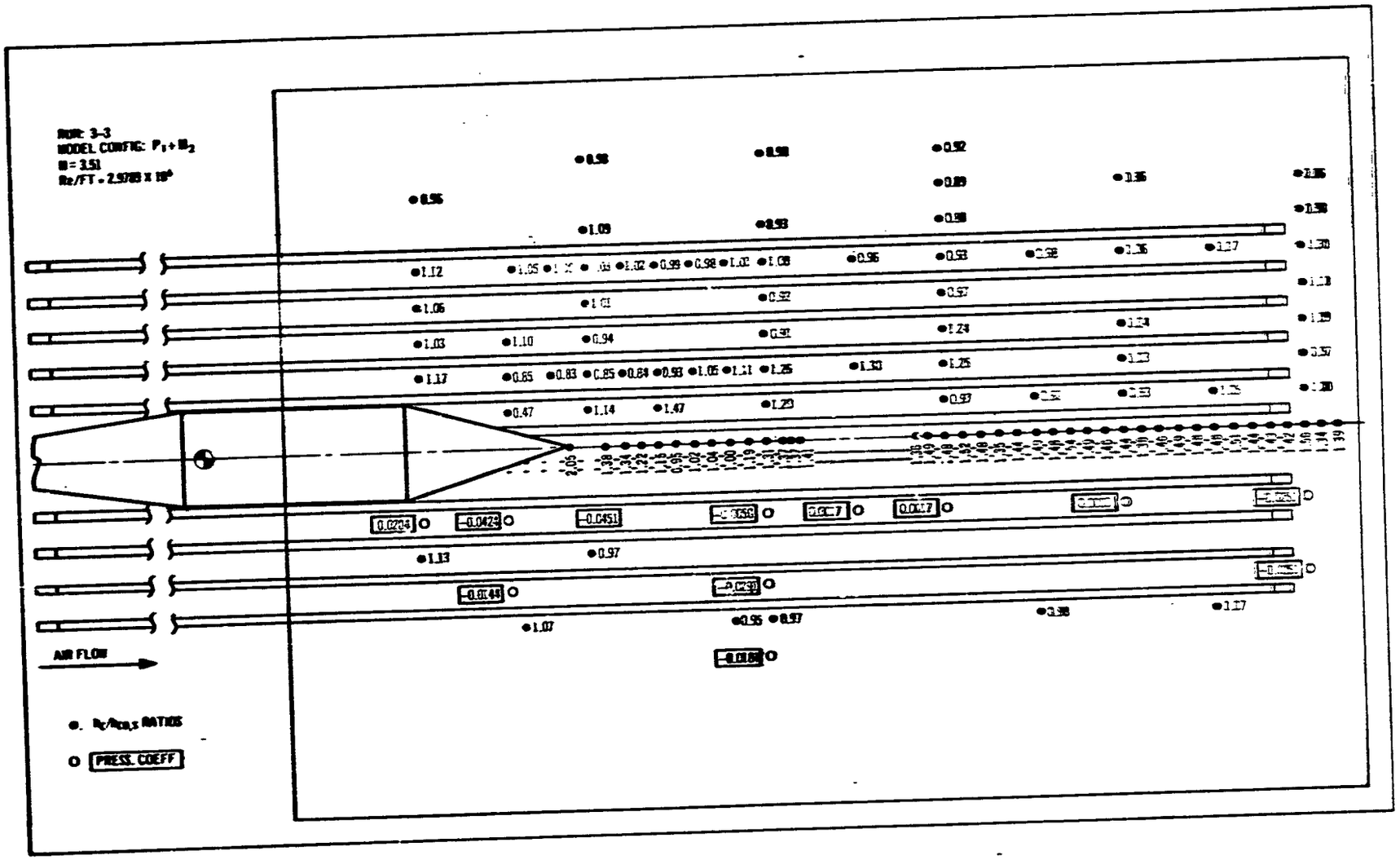

Figure 33. Langley Protuberance Heating Test-Heat Transfer Coefficient Ratios ($h_c/h_{co,s}$) and Pressure Coefficients on Plate with Stringers

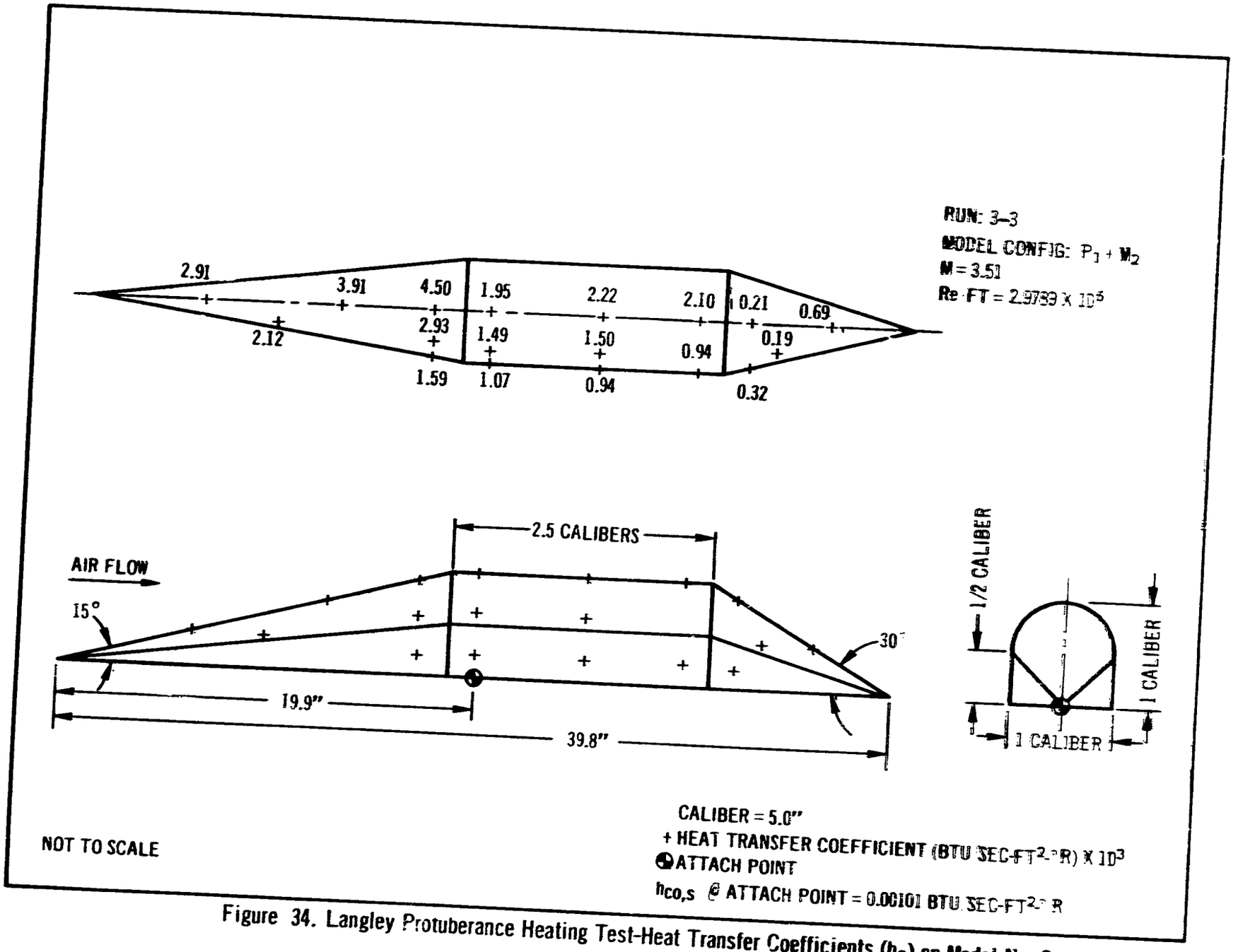

Figure 34. Langley Protuberance Heating Test-Heat Transfer Coefficients (h_C) on Model No. 2

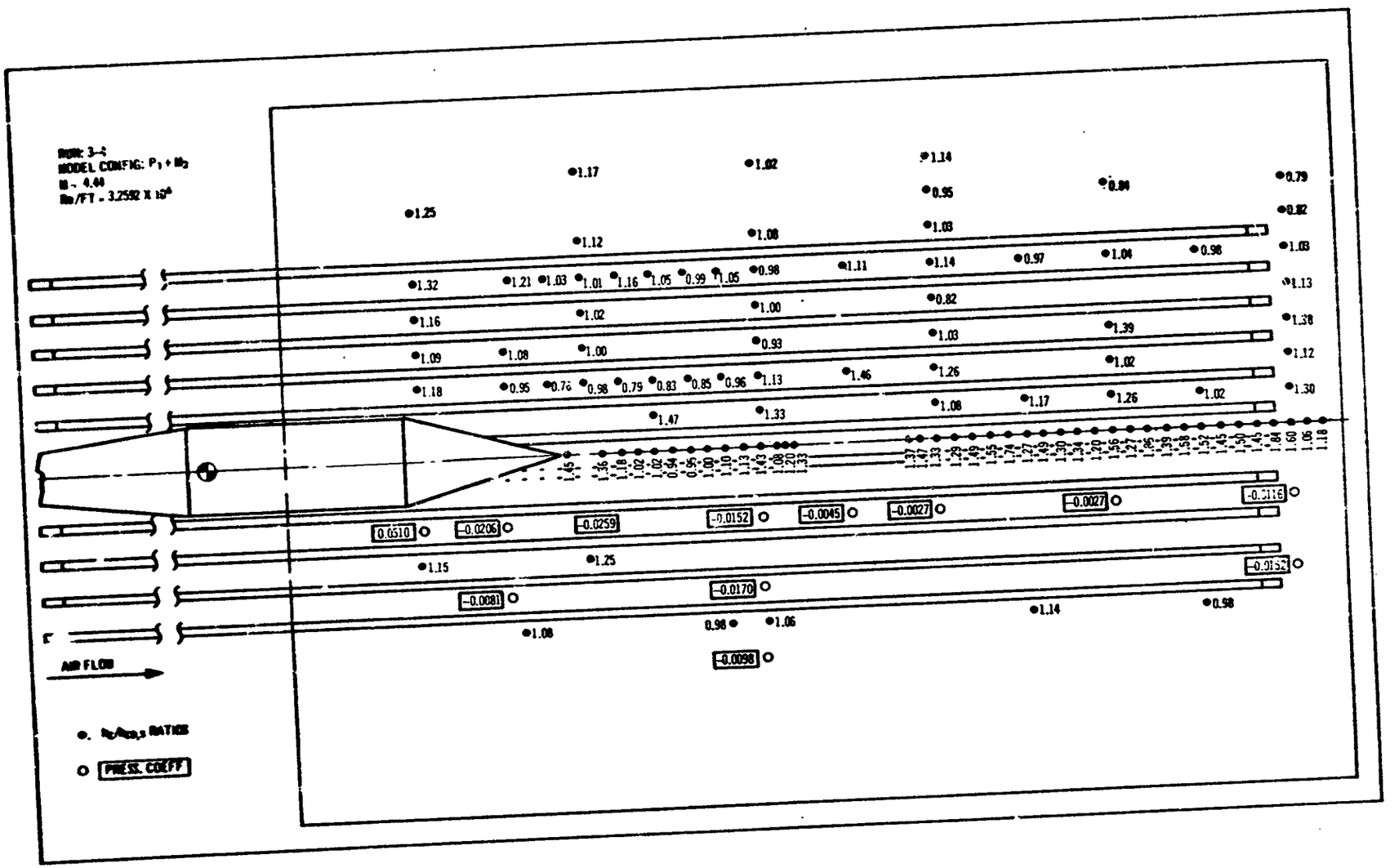

Figure 35. Langley Protuberance Heating Test-Heat Transfer Coefficient Ratios ($h_c/h_{co,s}$) and Pressure Coefficients on Plate with Stringers

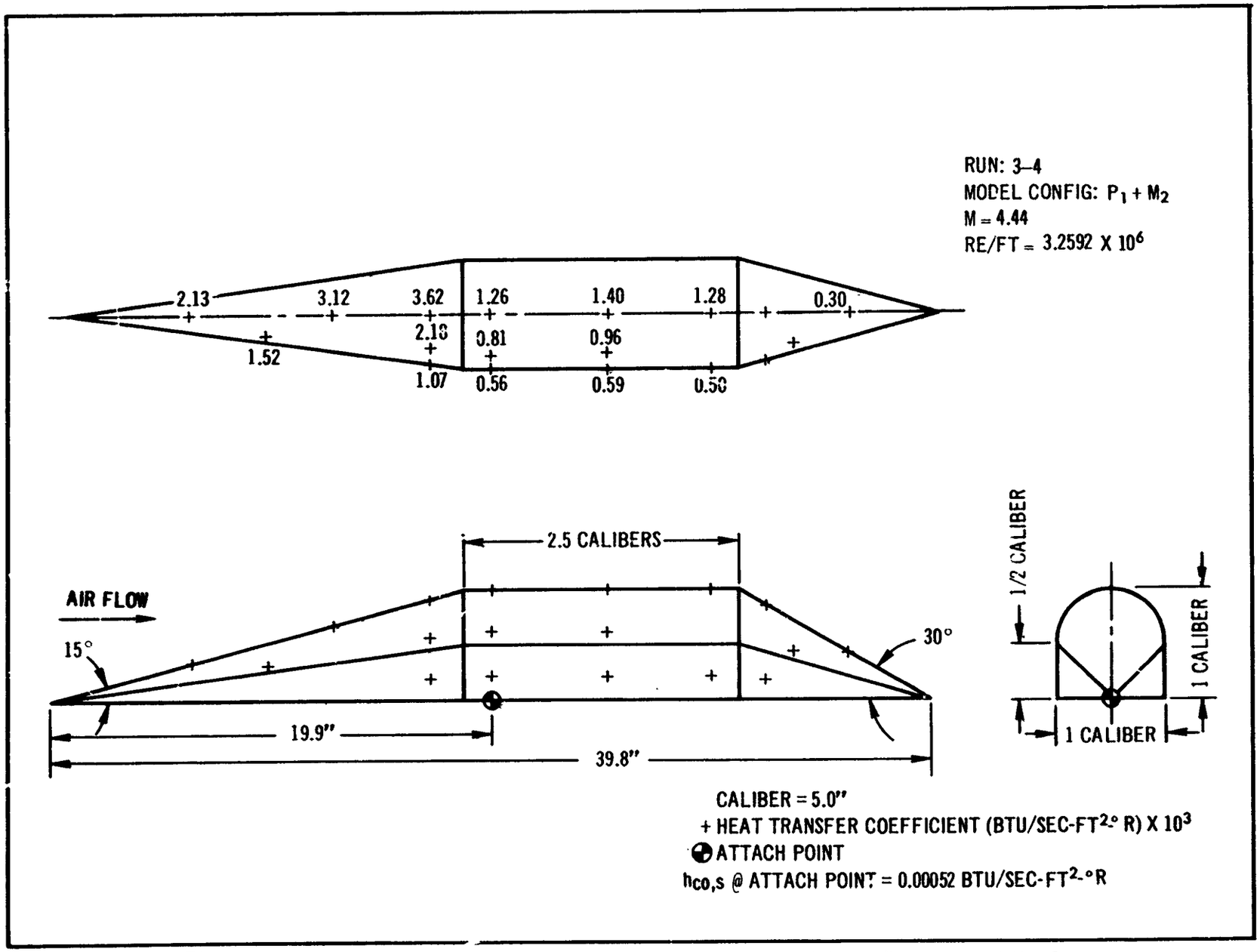

Figure 36. Langley Protuberance Heating Test-Heat Transfer Coefficients (h_C) on Model No. 2

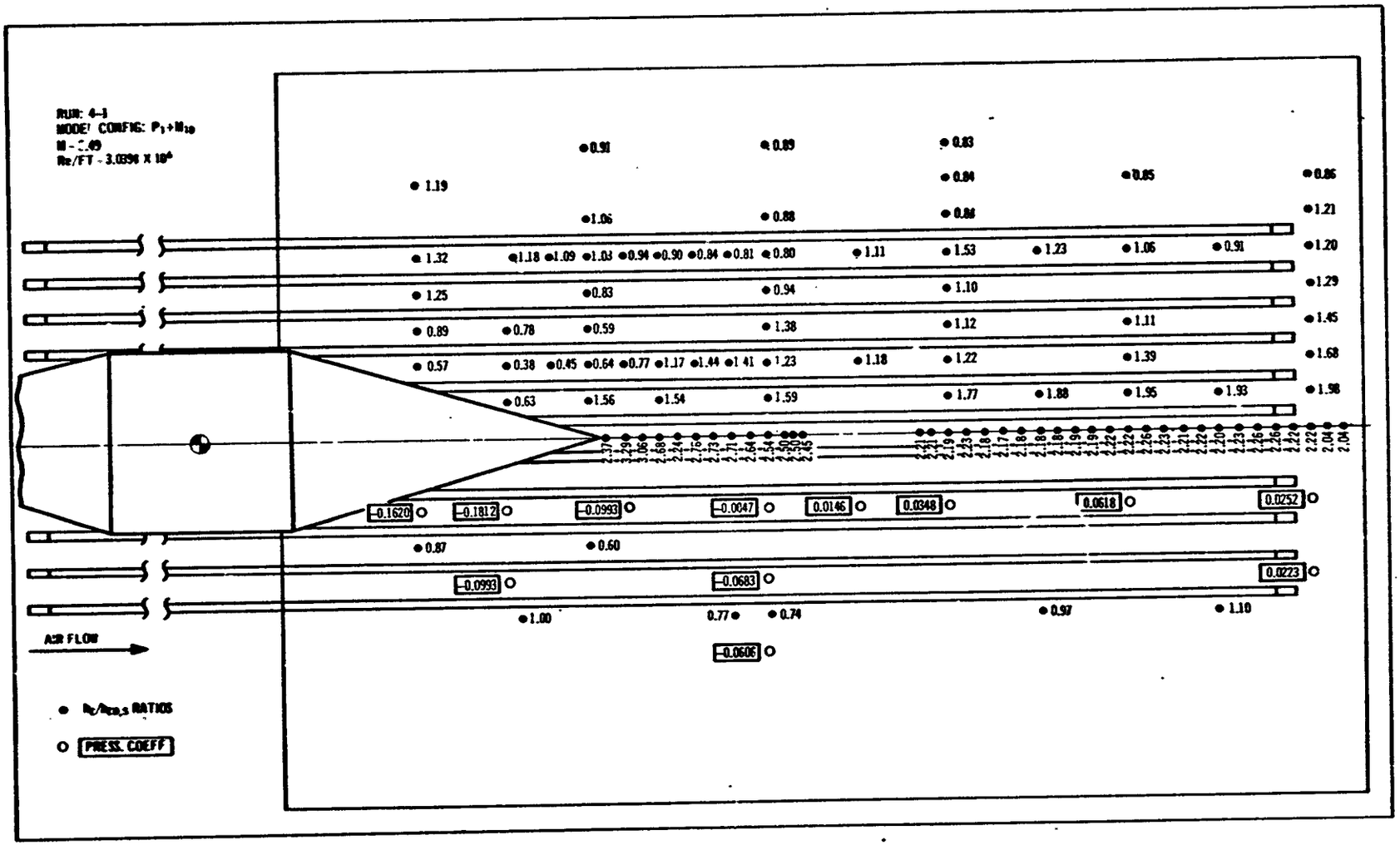

Figure 37. Langley Protuberance Heating Test-Heat Transfer Coefficient Ratios ($h_c/h_{co,s}$) and Pressure Coefficients on Plate with Stringers

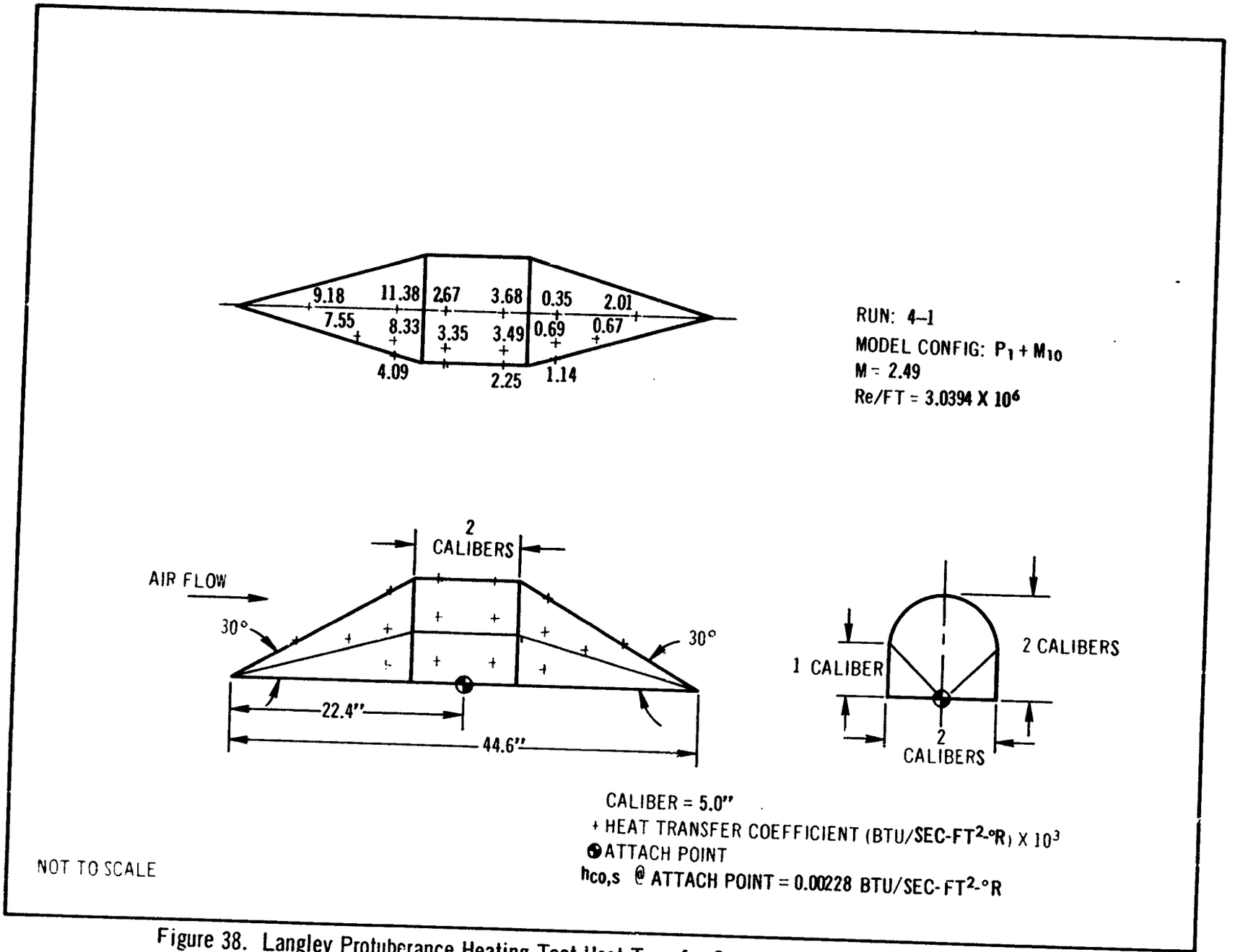

Figure 38. Langley Protuberance Heating Test-Heat Transfer Coefficients (h_c) on Model No. 10

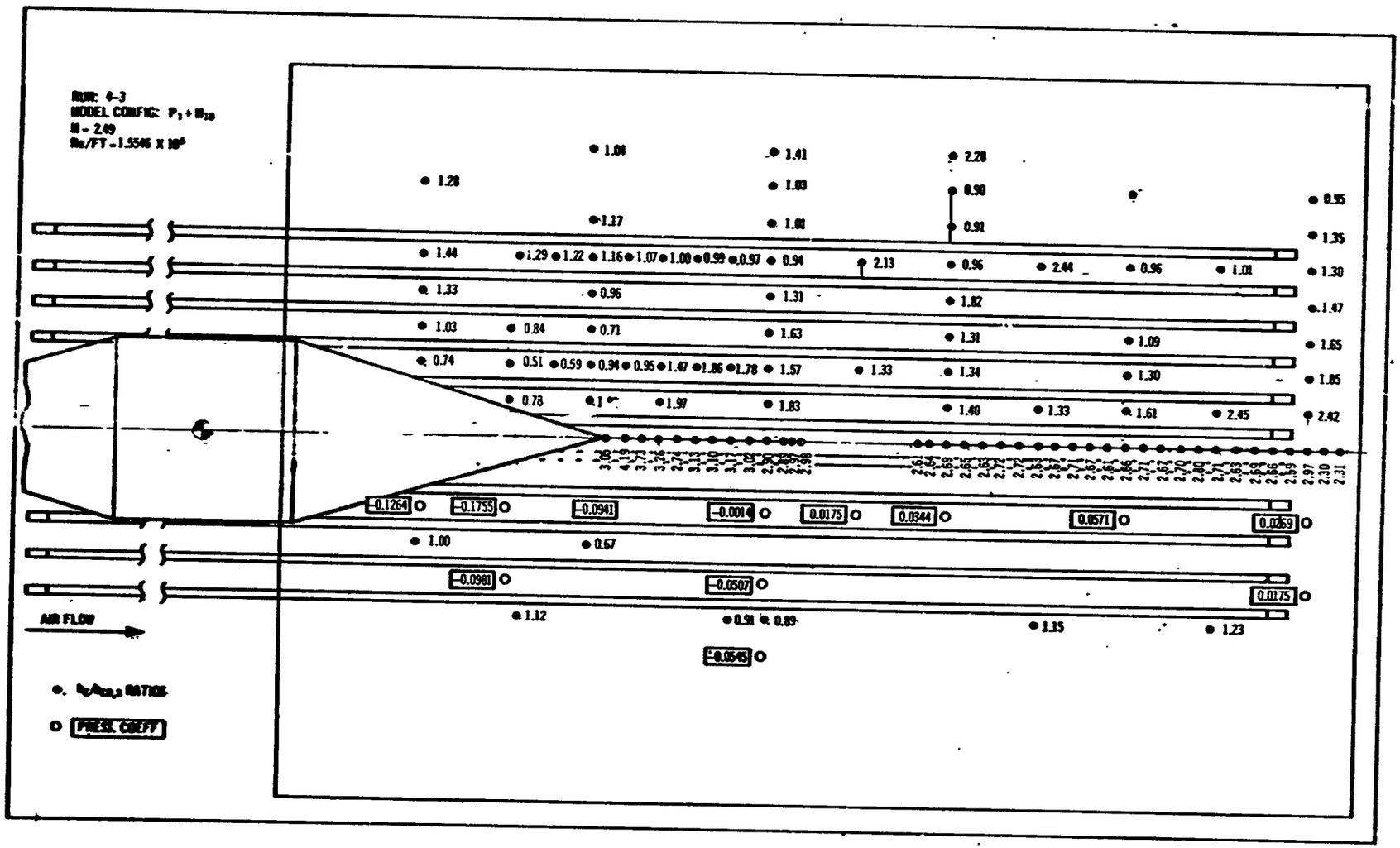

Figure 39. Langley Protuberance Heating Test-Heat Transfer Coefficient Ratios ($h_c/h_{co,s}$) and Pressure Coefficients on Plate with Stringers

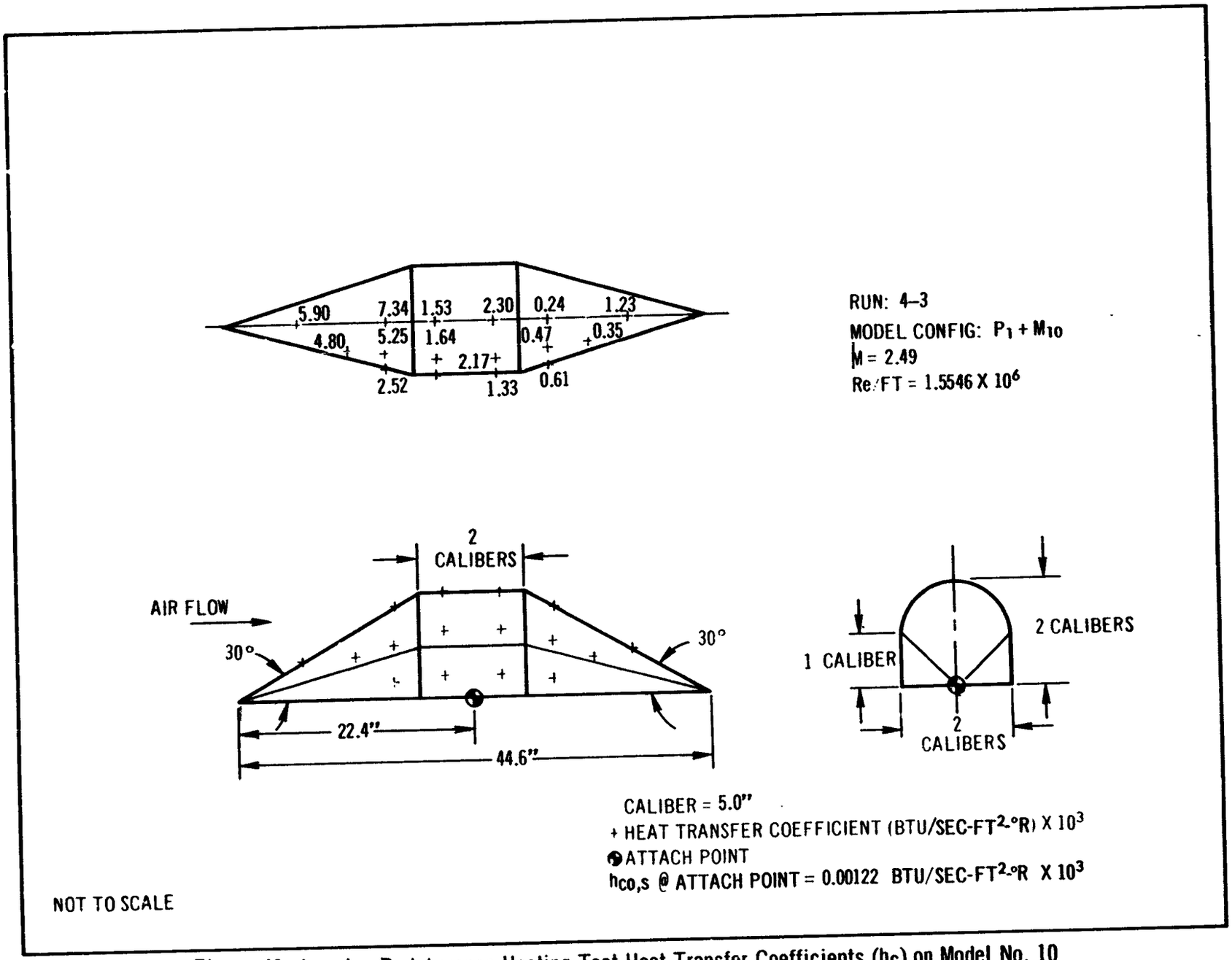

Figure 40. Langley Protuberance Heating Test-Heat Transfer Coefficients (h_c) on Model No. 10

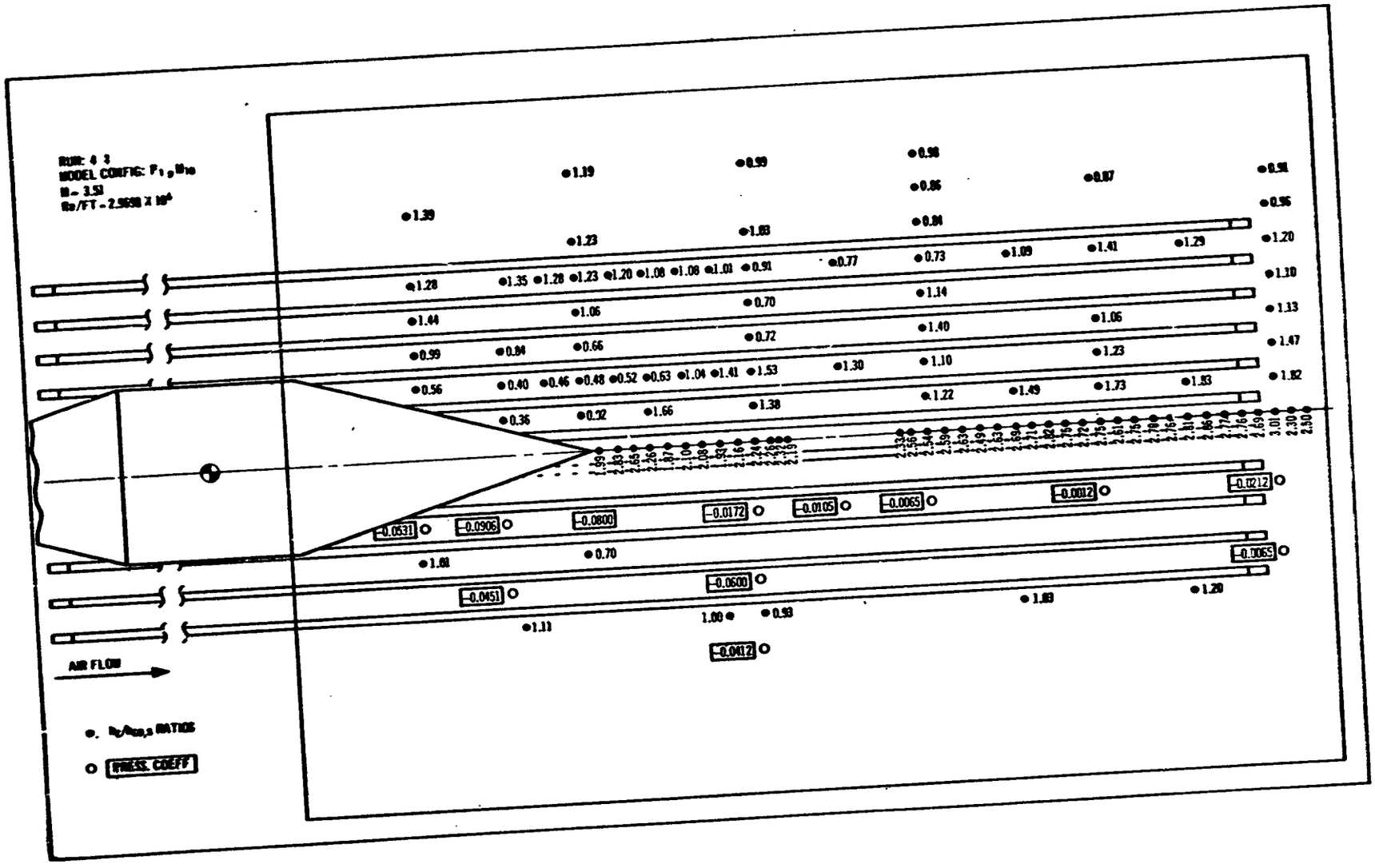

Figure 41. Langley Protuberance Heating Test-Heat Transfer Coefficient Ratios ($h_c/h_{co,s}$) and Pressure Coefficients on Plate with Stringers

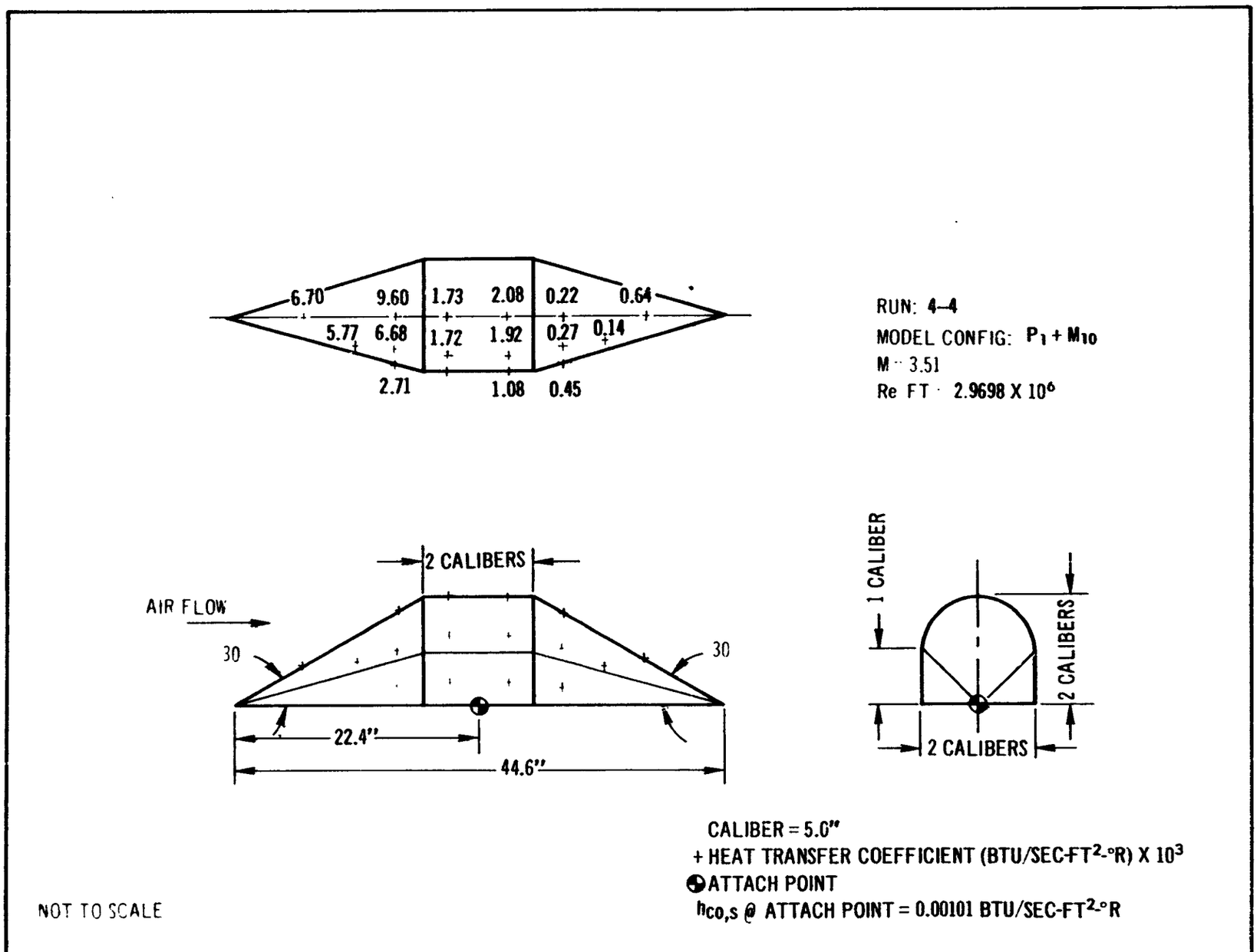

Figure 42. Langley Protuberance Heating Test-Heat Transfer Coefficients (h_C) on Model No. 10

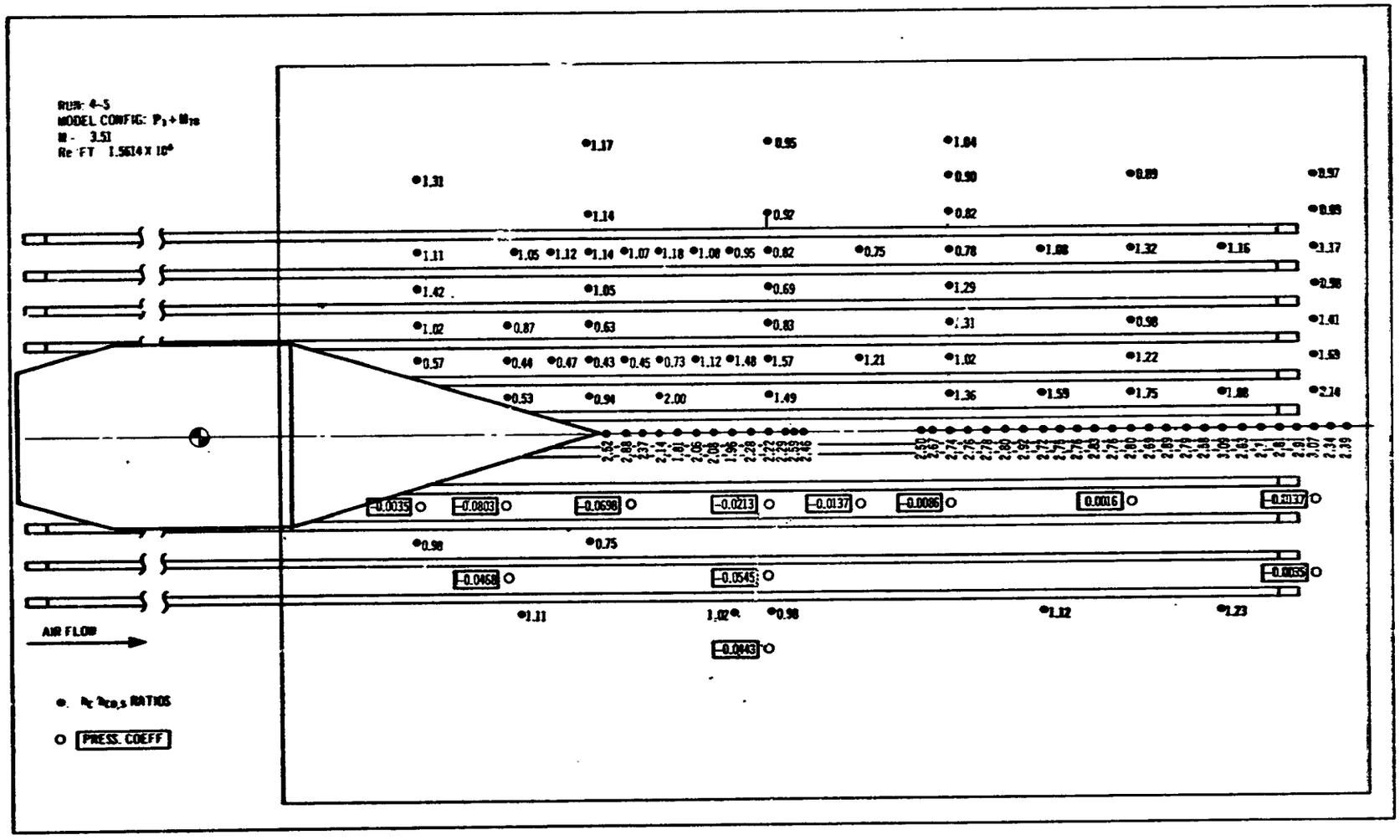

Figure 43. Langley Protuberance Heating Test-Heat Transfer Coefficient Ratios ($h_C/h_{CO,S}$) and Pressure Coefficients on Plate with Stringers

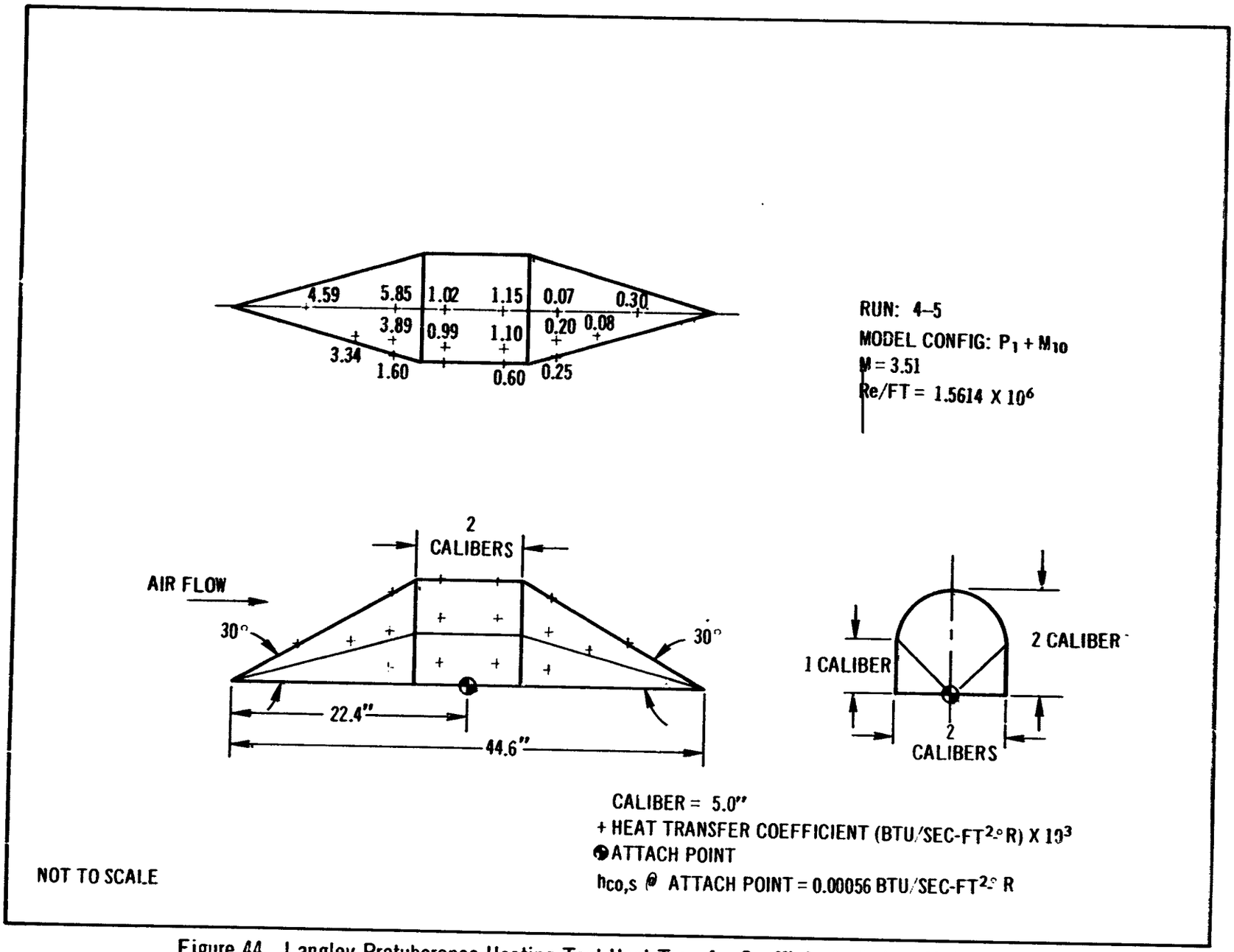

Figure 44. Langley Protuberance Heating Test-Heat Transfer Coefficients (h_C) on Model No. 10

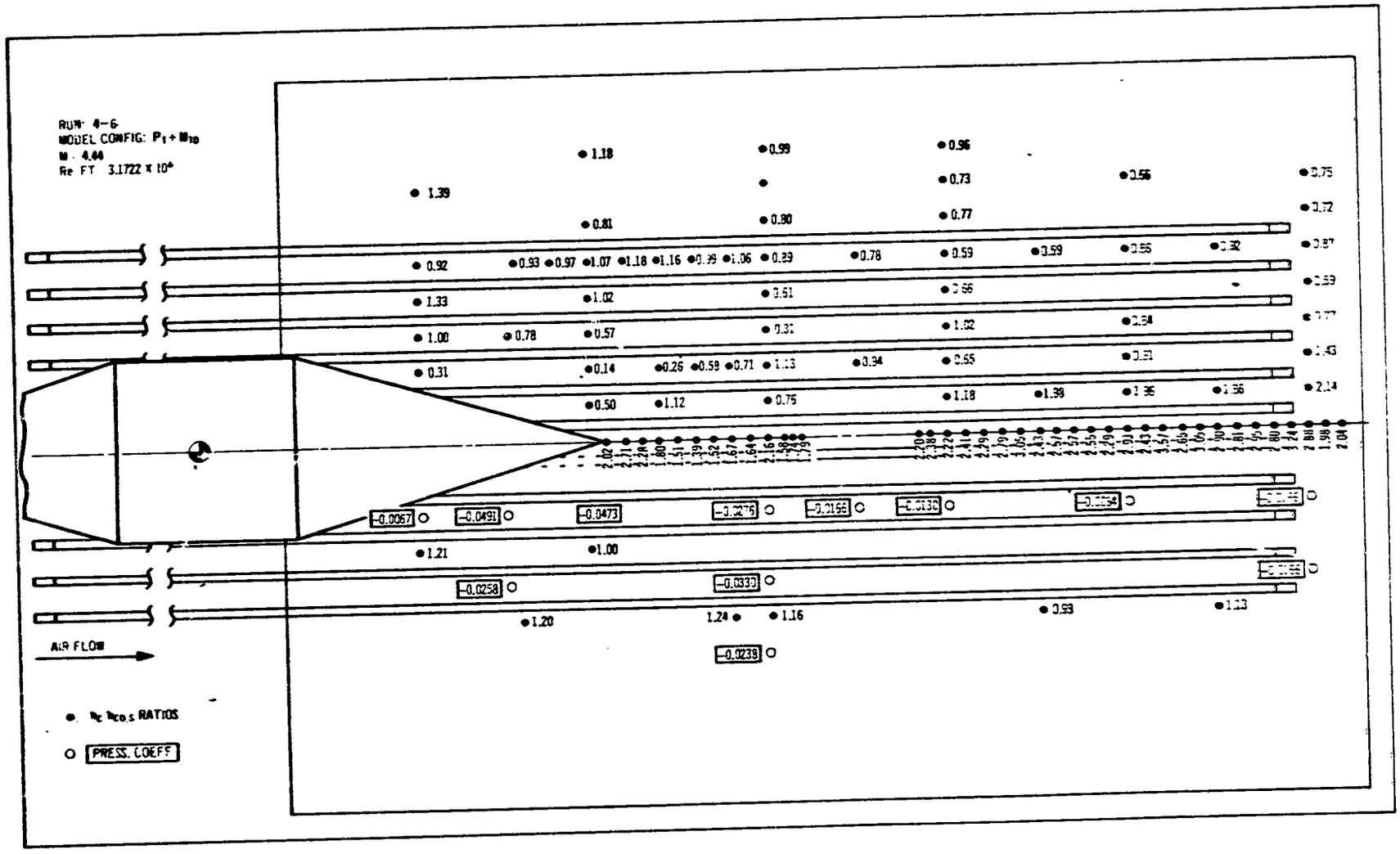

Figure 45. Langley Protuberance Heating Test-Heat Transfer Coefficient Ratios ($h_c/h_{co,s}$) and Pressure Coefficients on Plate with Stringers

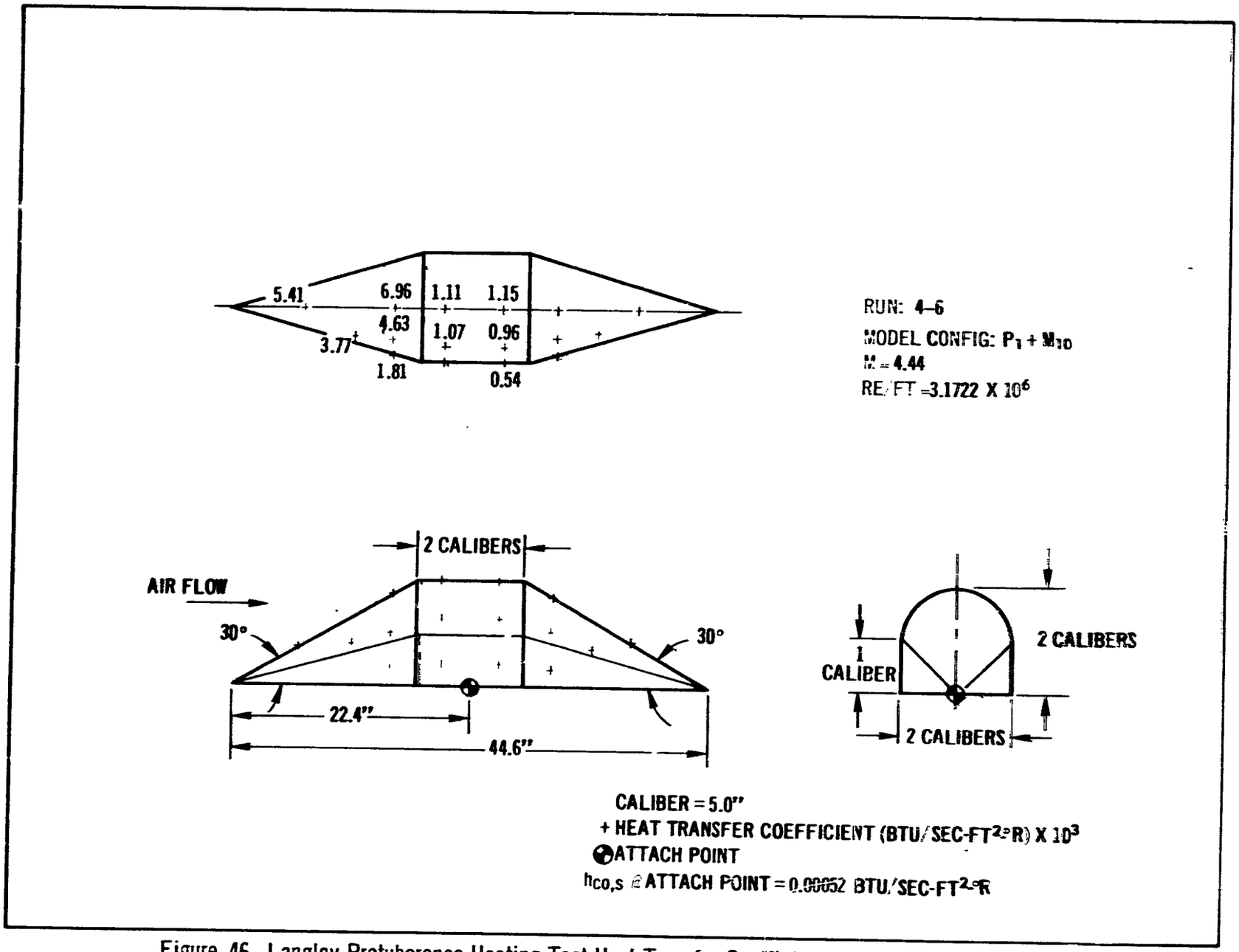

Figure 46. Langley Protuberance Heating Test-Heat Transfer Coefficients (h_C) on Model No. 10

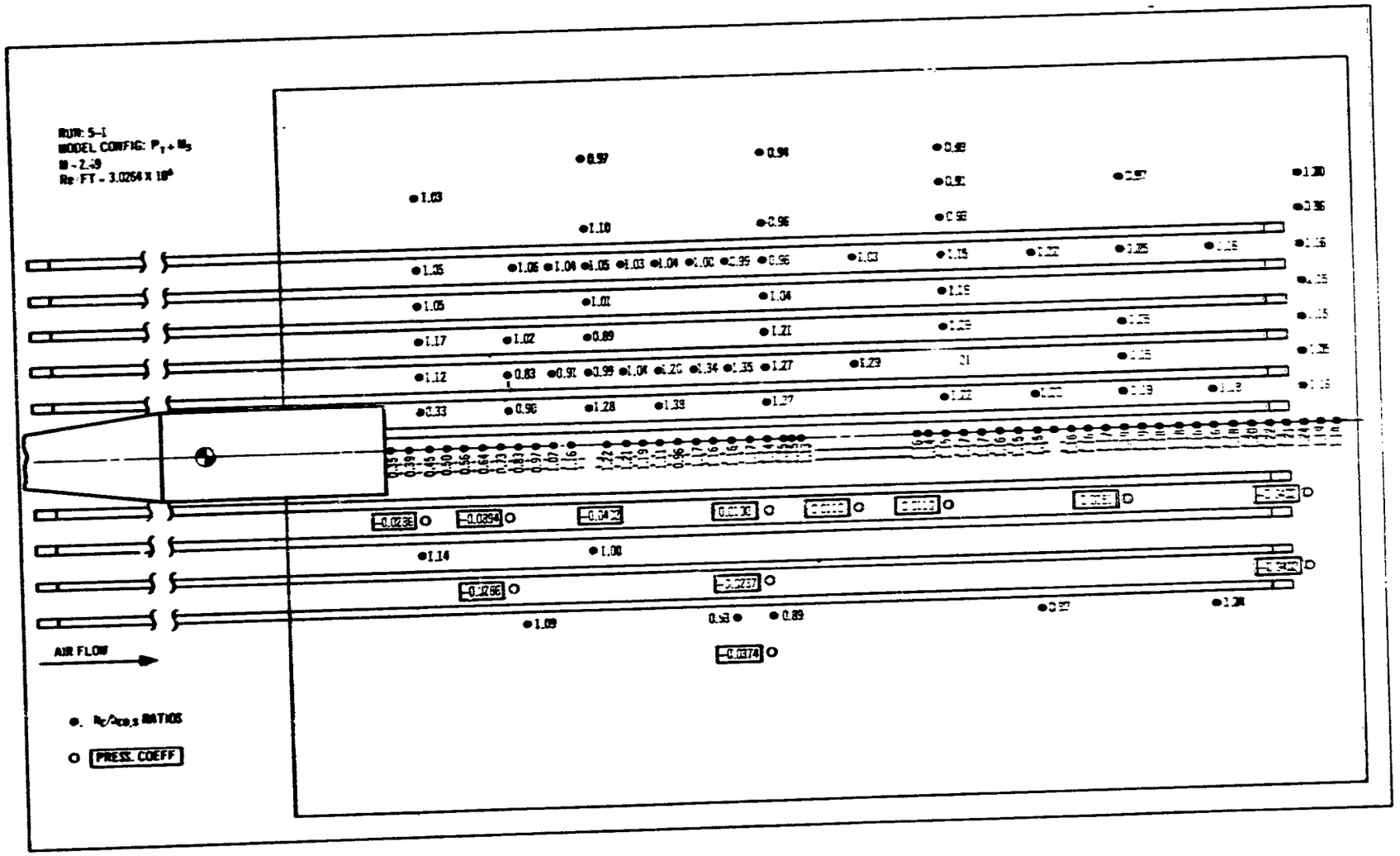

Figure 47. Langley Protuberance Heating Test-Heat Transfer Coefficient Ratios (h_c $h_{co,s}$) and Pressure Coefficients on Plate with Stringers

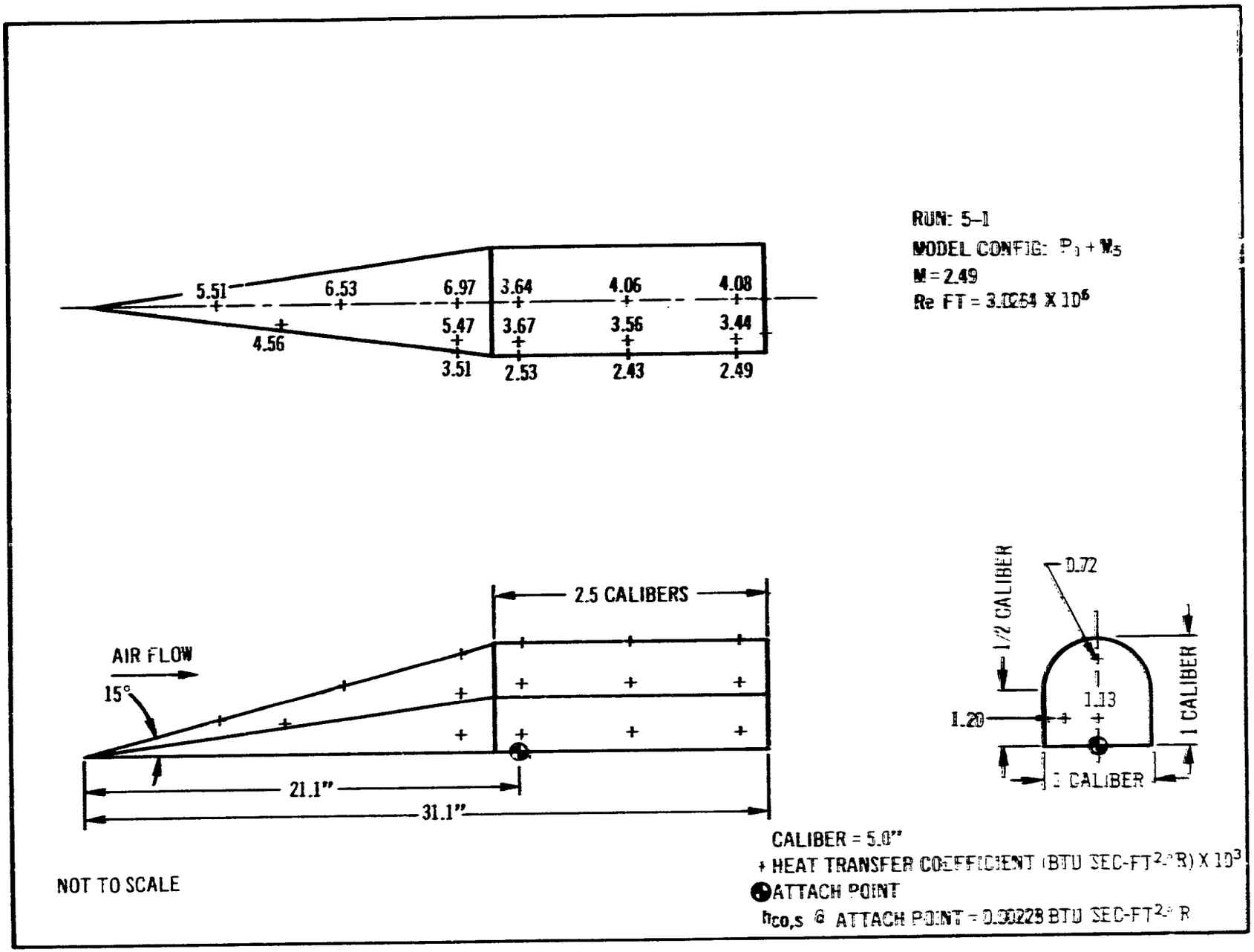

Figure 48. Langley Protuberance Heating Test-Heat Transfer Coefficients (h_c) on Model No. 5

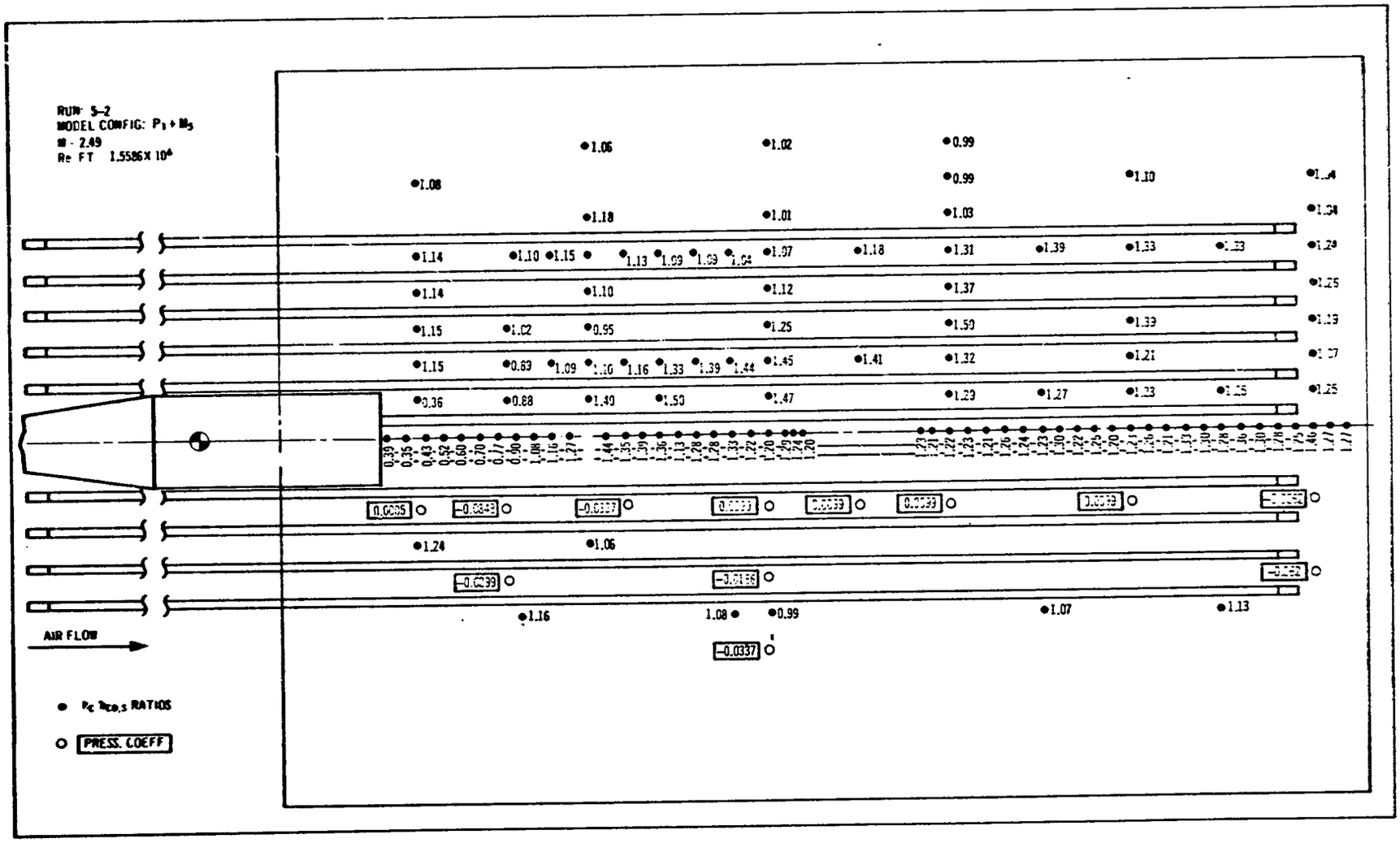

Figure 49. Langley Protuberance Heating Test-Heat Transfer Coefficient Ratios ($h_C/h_{co,s}$) and Pressure Coefficients on Plate with Stringers

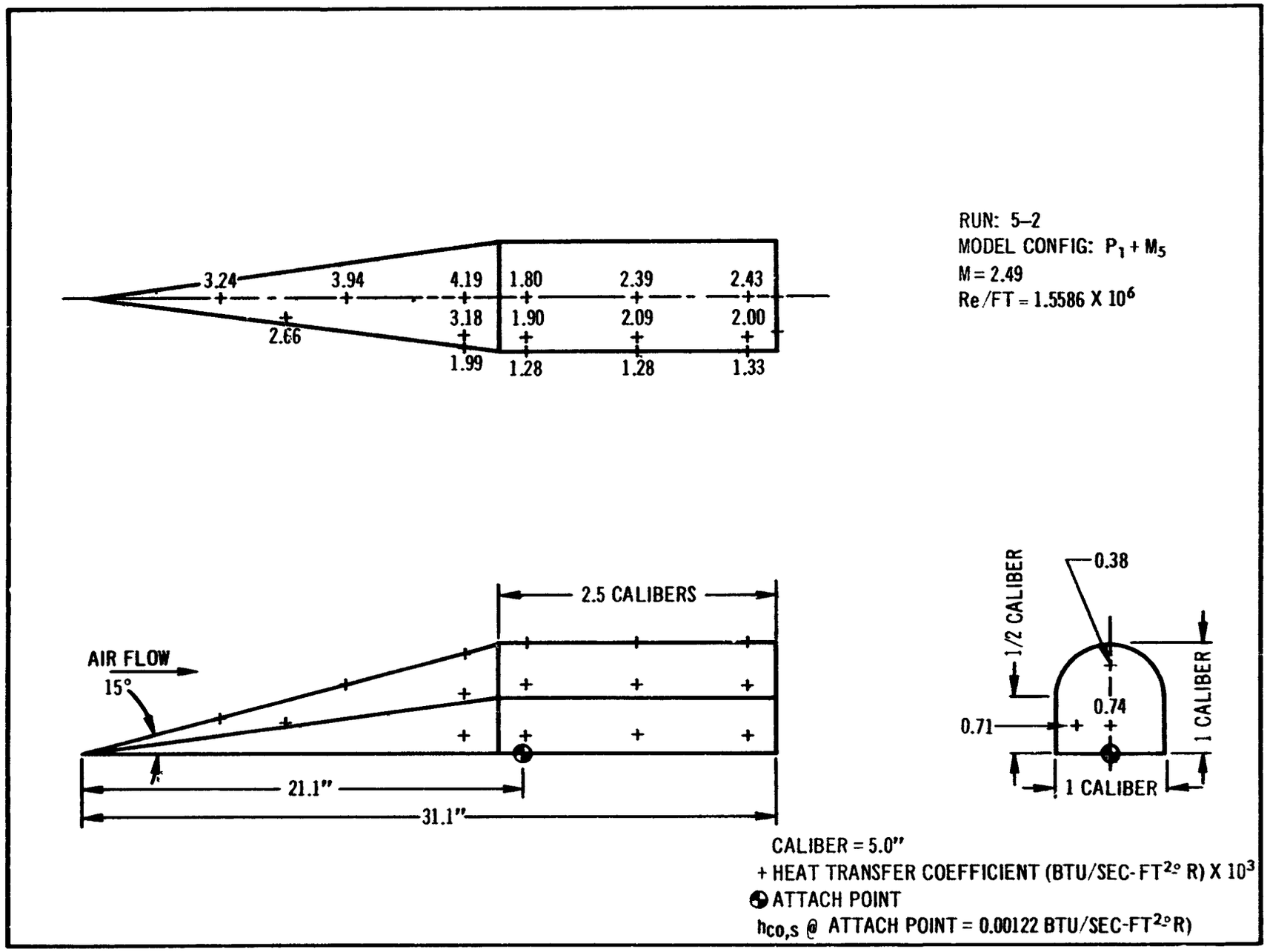

Figure 50. Langley Protuberance Heating Test-Heat Transfer Coefficients (h_C) on Model No. 10

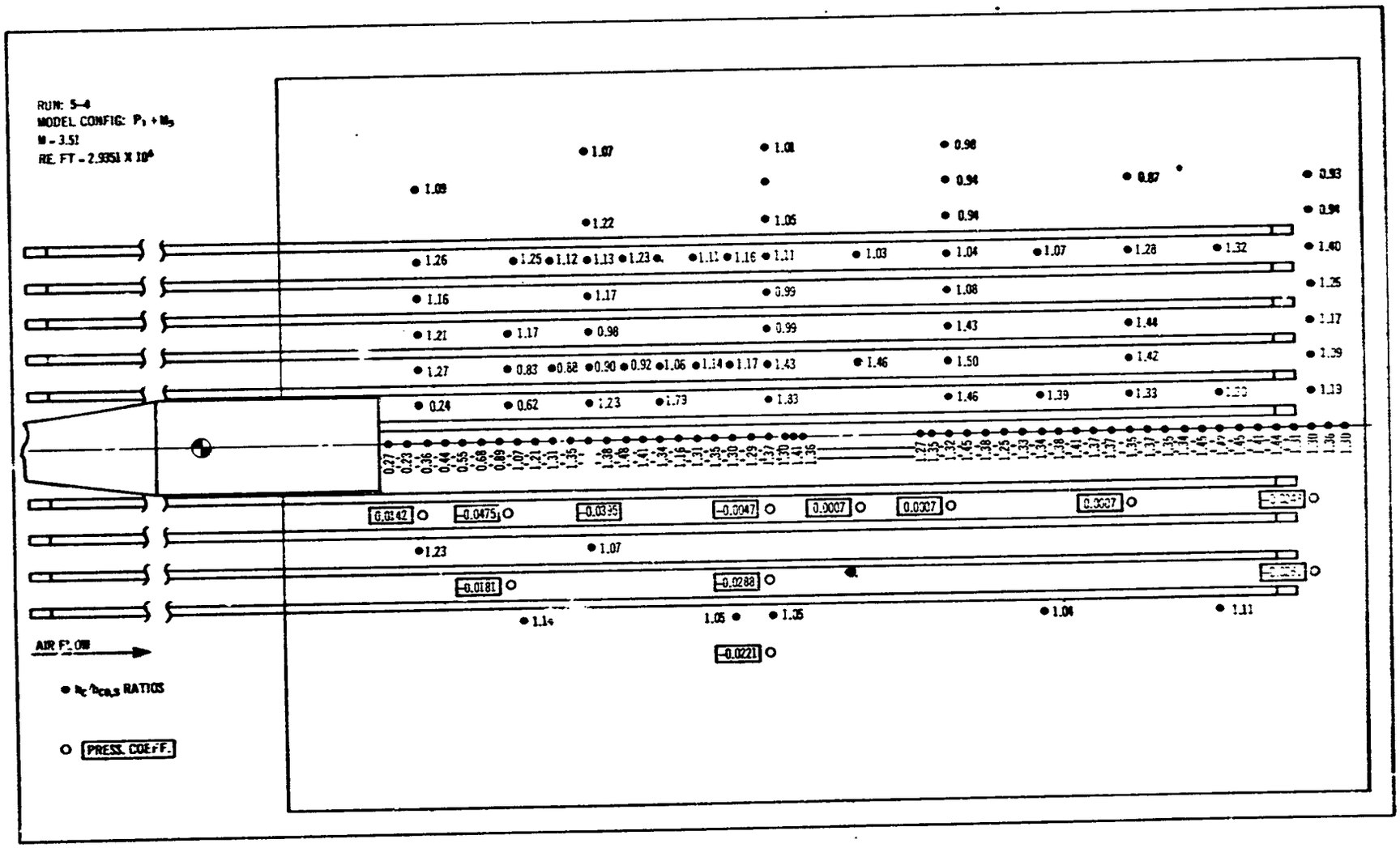

Figure 51. Langley Protuberance Heating Test-Heat Transfer Coefficient Ratios ($h_c/h_{co,s}$) and Pressure Coefficients on Plate with Stringers

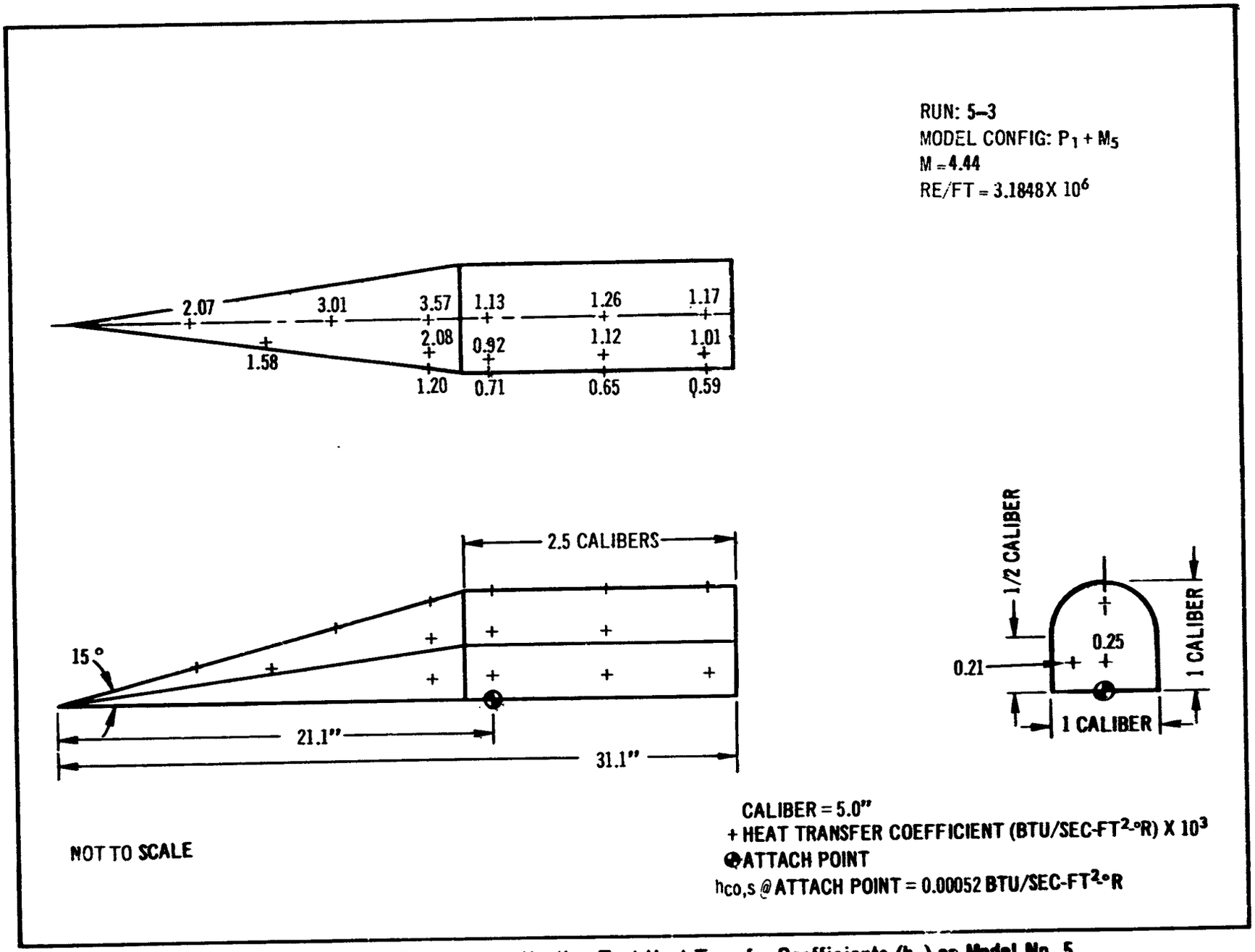

Figure 52. Langley Protuberance Heating Test-Heat Transfer Coefficients (h_c) on Model No. 5

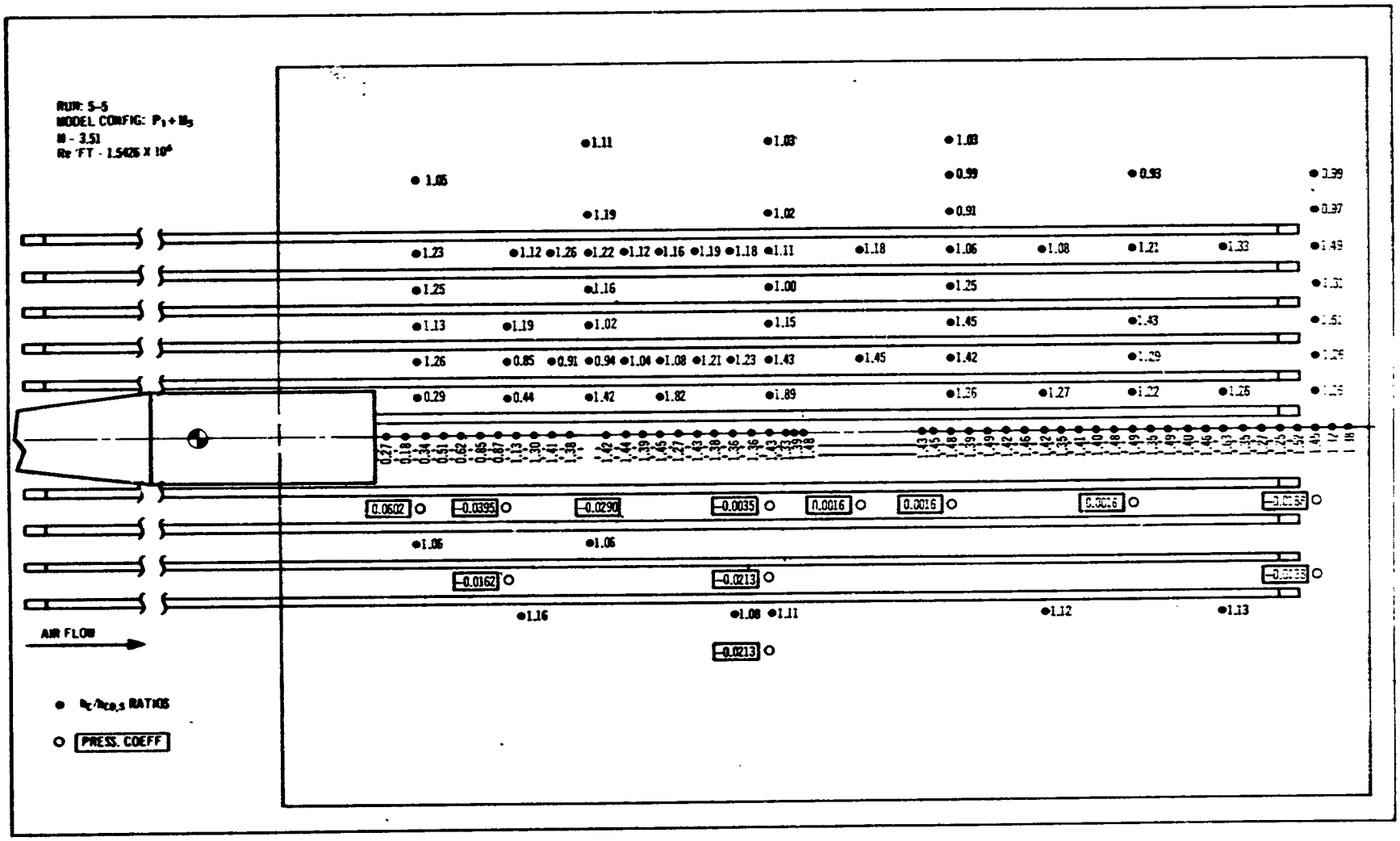

Figure 53. Langley Protuberance Heating Test-Heat Transfer Coefficient Ratios ($h_c/h_{co,s}$) and Pressure Coefficients on Plate with Stringers

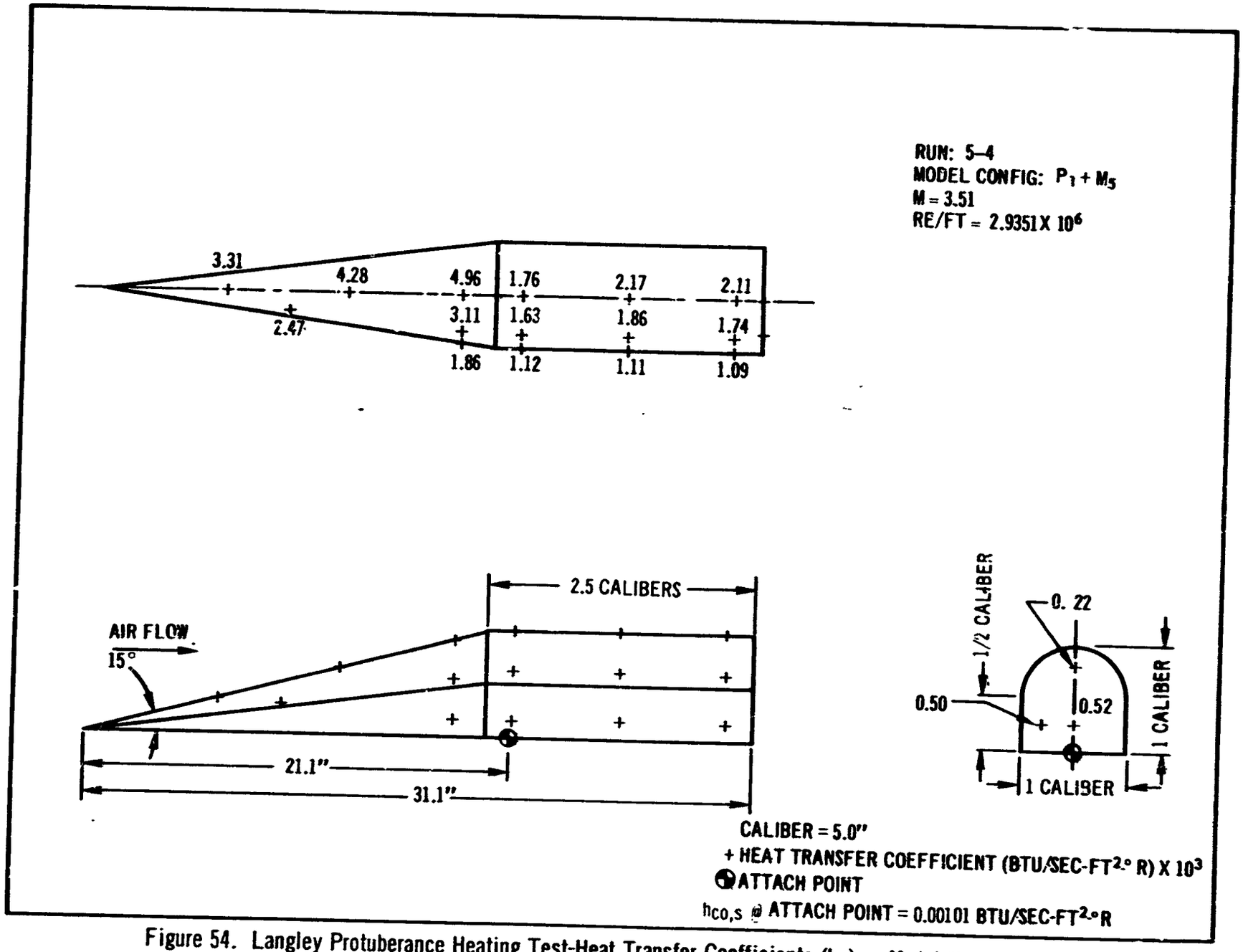

Figure 54. Langley Protuberance Heating Test-Heat Transfer Coefficients (h_c) on Model No. 5

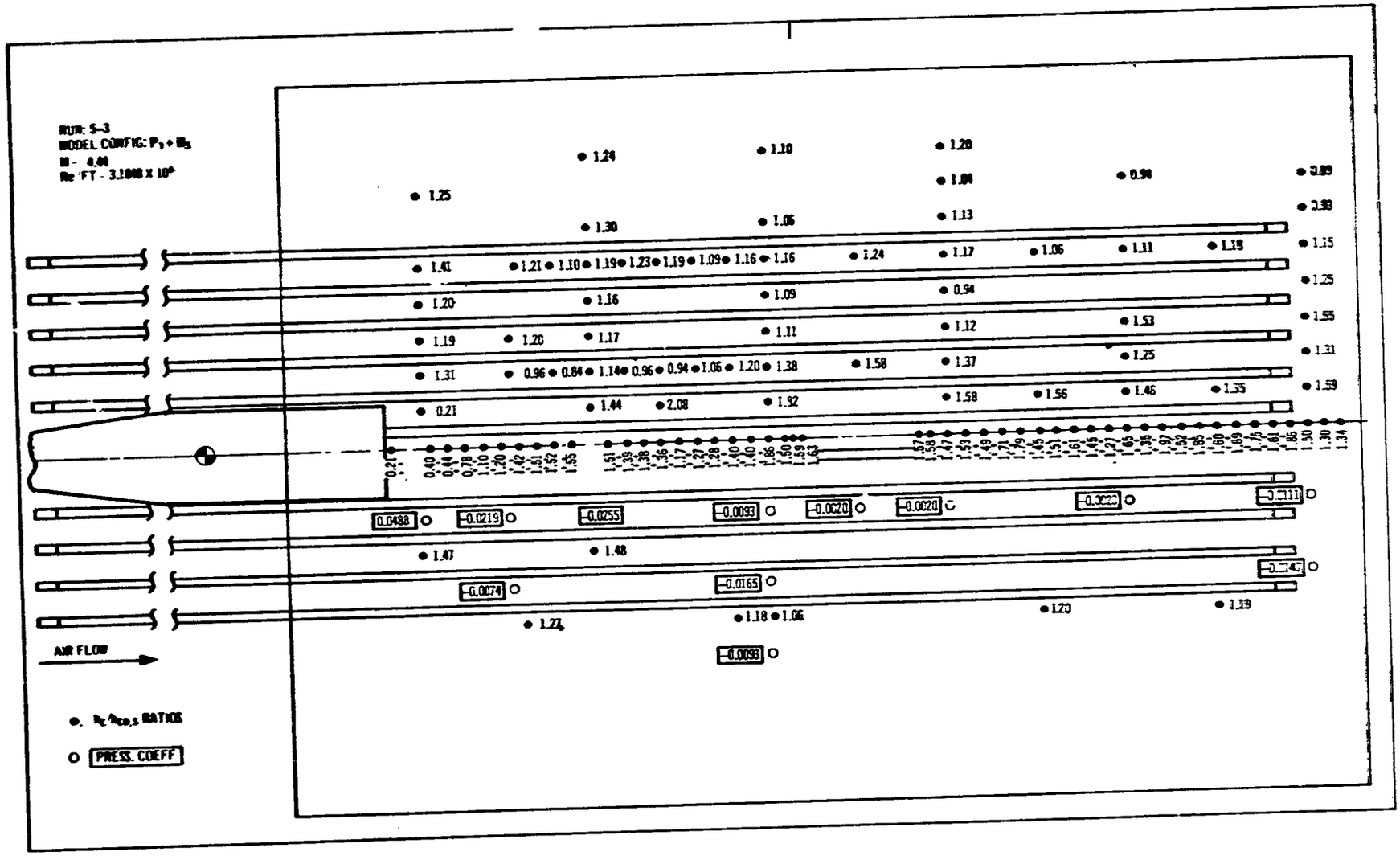

Figure 55. Langley Protuberance Heating Test-Heat Transfer Coefficient Ratios ($h_C/h_{co,s}$) and Pressure Coefficients on Plate with Stringers

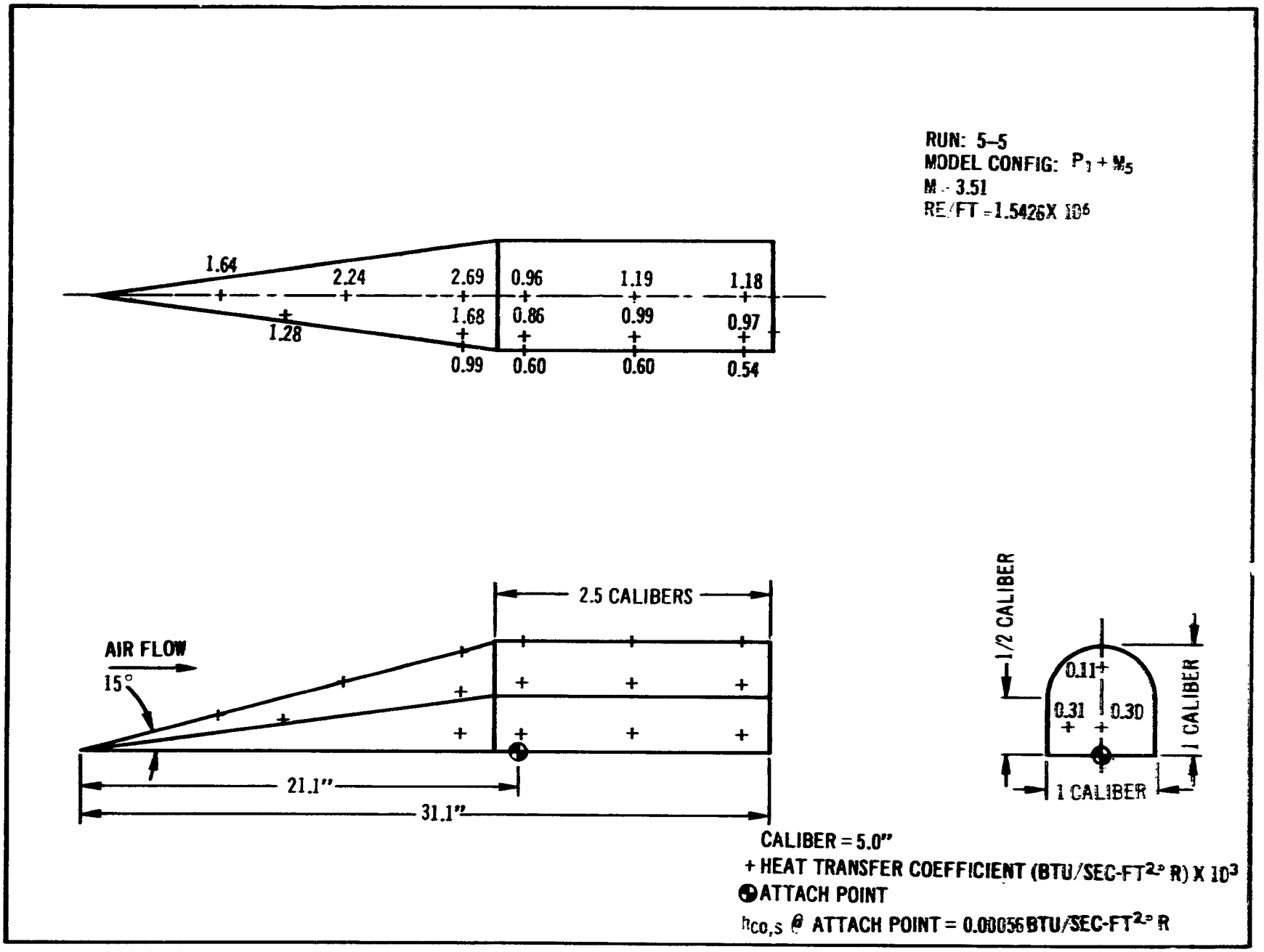

Figure 56. Langley Protuberance Heating Test-Heat Transfer Coefficients (h_C) on Model No. 5

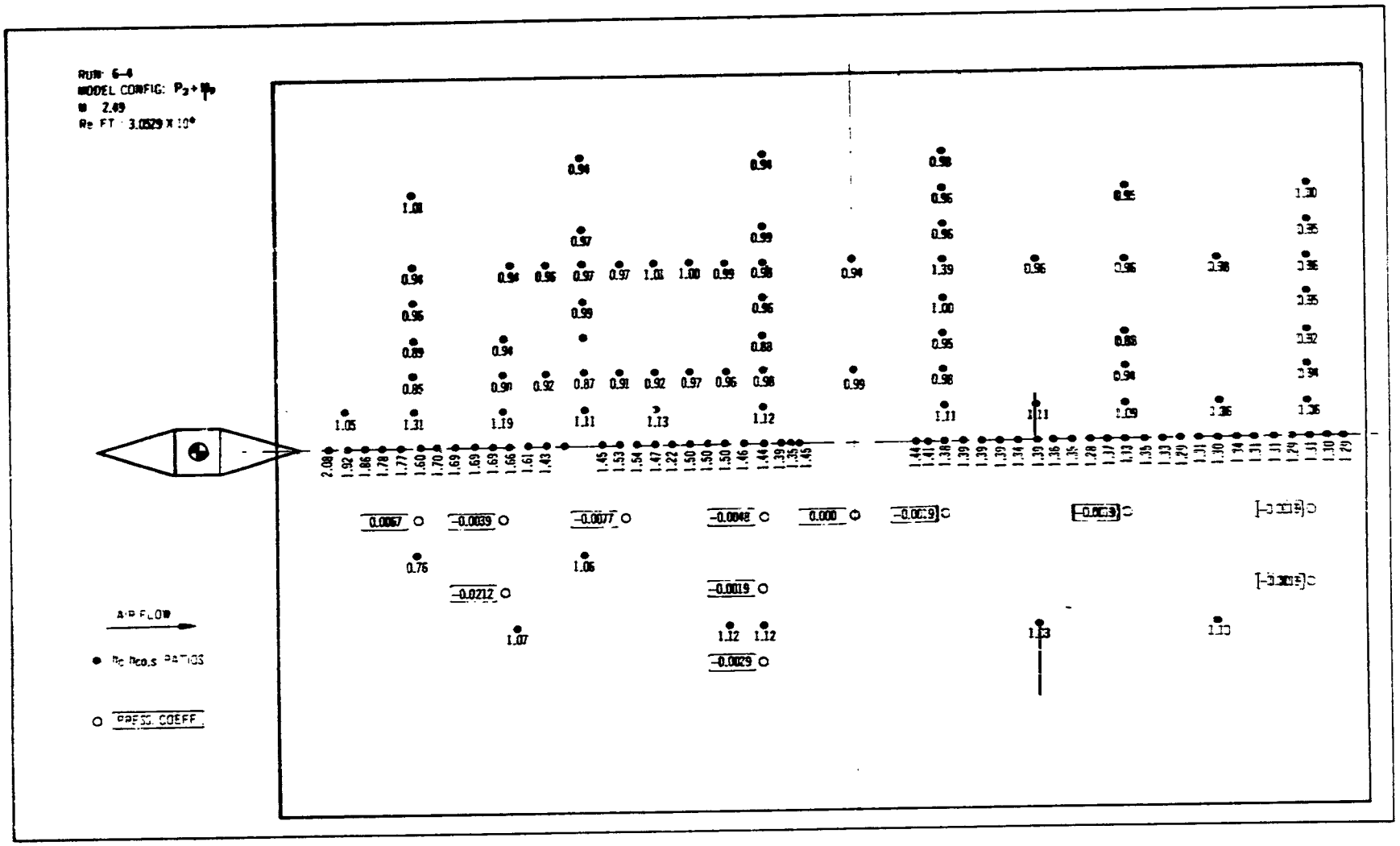

Figure 57. Langley Protuberance Heating Test-Heat Transfer Coefficient Ratios ($h_c / h_{c,D,s}$) and Pressure Coefficients on Smooth Plate

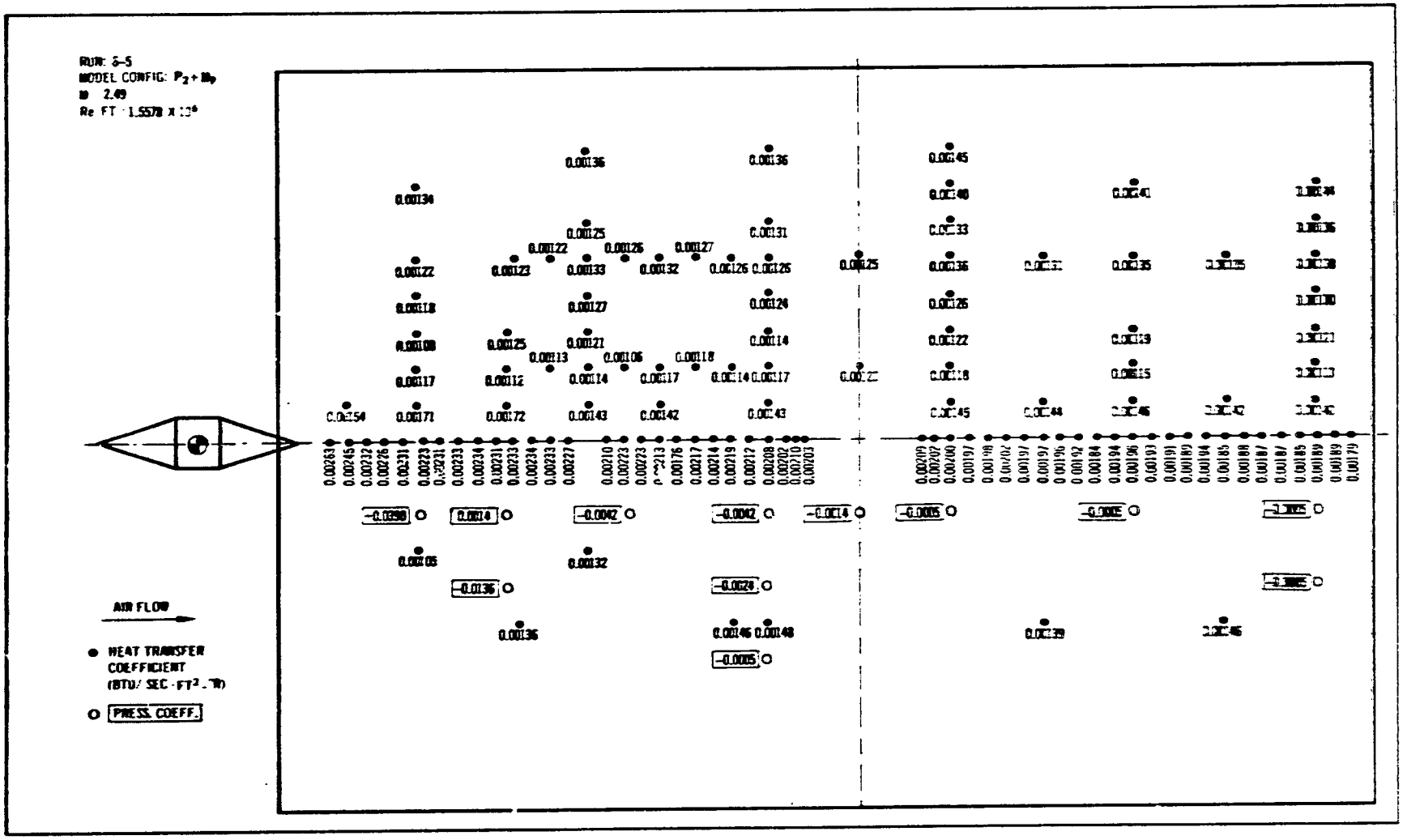

Figure 58. Langley Protuberance Heating Test-Heat Transfer Coefficients (h_c) and Pressure Coefficients on Smooth Plate

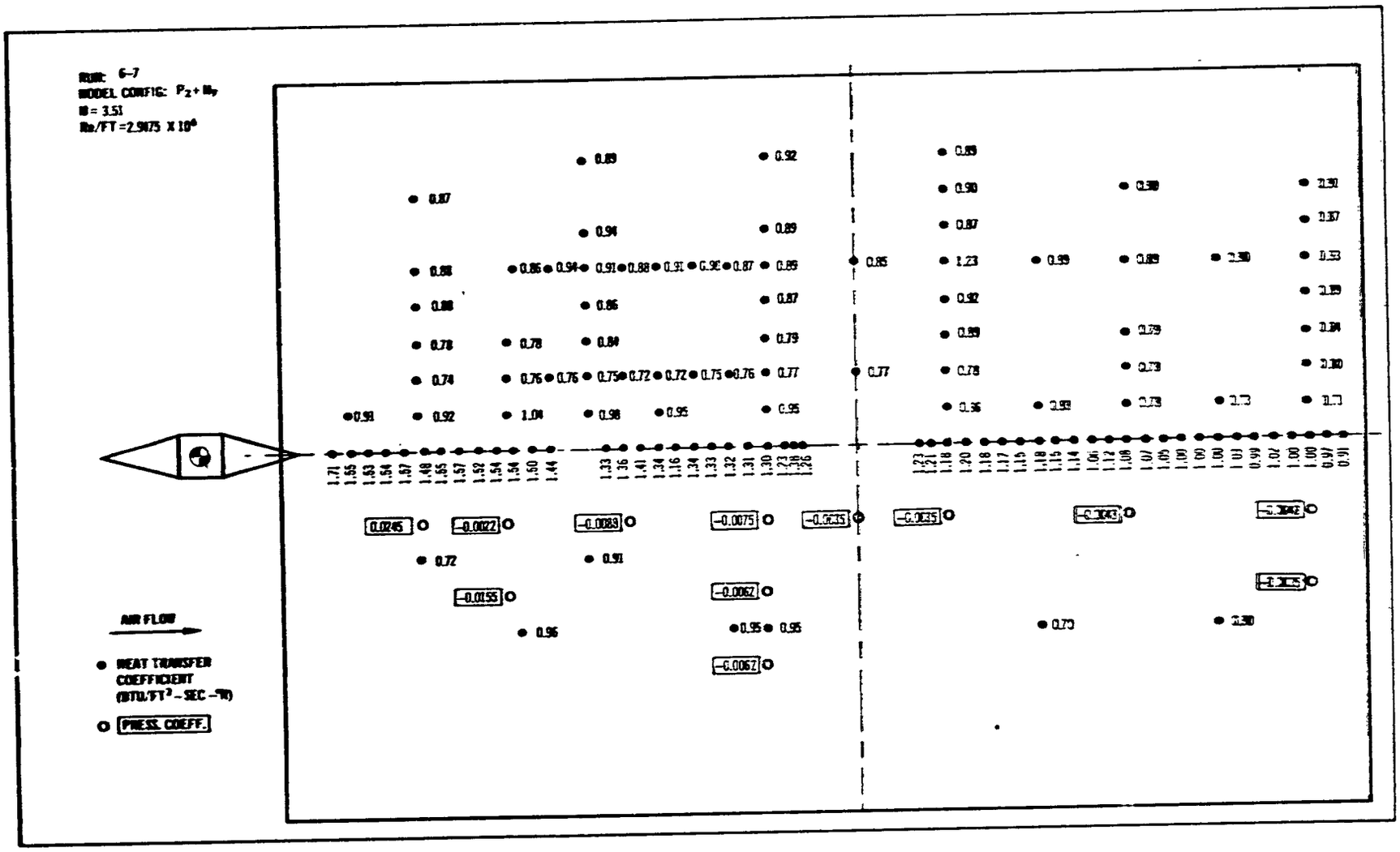

Figure 59. Langley Protuberance Heating Test-Heat Transfer Coefficient Ratios ($h_c/h_{co,s}$) and Pressure Coefficients on Smooth Plate

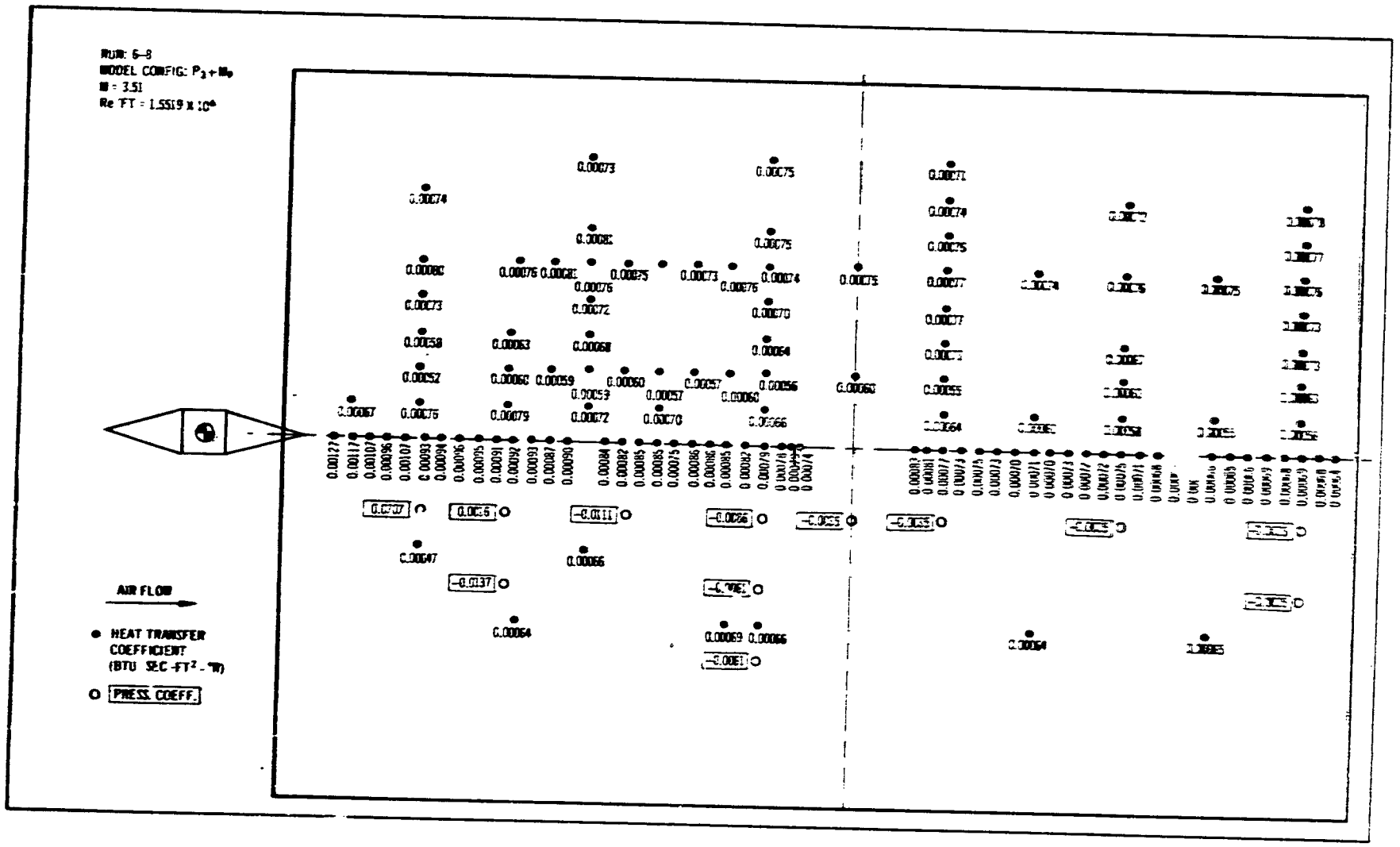

Figure 60. Langley Protuberance Heating Test-Heat Transfer Coefficients (h_c) and Pressure Coefficients on Smooth Plate

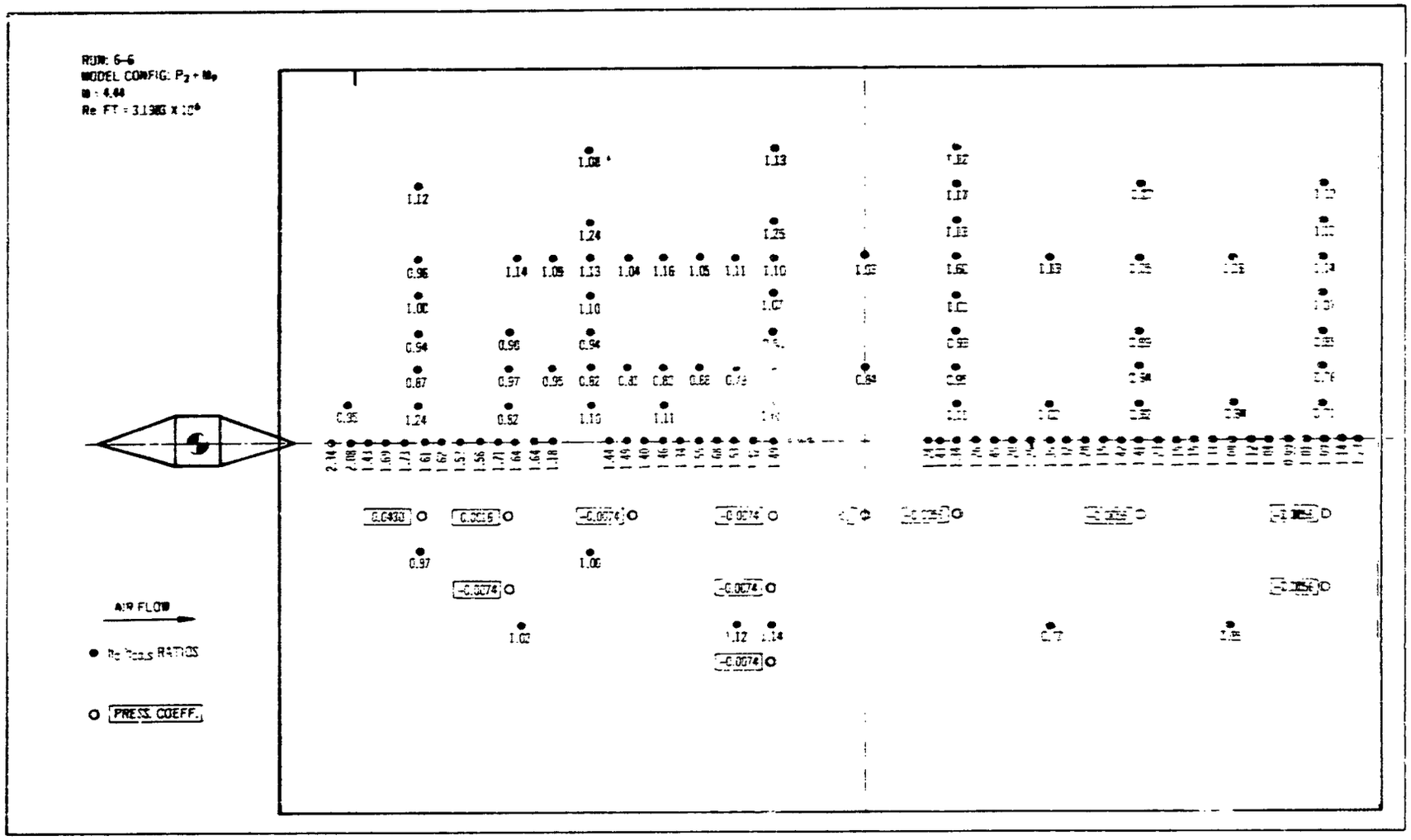

Figure 61. Langley Protuberance Heating Test-Heat Transfer Coefficient Ratios (h_C $h_{CD,s}$) and Pressure Coefficients on Smooth Plate

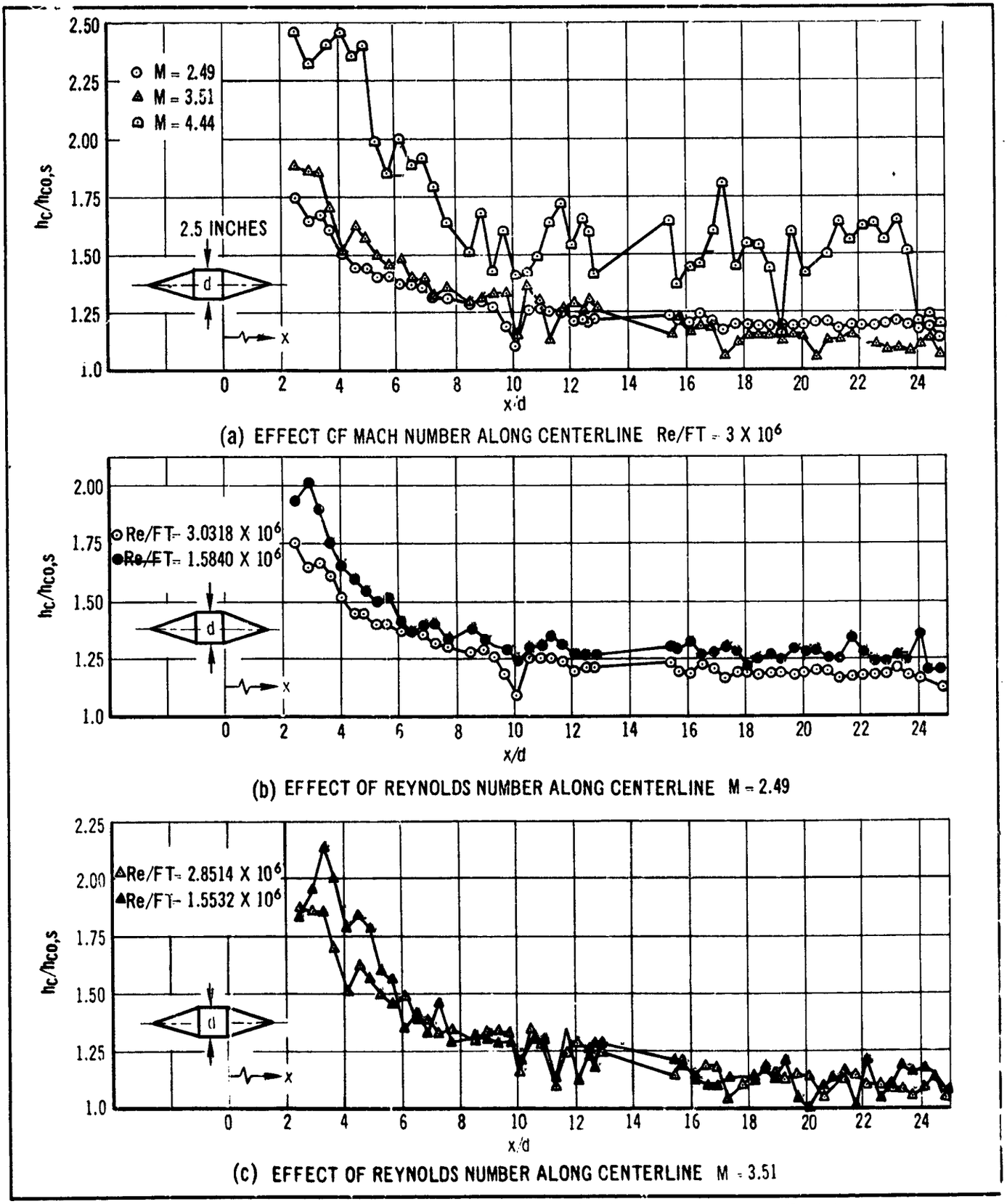

Figure 62. Downstream Heat Transfer Coefficient Ratios $h_c/h_{co,s}$ Along the Protuberance Centerline of Model No. 9

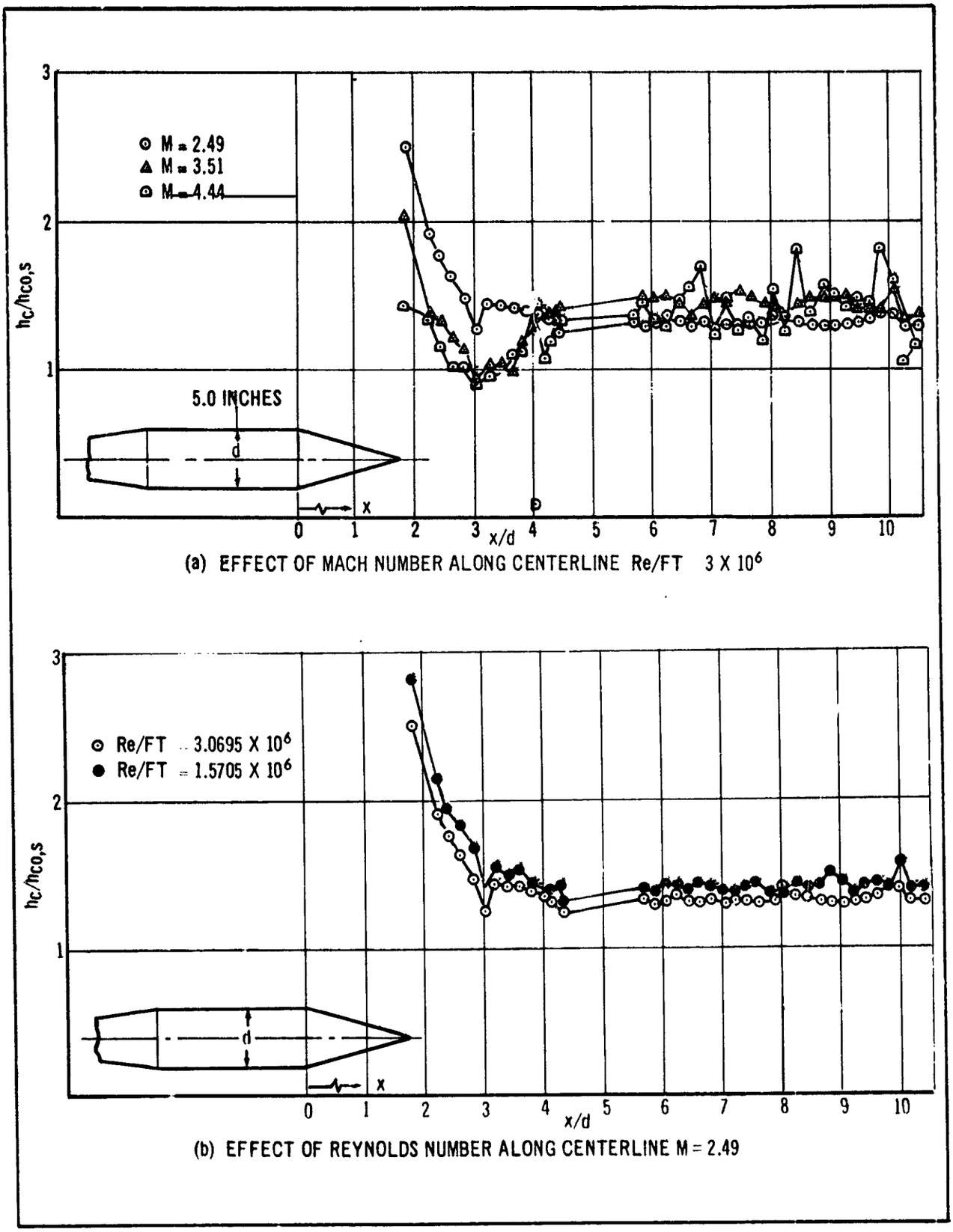

(a) EFFECT OF MACH NUMBER ALONG CENTERLINE Re/FT 3×10^6

(b) EFFECT OF REYNOLDS NUMBER ALONG CENTERLINE M = 2.49

Figure 63. Downstream Heat Transfer Coefficient Ratios $h_c/h_{co,s}$ Along the Protuberance Centerline of Model No. 2

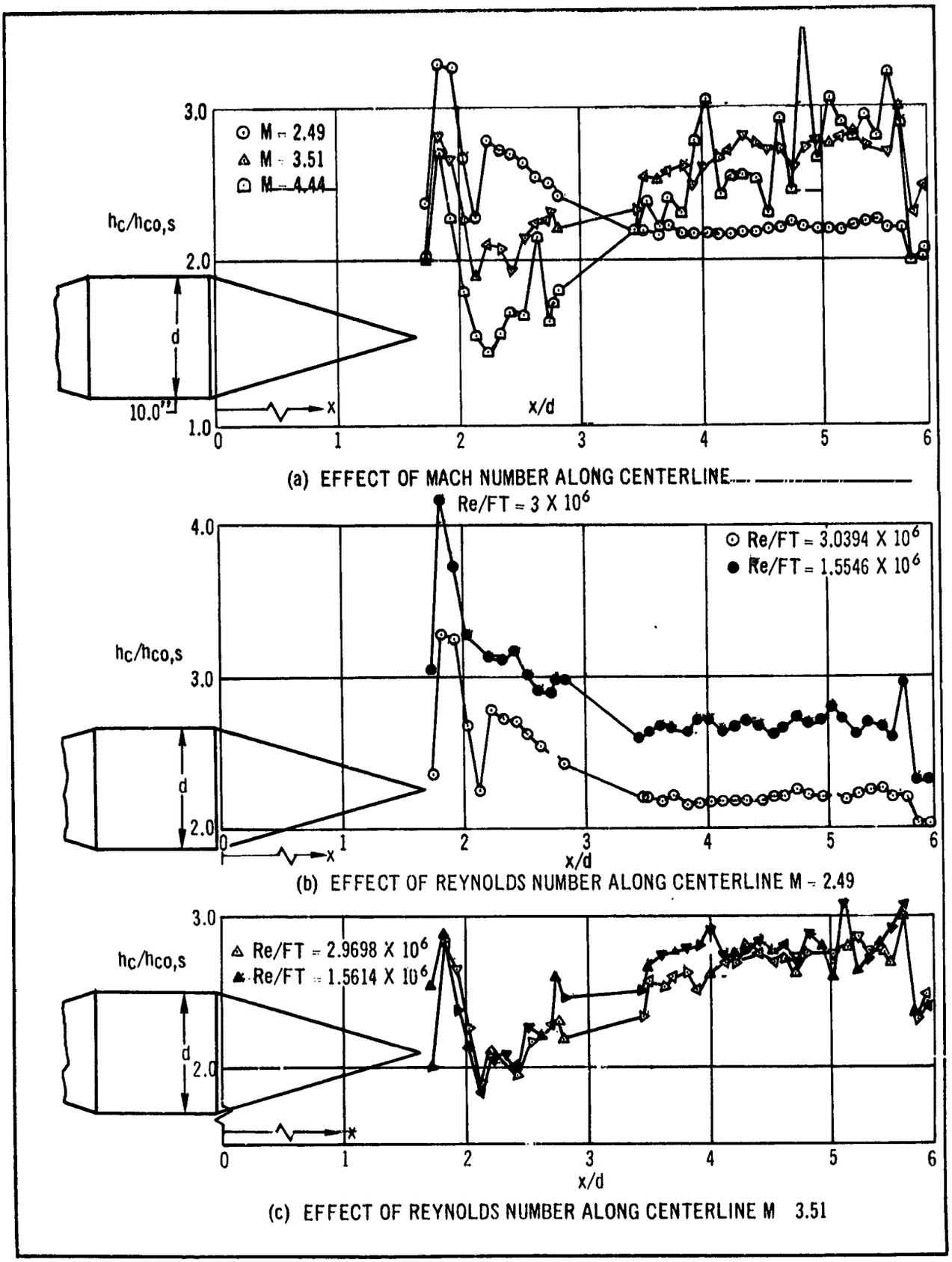

Figure 64. Downstream Heat Transfer Coefficient Ratios $h_c/h_{co,s}$ Along the Protuberance Centerline of Model No. 10

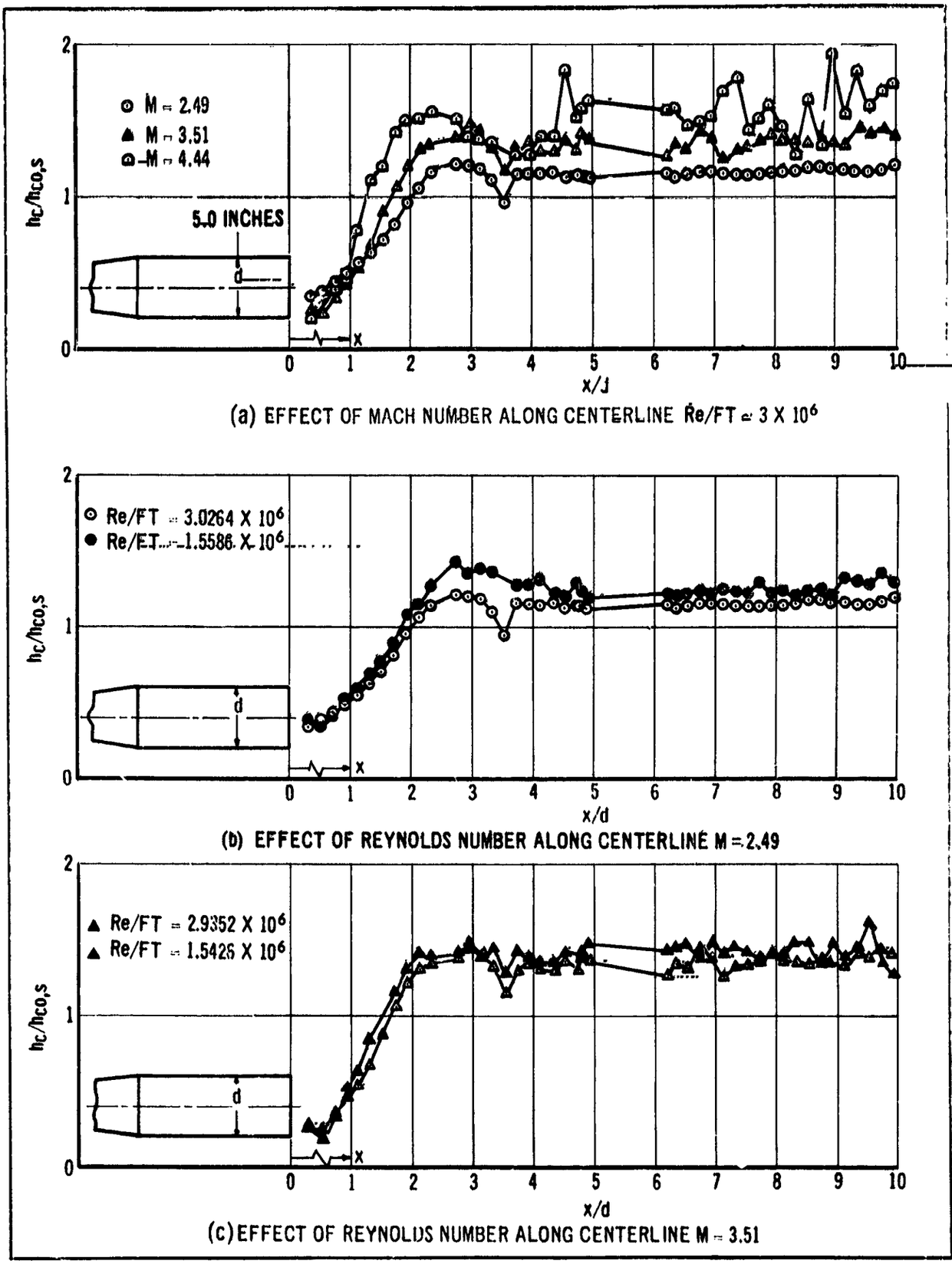

(a) EFFECT OF MACH NUMBER ALONG CENTERLINE Re/FT = 3 X 10^6

(b) EFFECT OF REYNOLDS NUMBER ALONG CENTERLINE M = 2.49

(c) EFFECT OF REYNOLDS NUMBER ALONG CENTERLINE M = 3.51

Figure 65. Downstream Heat Transfer Coefficient Ratios $h_c/h_{co,s}$ Along the Protuberance Centerline of Model No. 5

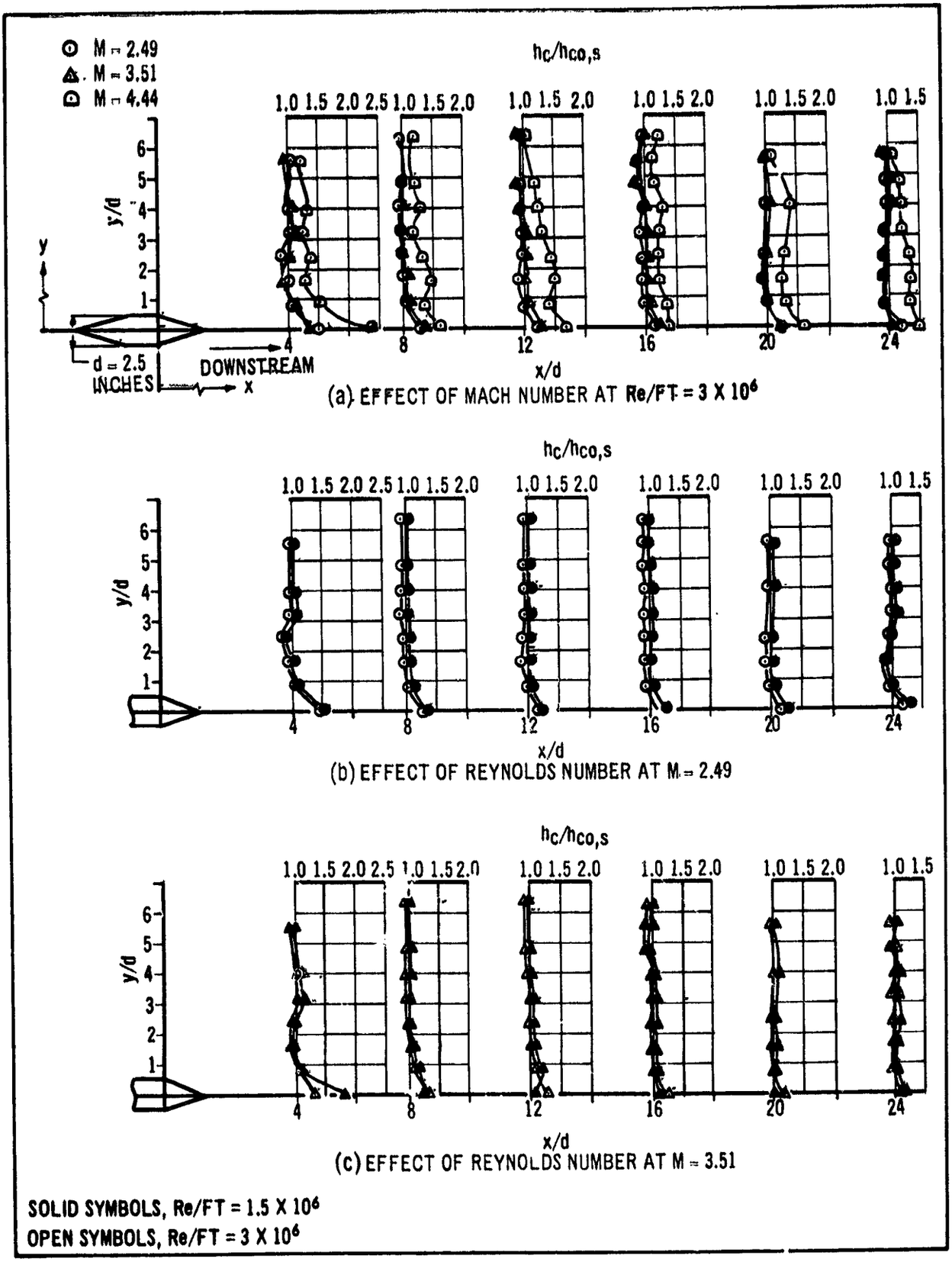

Figure 66. Lateral Heat Transfer Coefficient Ratios $h_c/h_{co,s}$ in the Turbulent Wake Region of Model No. 9

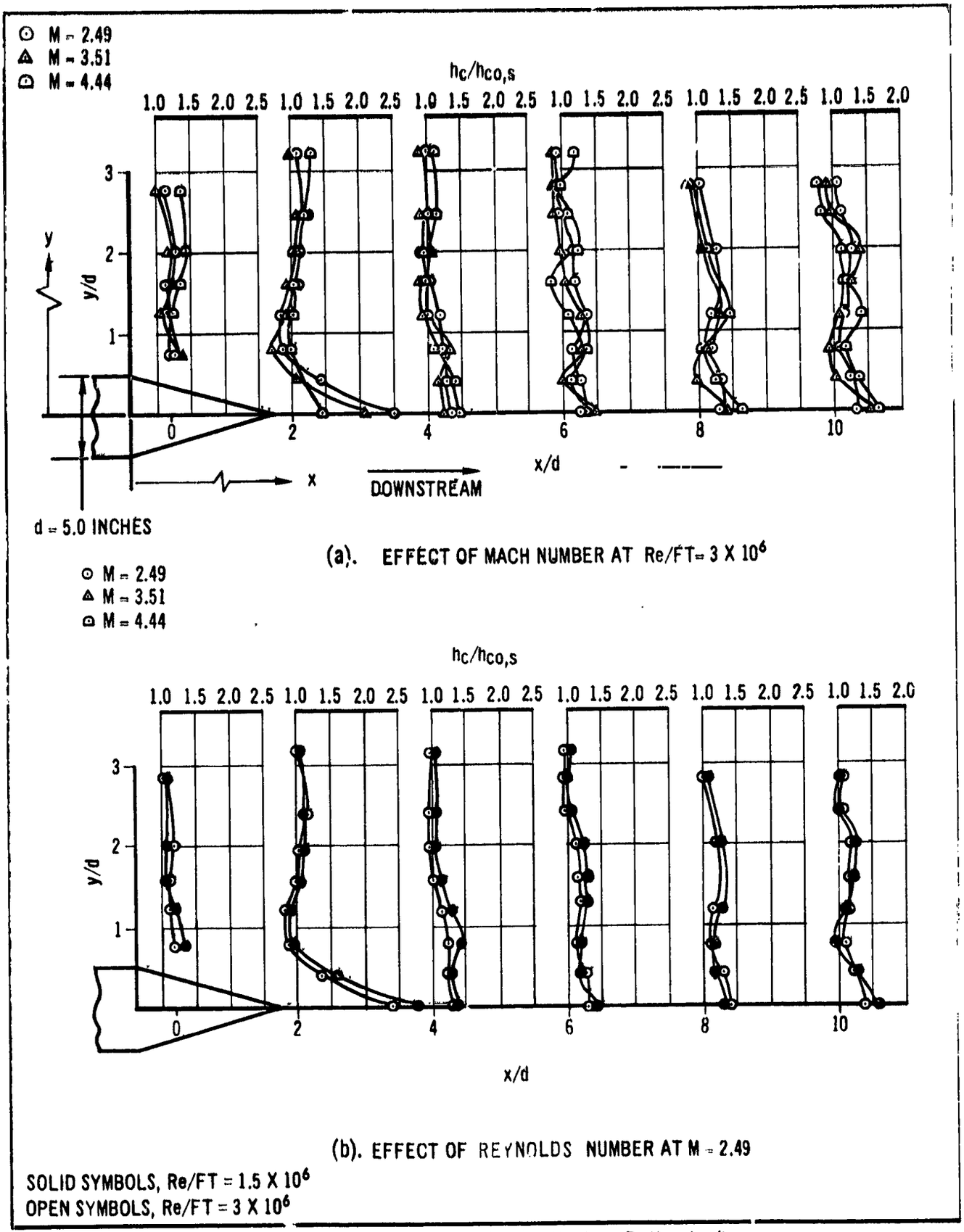

Figure 67 Lateral Heat Transfer Coefficient Ratios $h_c/h_{co,s}$ in the Turbulent Wake Region of Model No. 2

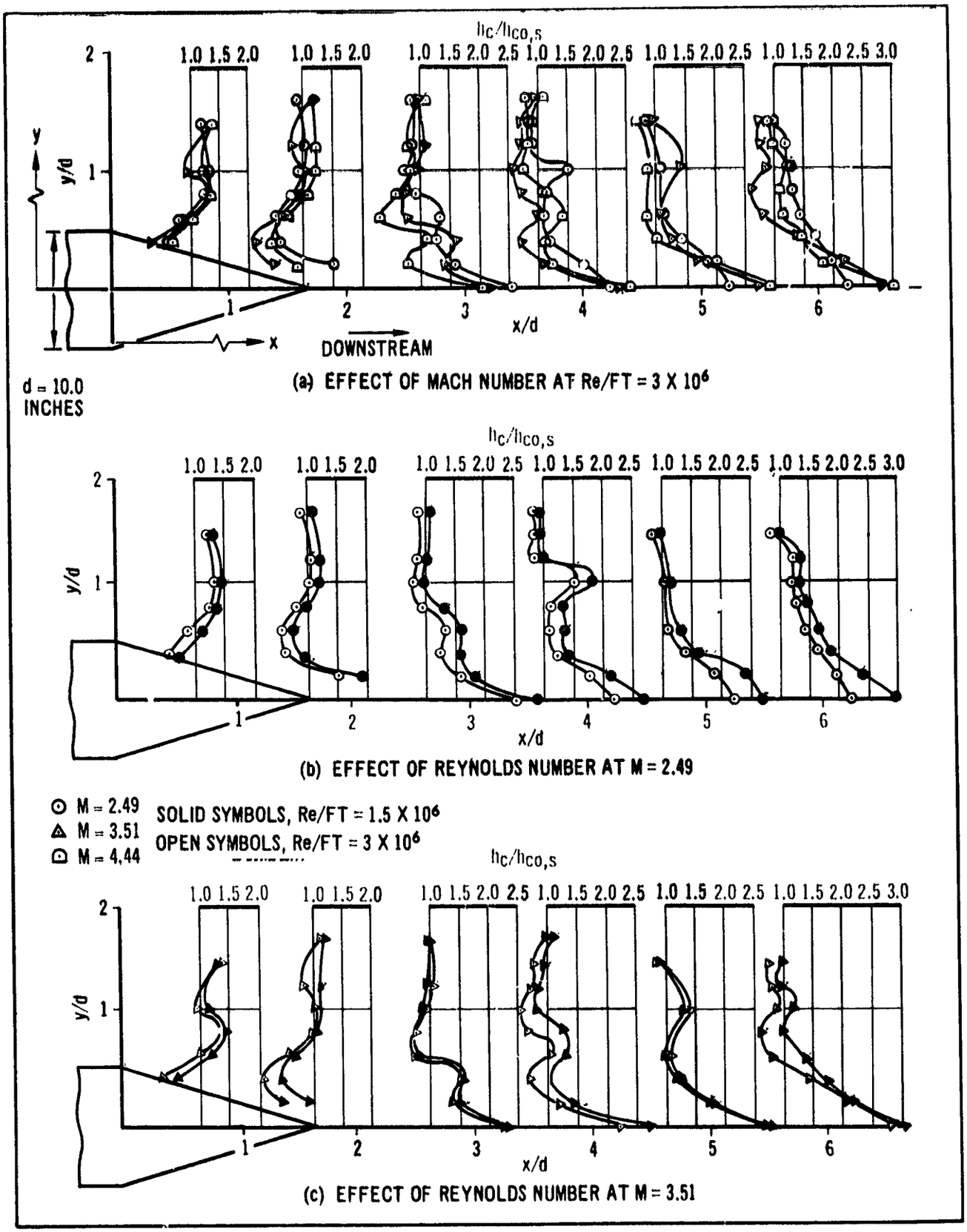

Figure 68. Lateral Heat Transfer Coefficient Ratios $h_c/h_{co,s}$ in the Turbulent Wake Region of Model No. 10

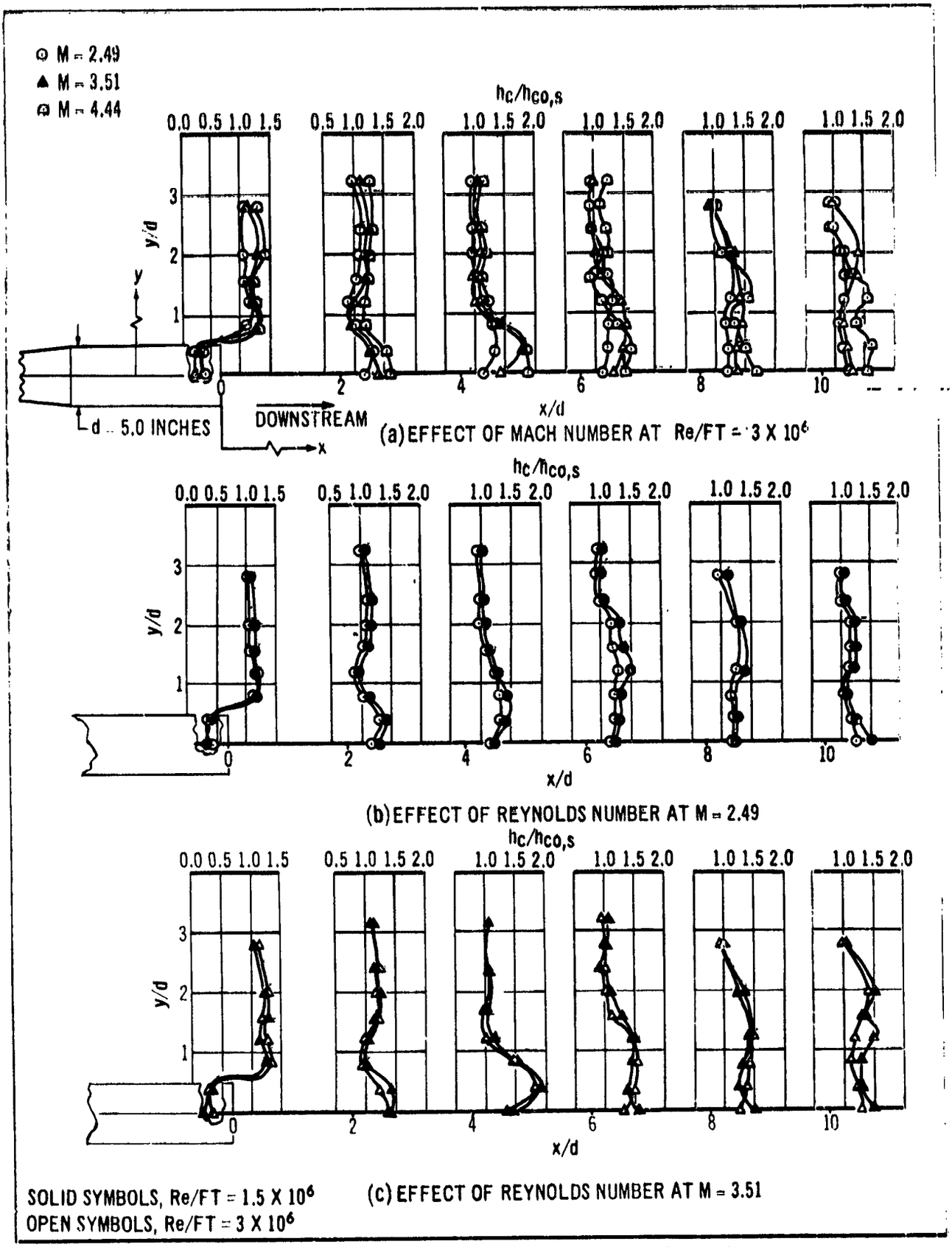

Figure 69. Lateral Heat Transfer Coefficient Ratios $h_c/h_{co,s}$ in the Turbulent Wake Region of Model No. 5

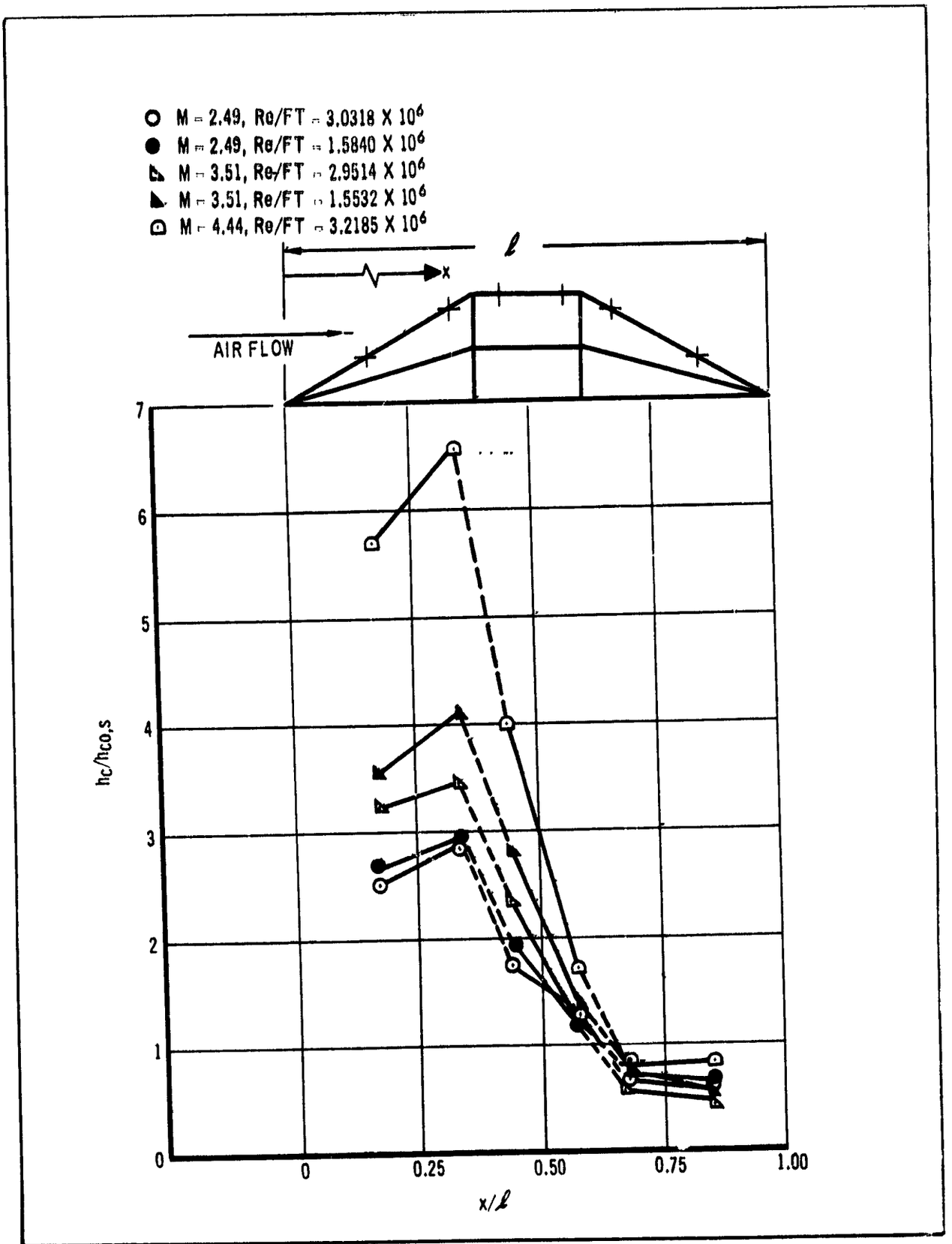

Figure 70(a). Axial Distribution of the Ratio of Model Heat Transfer Coefficient To Flat Plate Heat Transfer Coefficient on Model No. 9

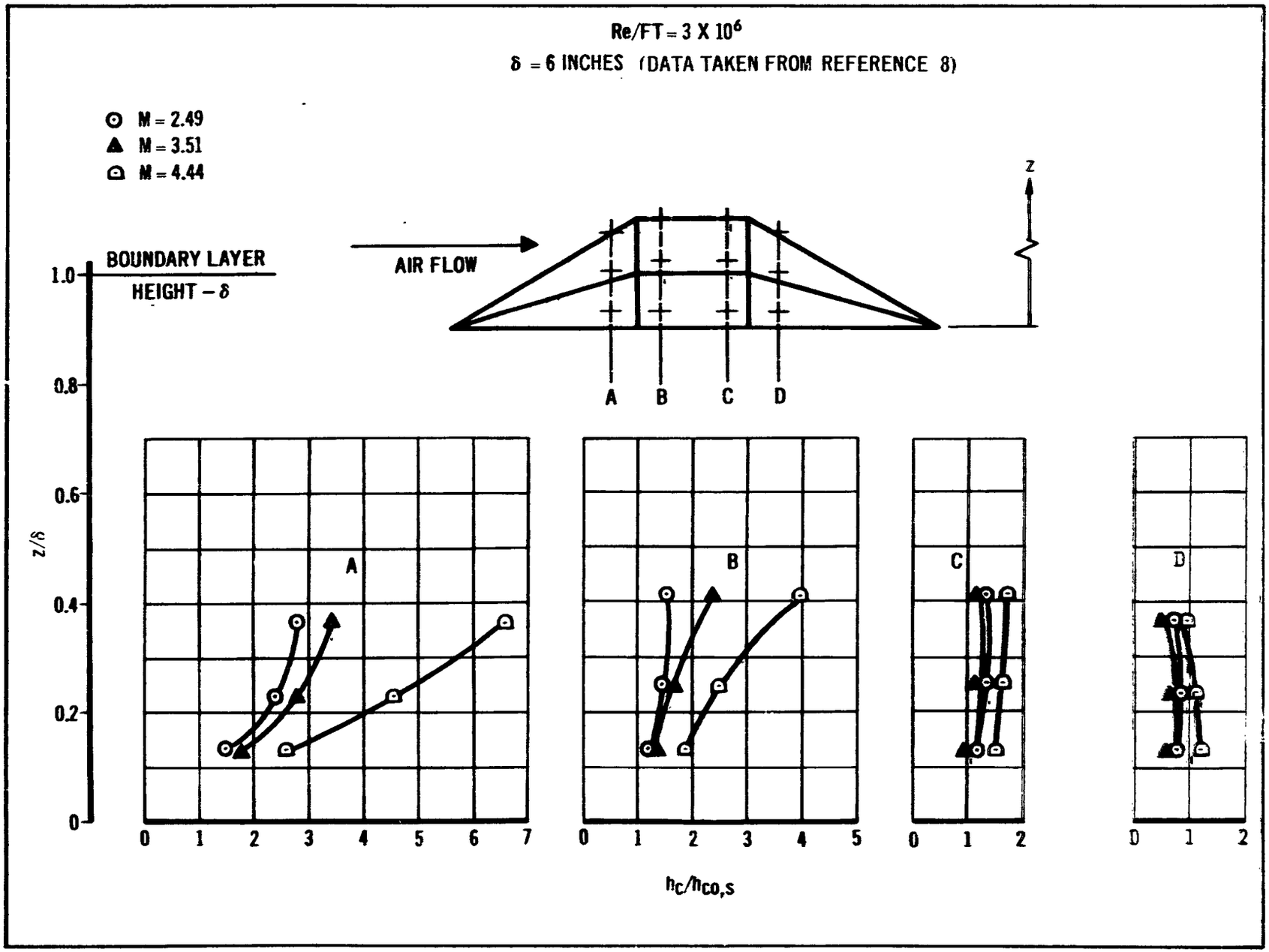

Figure 70(b).. Cross Sectional Distribution of the Ratio of Model Heat Transfer Coefficient To Flat Plate Heat Transfer Coefficient on Model No. 9

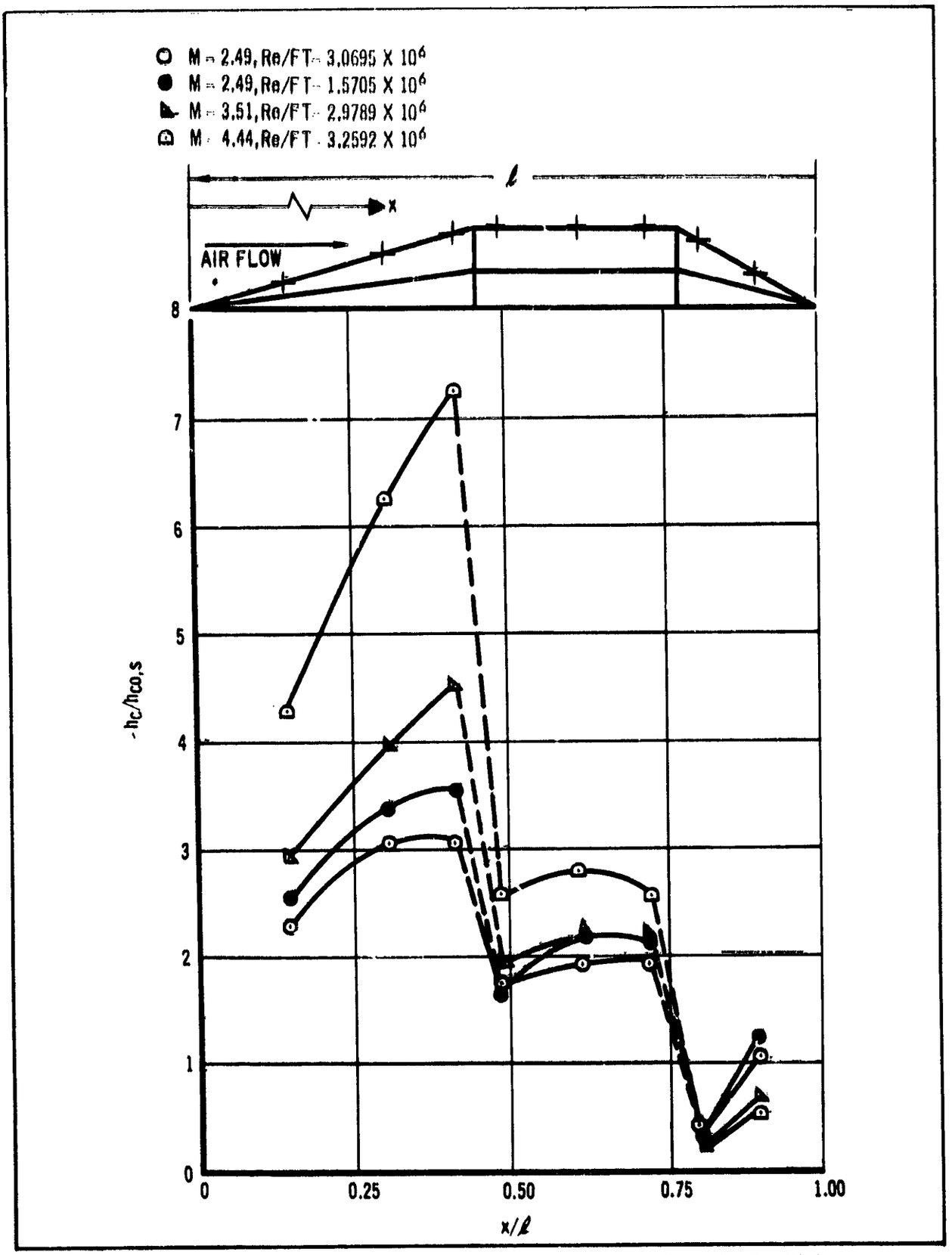

Figure 71(a). Axial Distribution of the Ratio of Model Heat Transfer Coefficient To Flat Plate Heat Transfer Coefficient on Model No. 2

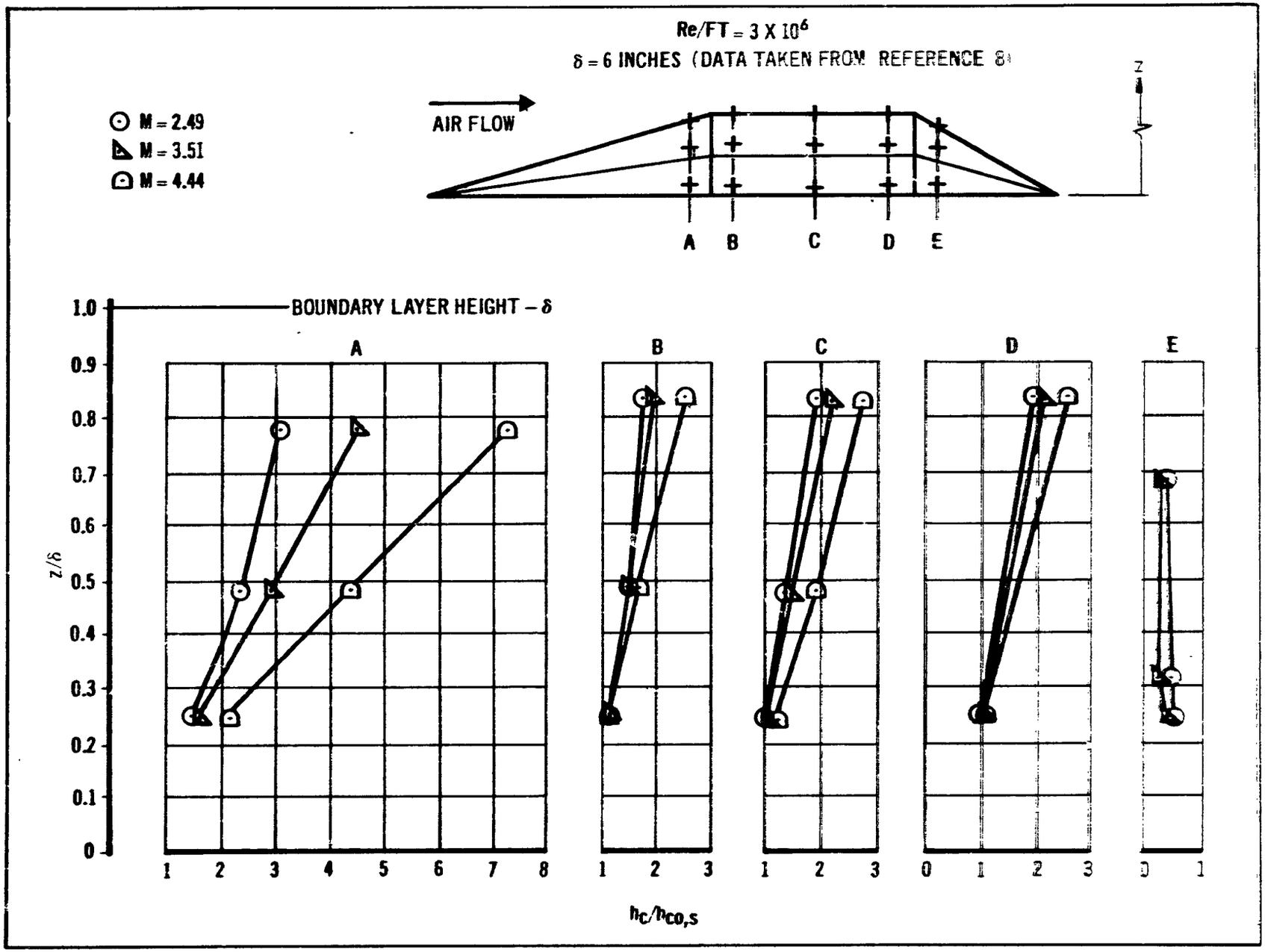

Figure 71(b). Cross Sectional Distribution of the Ratio of Model Heat Transfer Coefficient To Flat Plate Heat Transfer Coefficient on Model No. 2

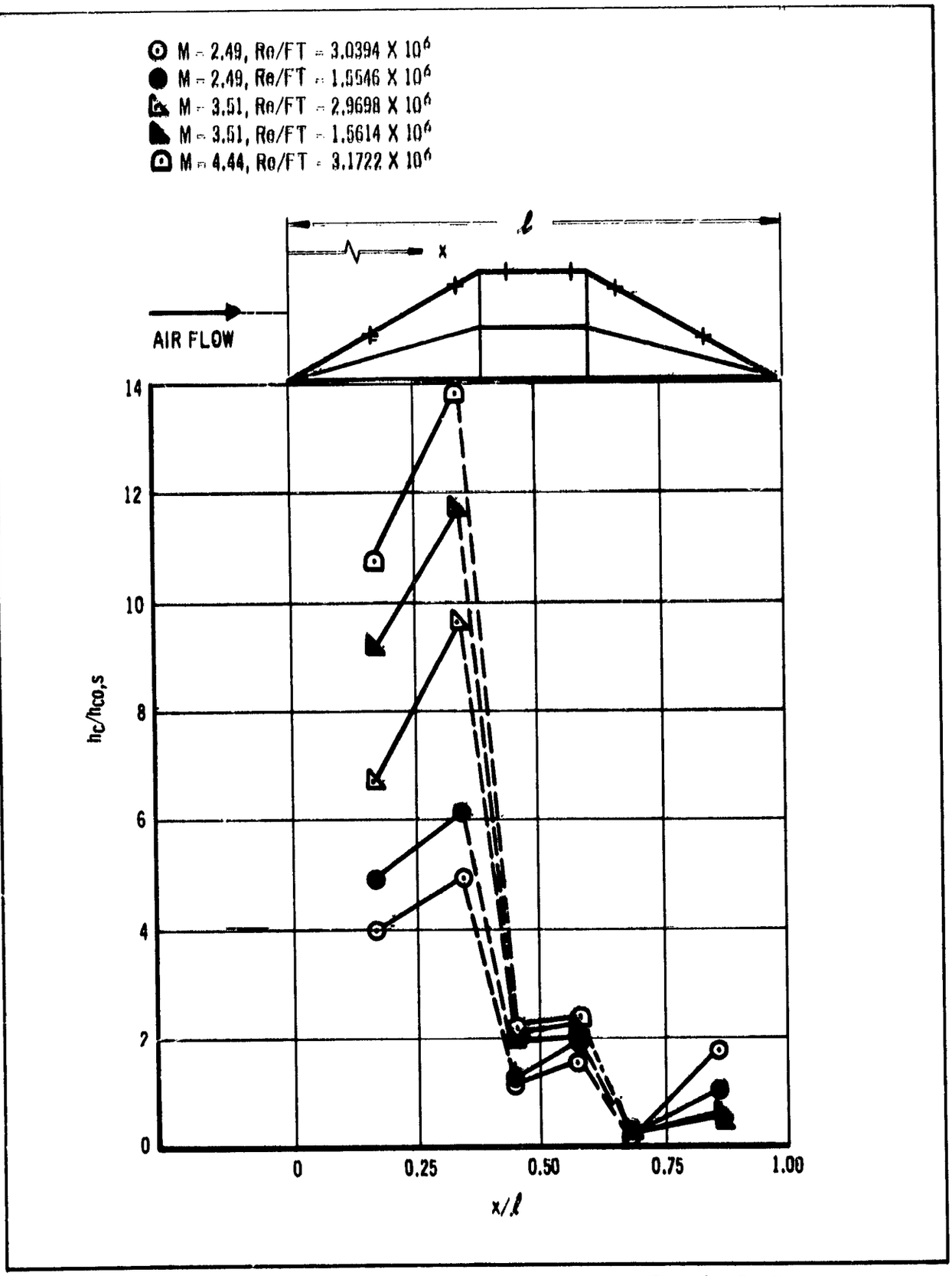

Figure 72(a). Axial Distribution of the Ratio of Model Heat Transfer Coefficient To Flat Plate Heat-Transfer Coefficient on Model No. 10

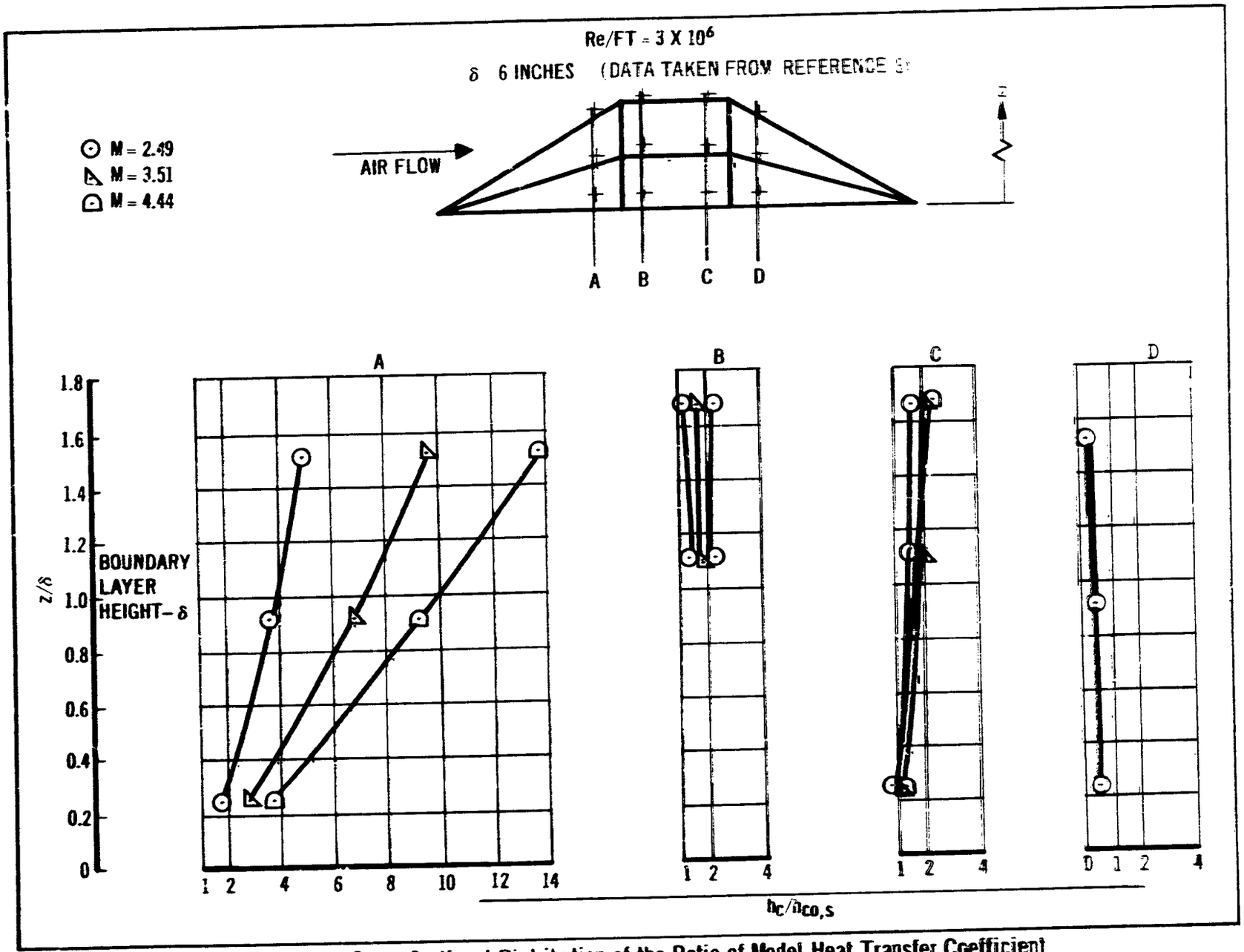

Figure 72(b). Cross Sectional Distribution of the Ratio of Model Heat Transfer Coefficient To Flat Plate Heat Transfer Coefficient on Model No. 10

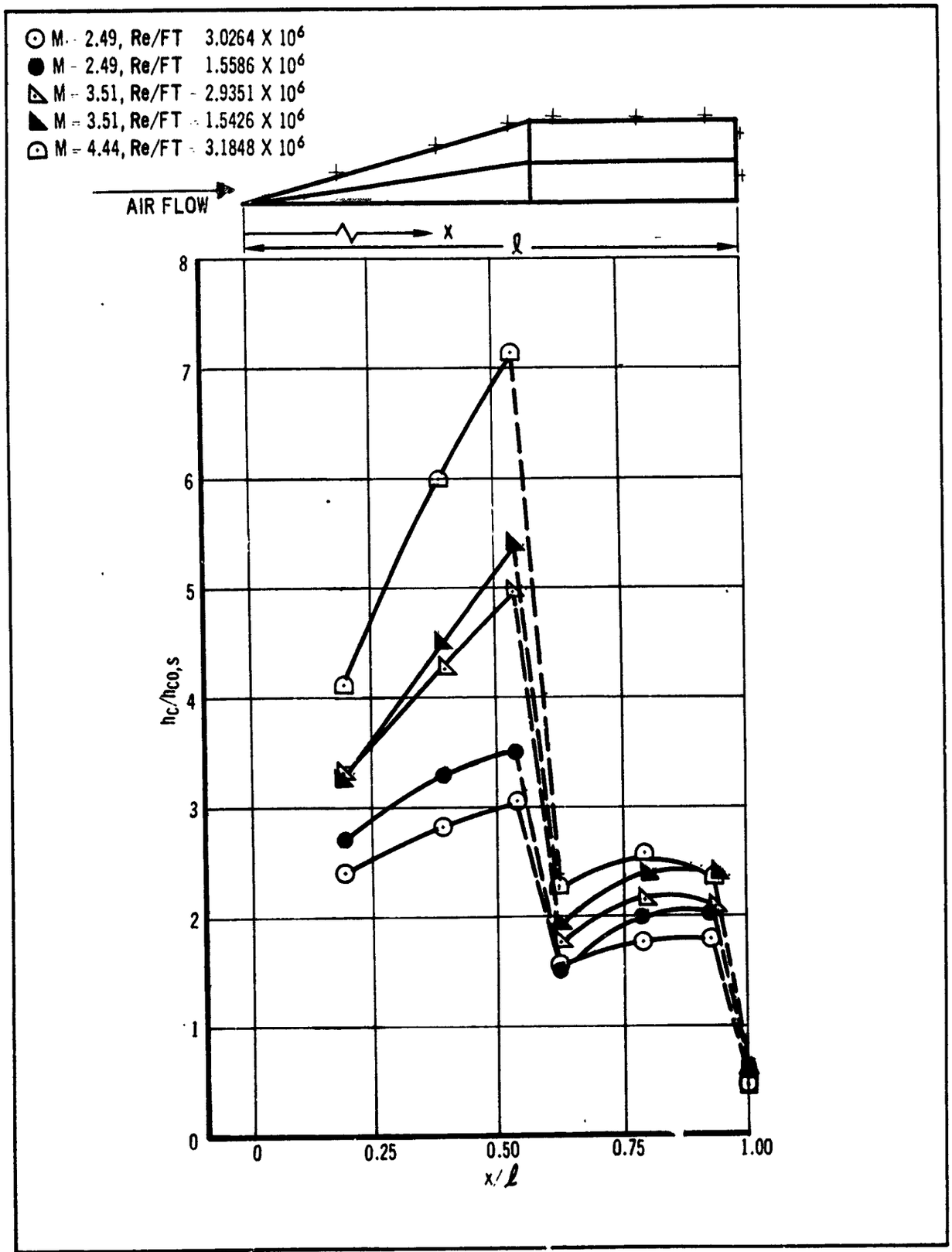

Figure 73(a). Axial Distribution of the Ratio of Model Heat Transfer Coefficient To Flat Plate Heat Transfer Coefficient on Model No. 5

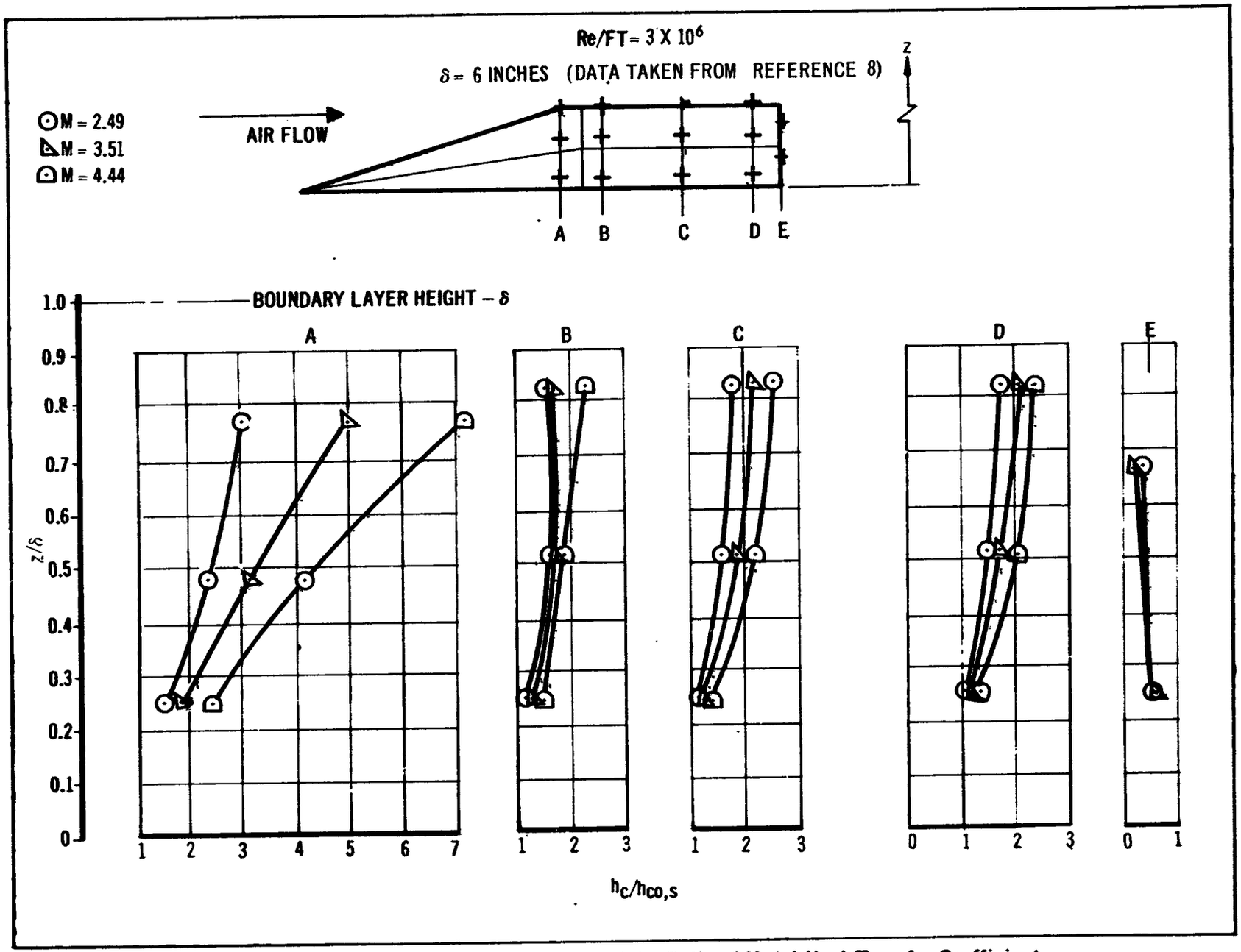

Figure 73.(b) Cross Sectional Distribution of the Ratio of Model Heat Transfer Coefficient To Flat Plate Heat Transfer Coefficient on Model No. 5

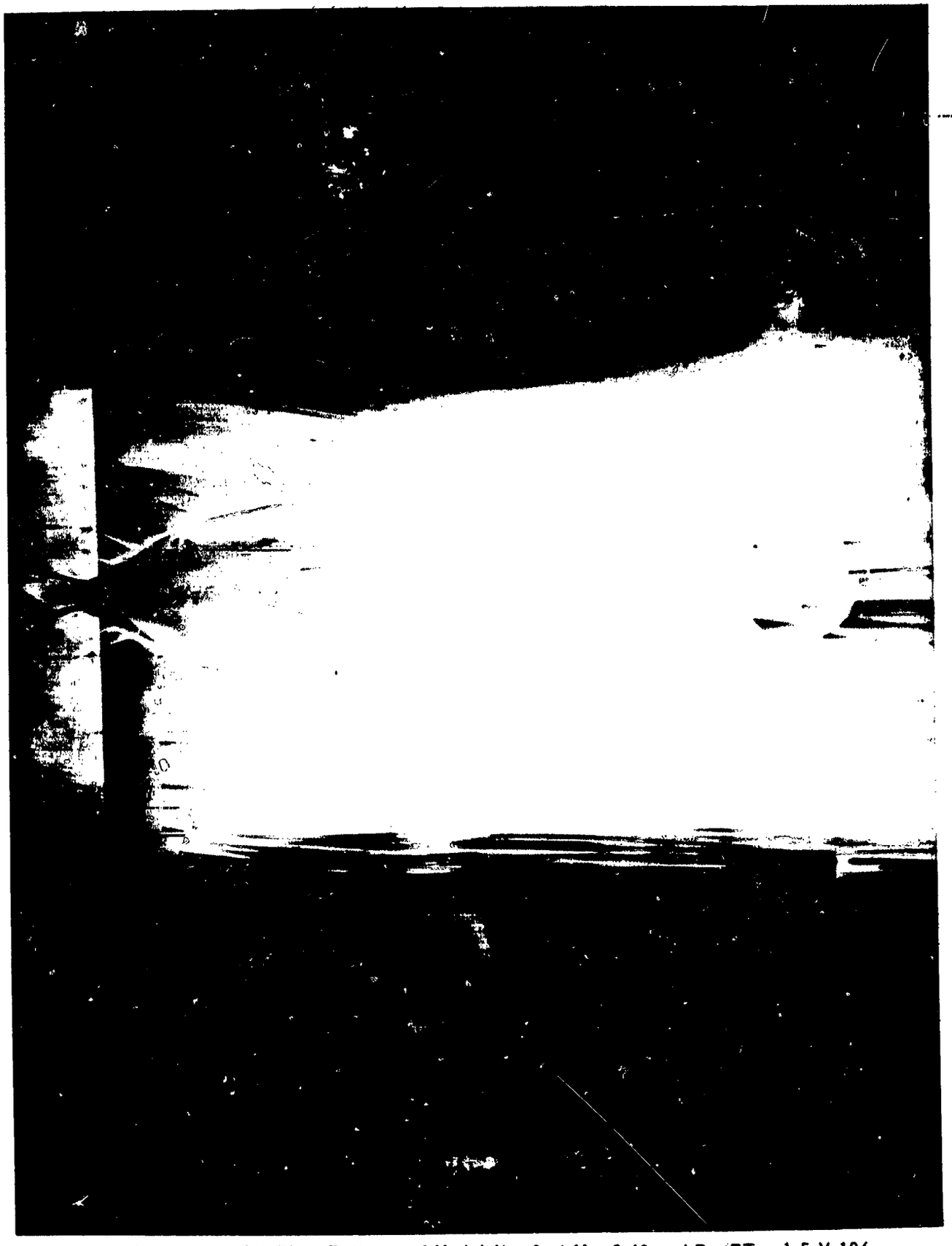

Figure 74. Oil Flow Patterns of Model No. 9 at M = 2.49 and Re/FT = 1.5×10^6

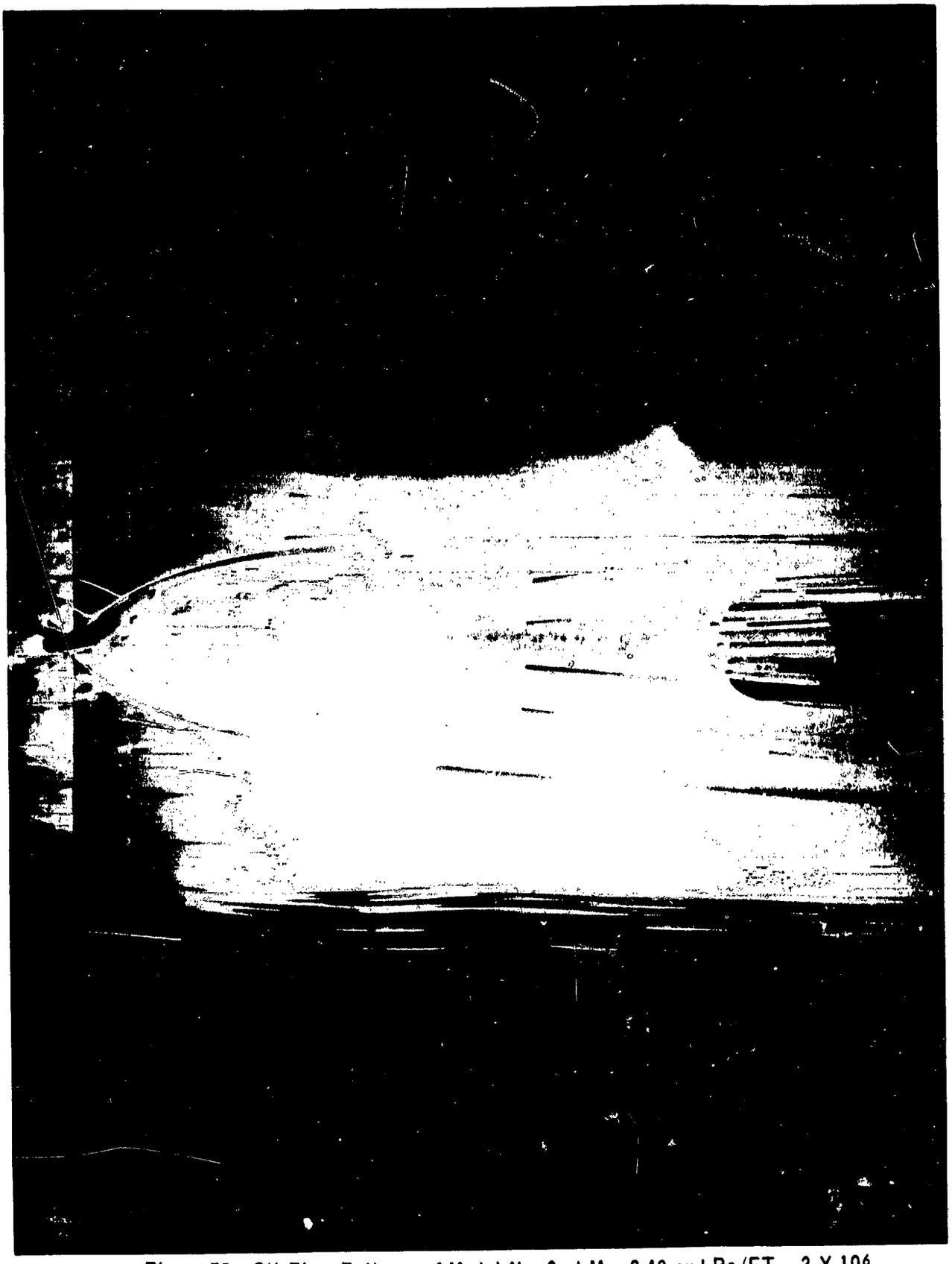

Figure 75. Oil Flow Patterns of Model No. 9 at M = 2.49 and Re/FT = 3 X 10^6

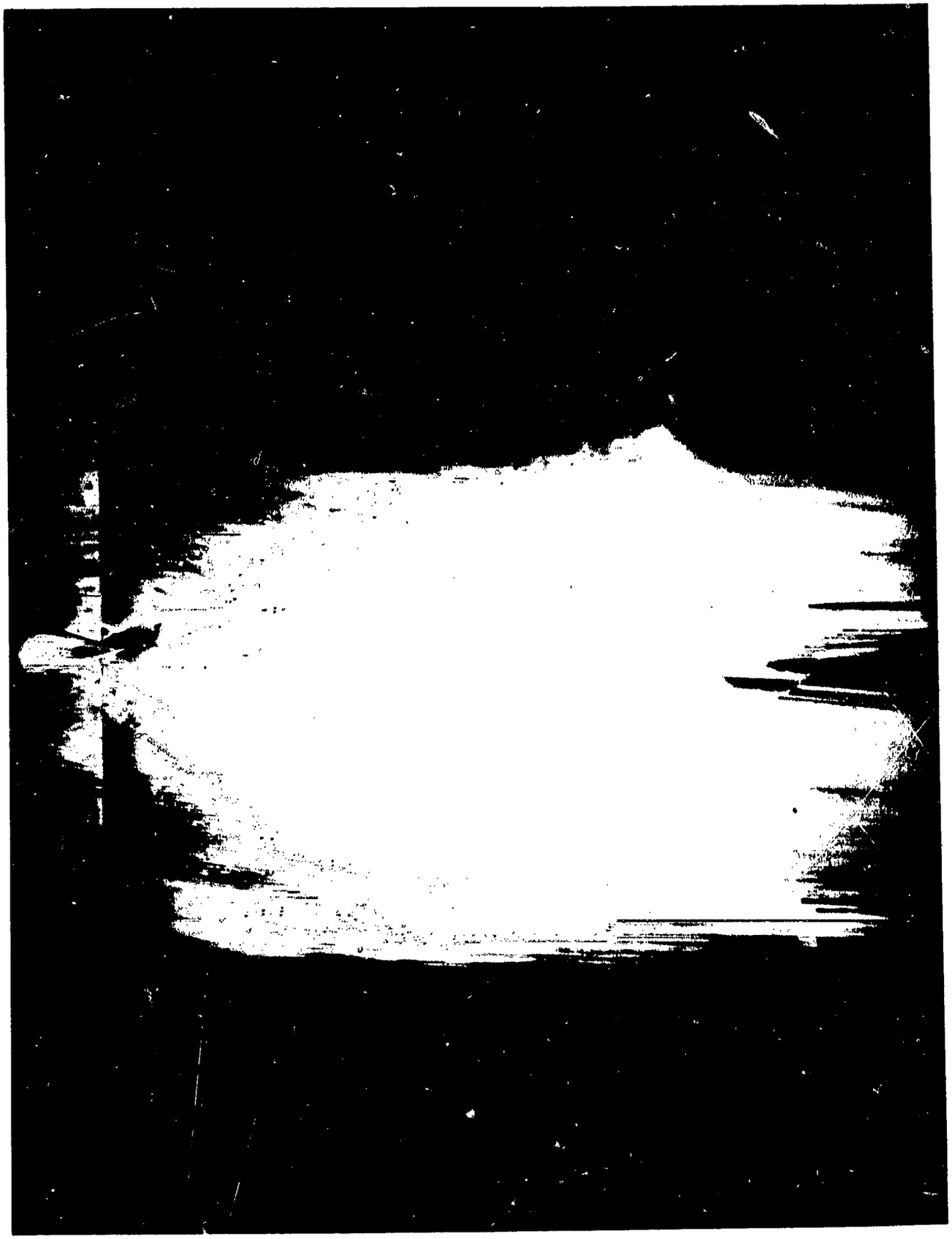

Figure 76. Oil Flow Patterns of Model No. 9 at M = 3.51 and $Re/FT = 3 \times 10^6$

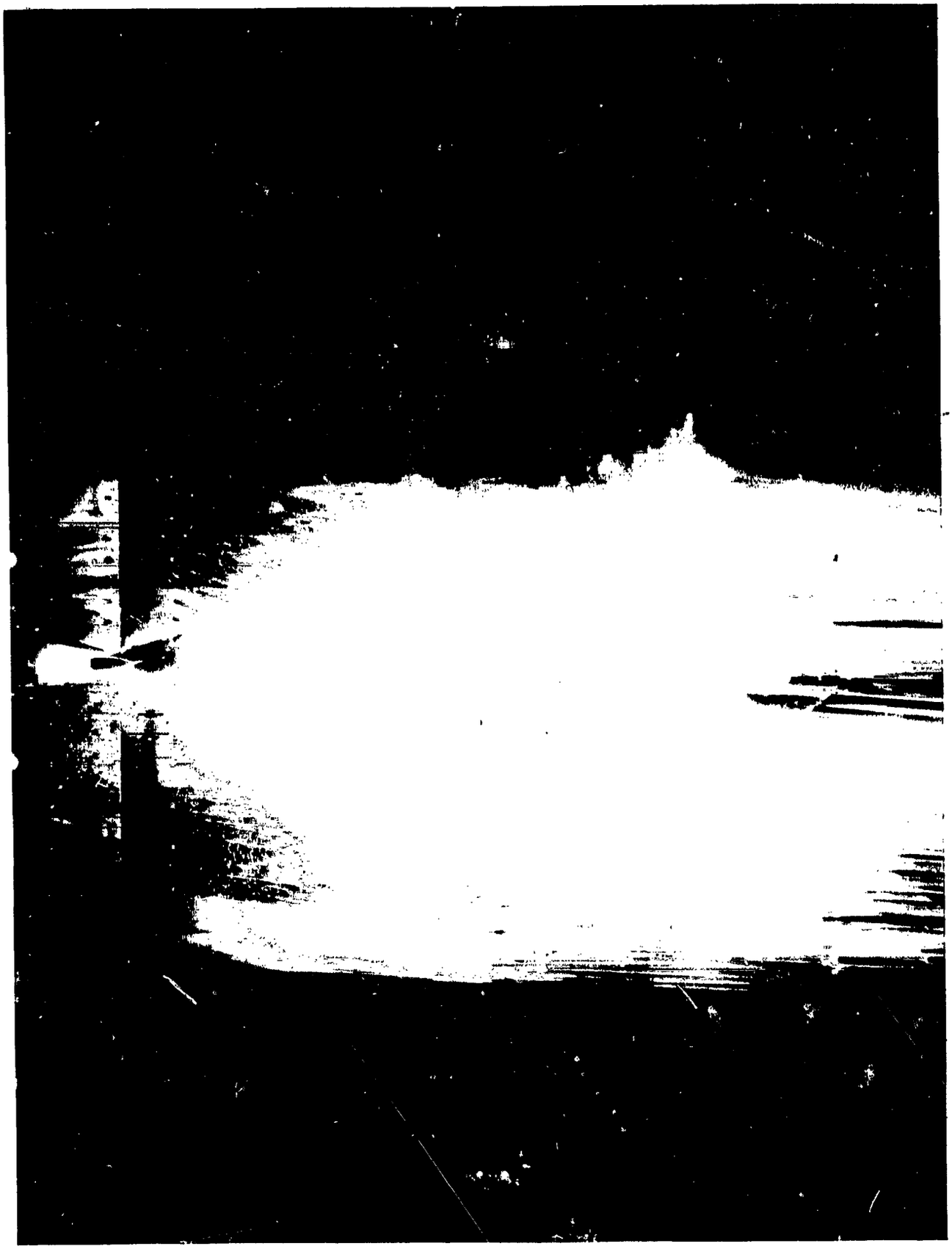

Figure 77. Oil Flow Patterns of Model No. 9 at M = 4.44 and Re/FT = 3 X 10^6

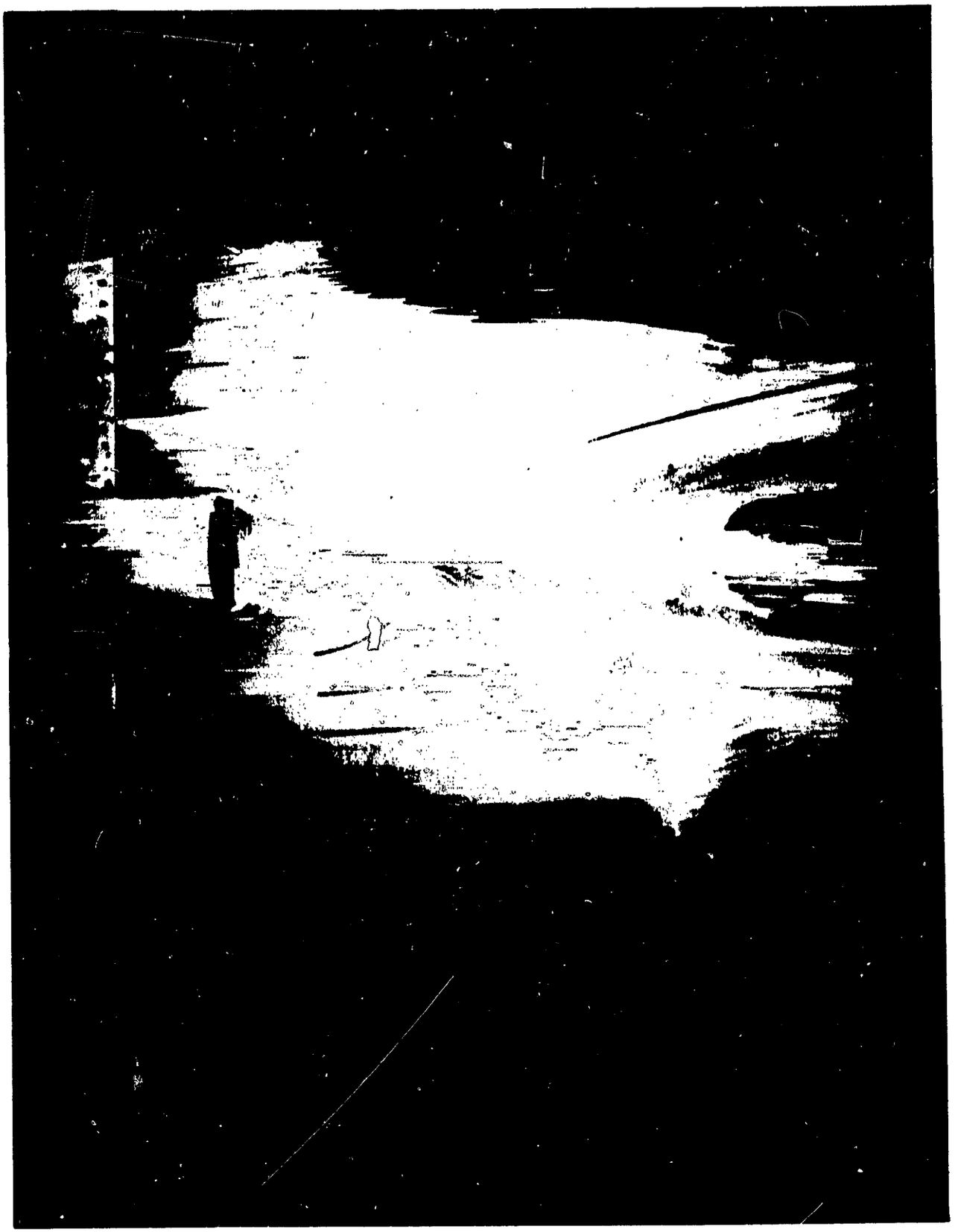

Figure 78. Upstream Oil Flow Patterns of Model No. 5 at M = 3.51 and Re/FT = 3 X 10^6

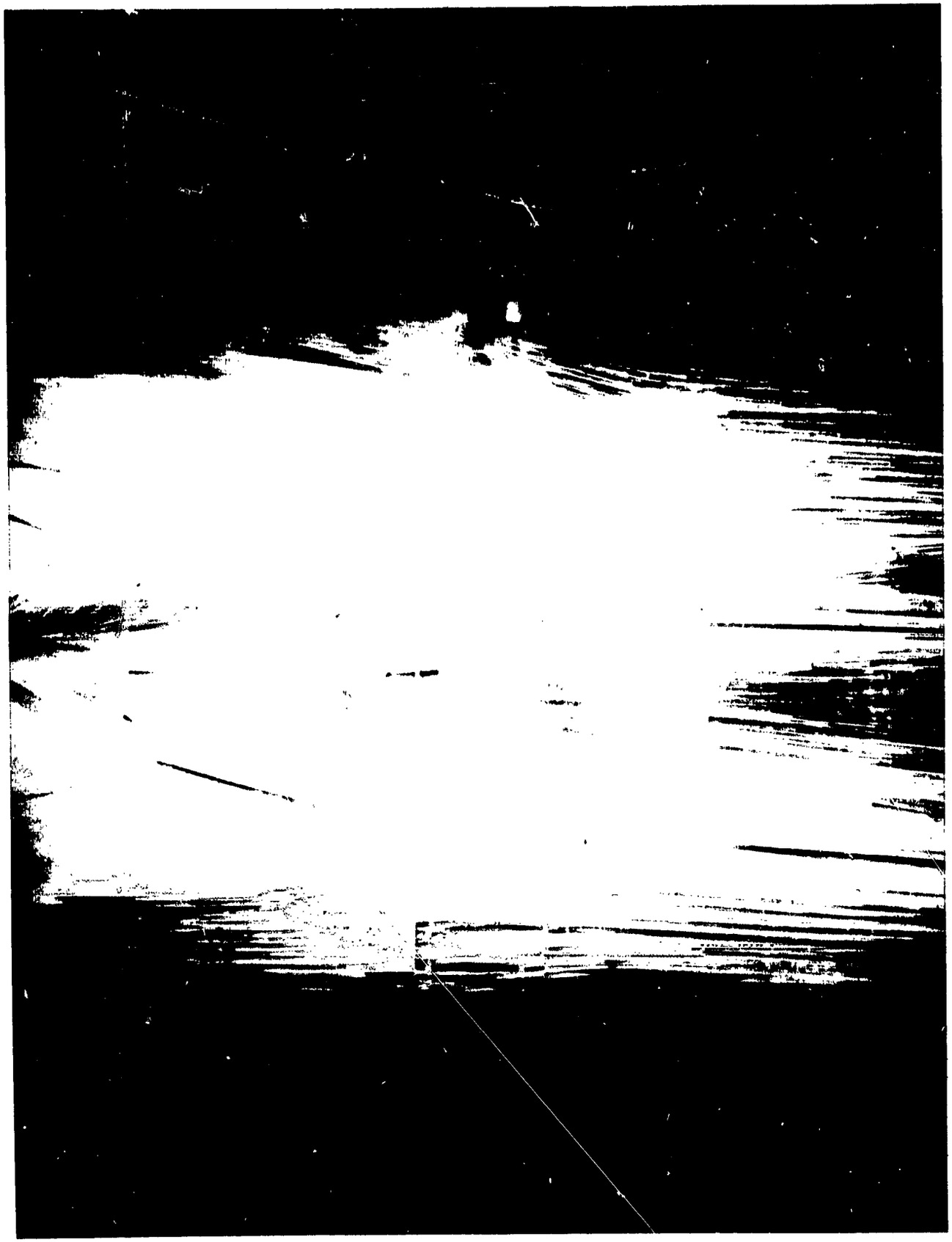

Figure 79. Downstream Oil Flow Patterns of Model No. 5 at M = 3.51 and Re/FT = 3 X 10^6

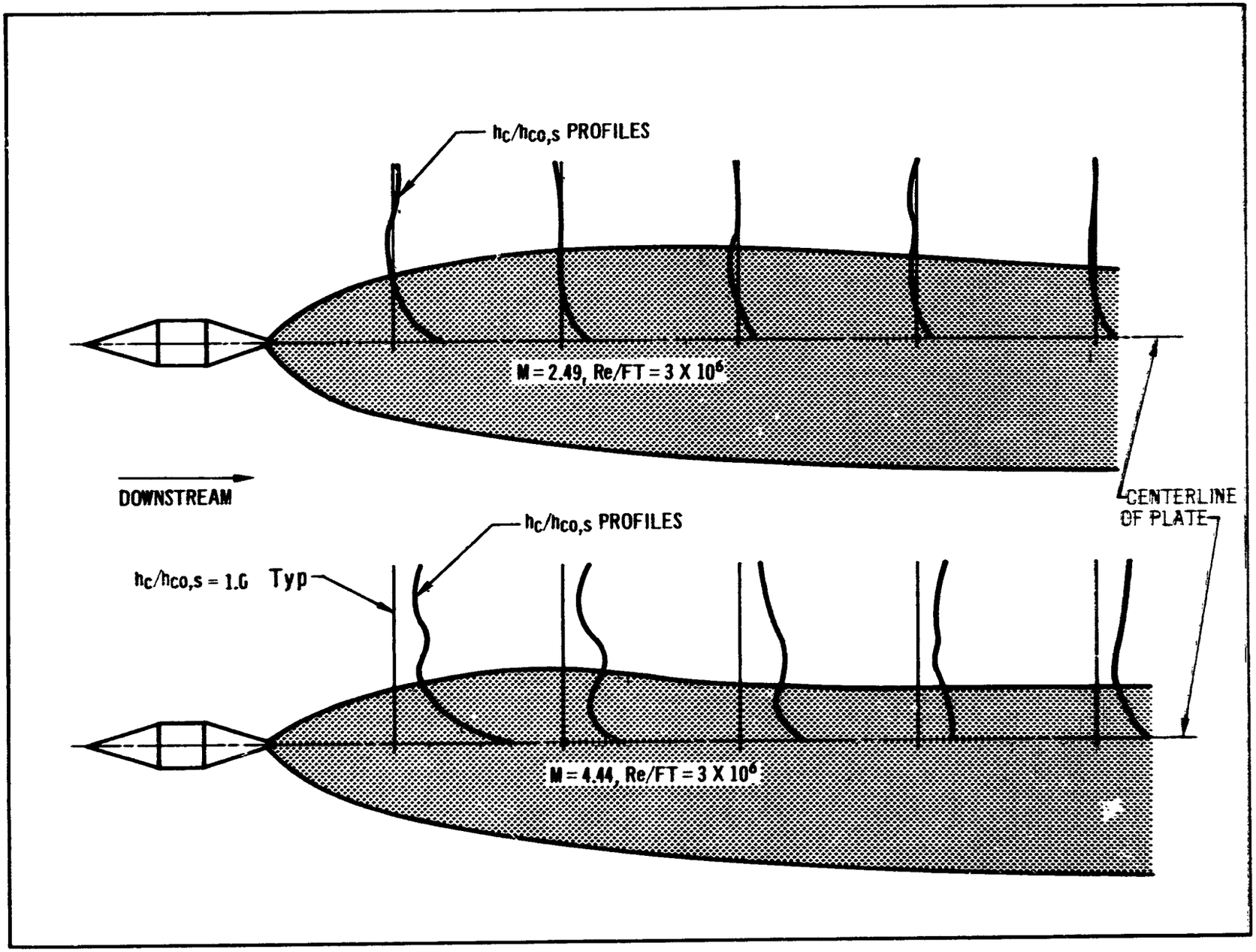

Figure 80. Lateral Heat Transfer Coefficient Ratios ($h_c/h_{co,s}$) Superimposed on Observed Oil Flow Patterns
Model No. 9

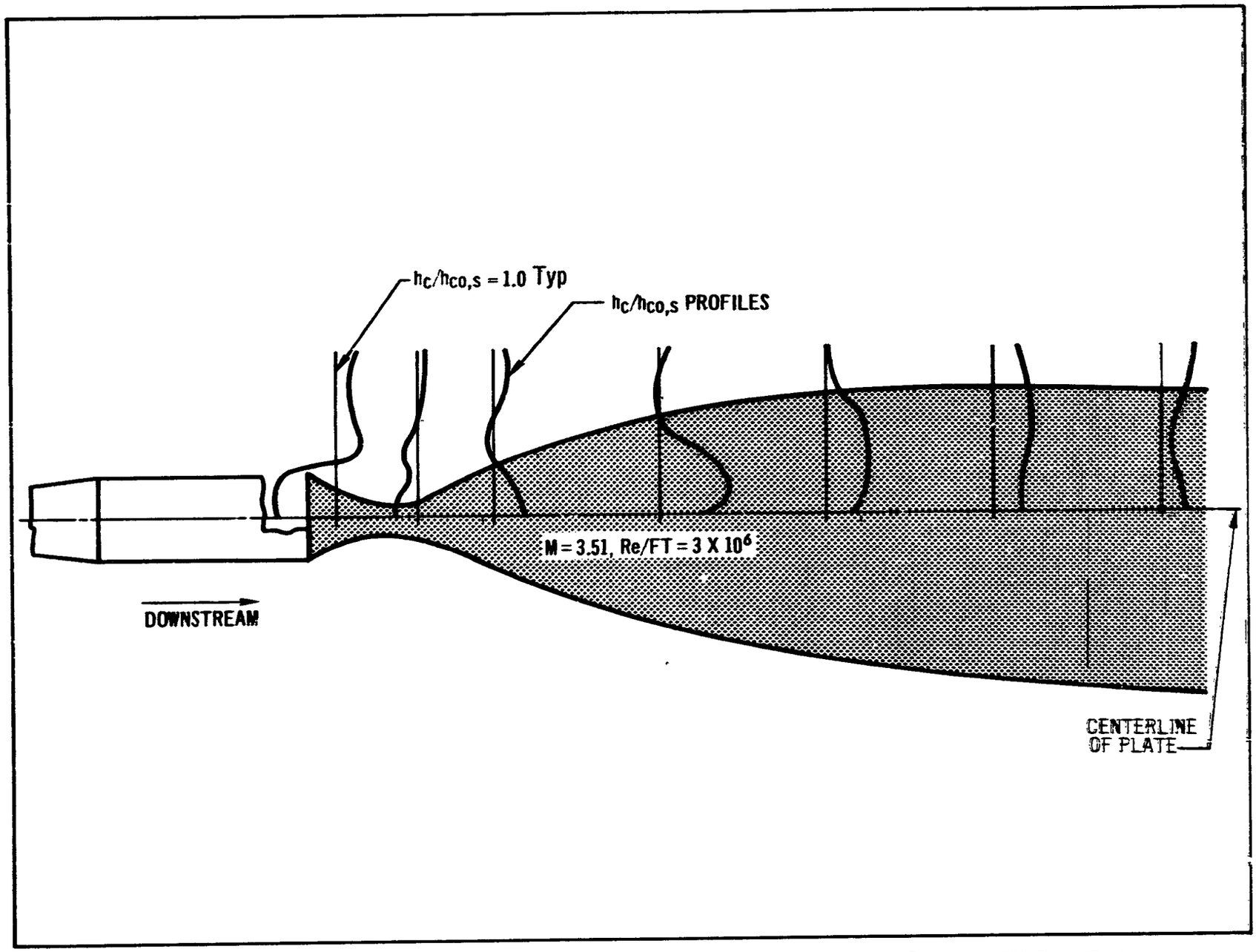

Figure 81. Lateral Heat Transfer Coefficient Ratios ($h_c/h_{co,s}$) Superimposed on Observed Oil Flow Patterns
Model No. 5

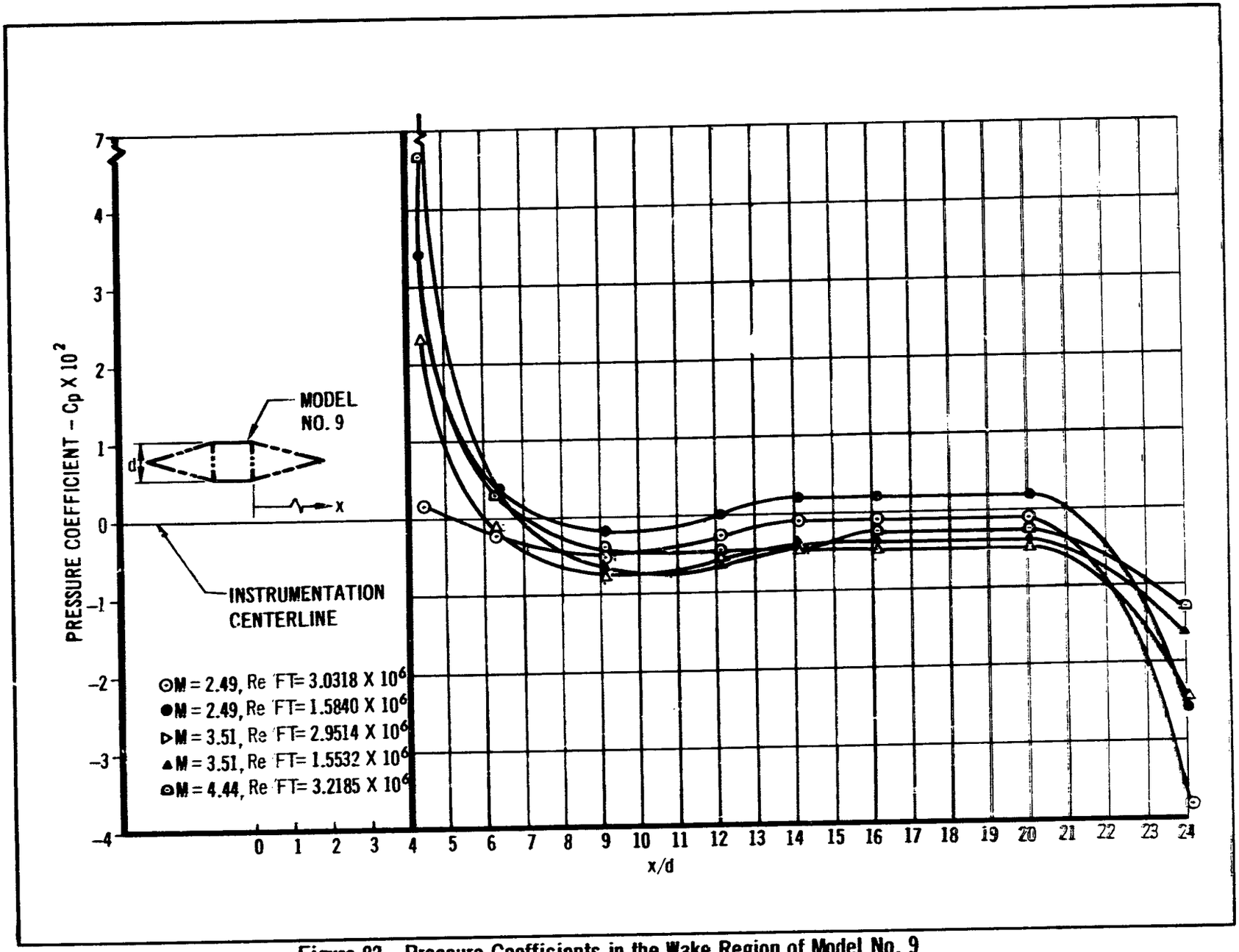

Figure 82. Pressure Coefficients in the Wake Region of Model No. 9

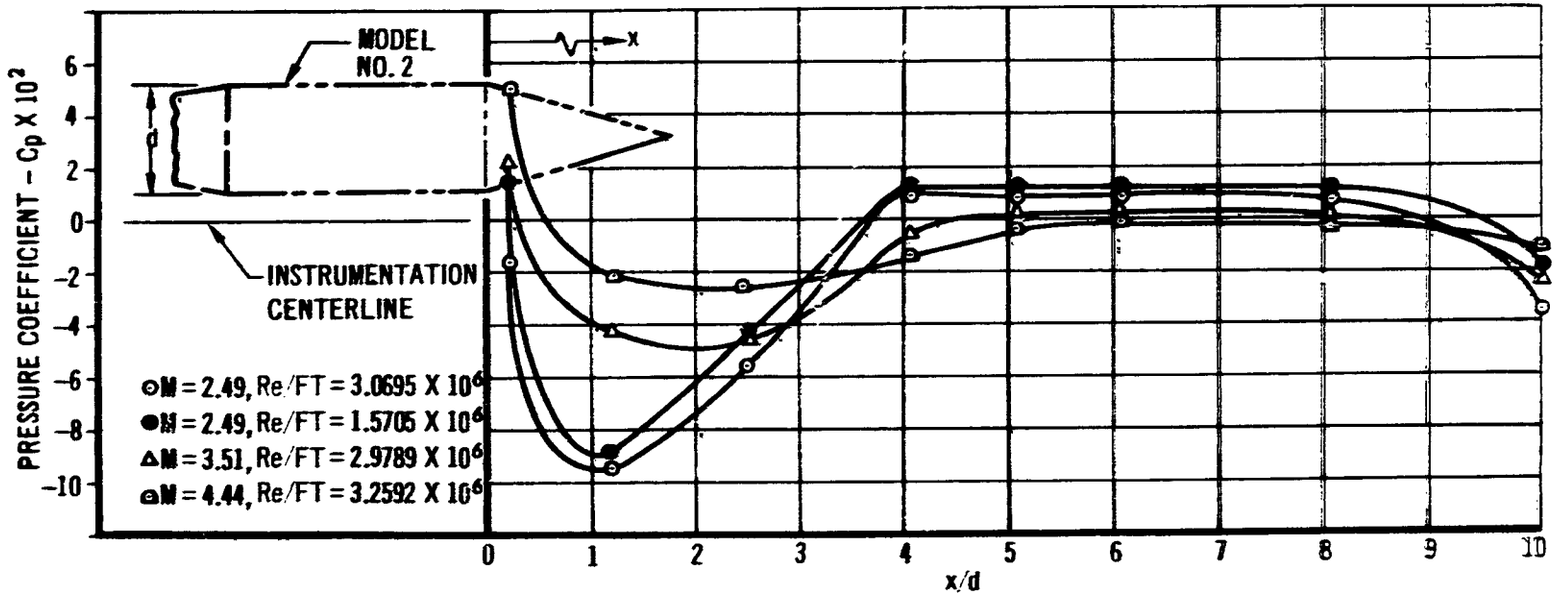

Figure 83. Pressure Coefficients in the Wake Region of Model No. 2

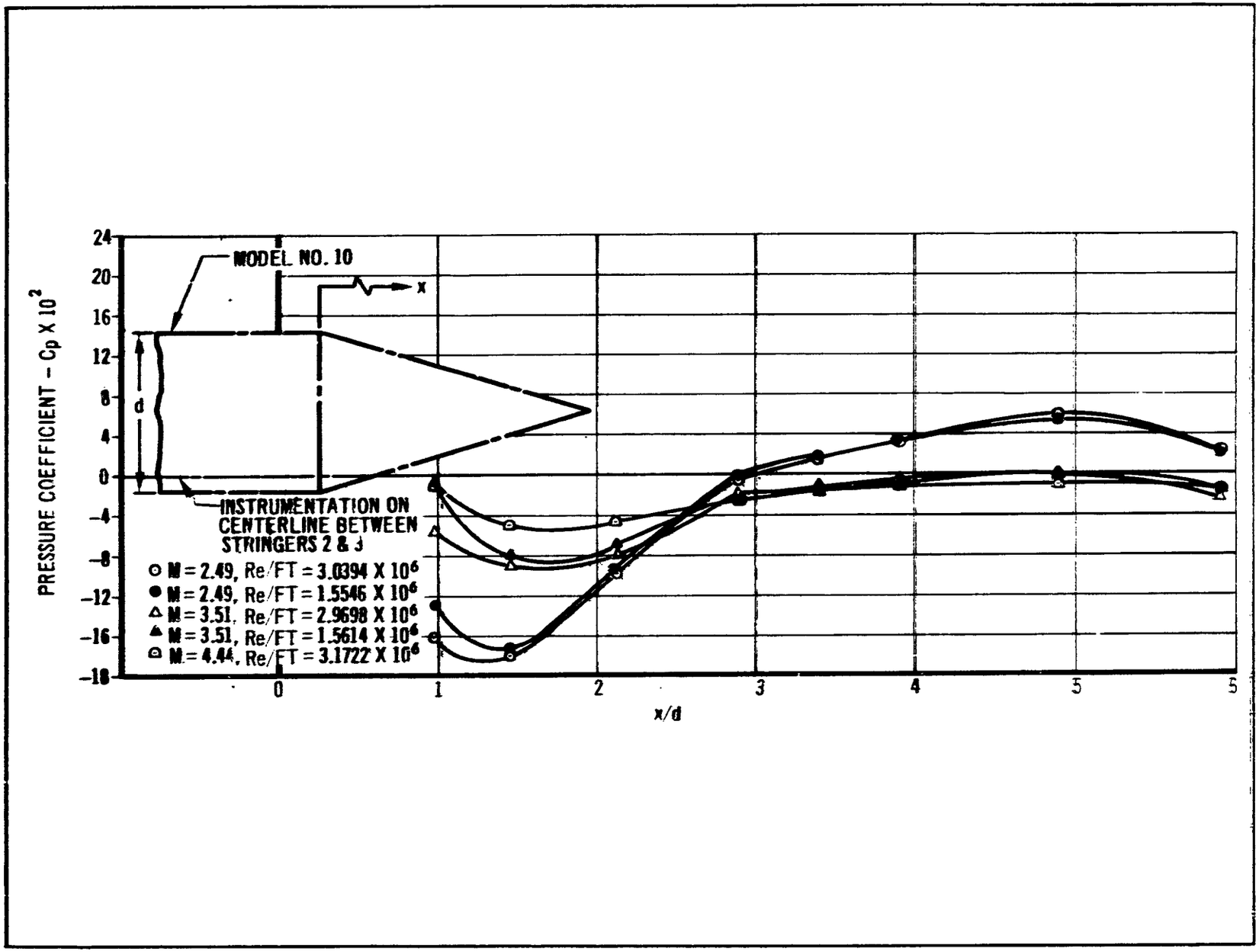

Figure 84. Pressure Coefficients in the Wake Region of Model No. 10

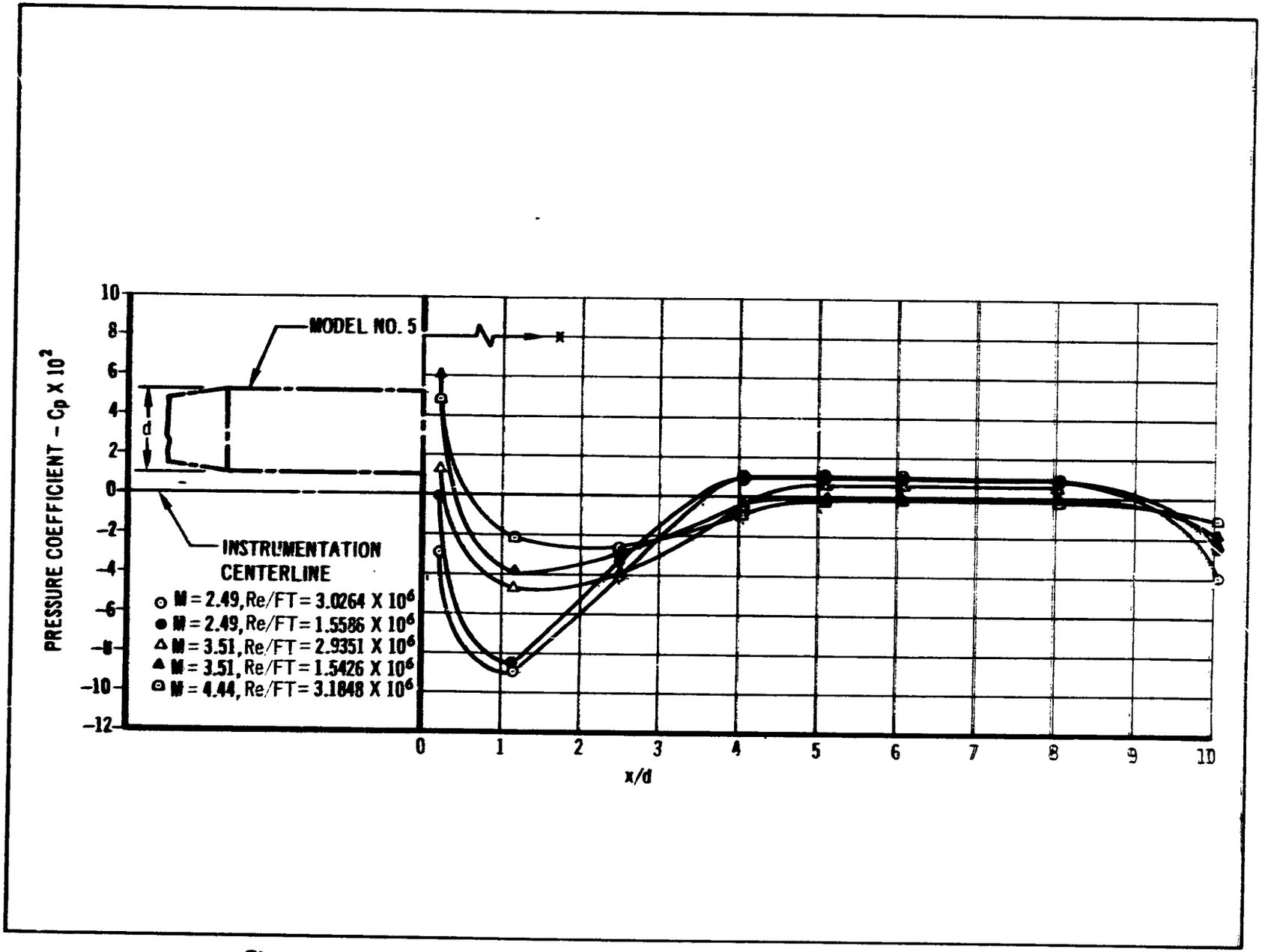

Figure 85. Pressure Coefficients in the Wake Region of Model No. 5

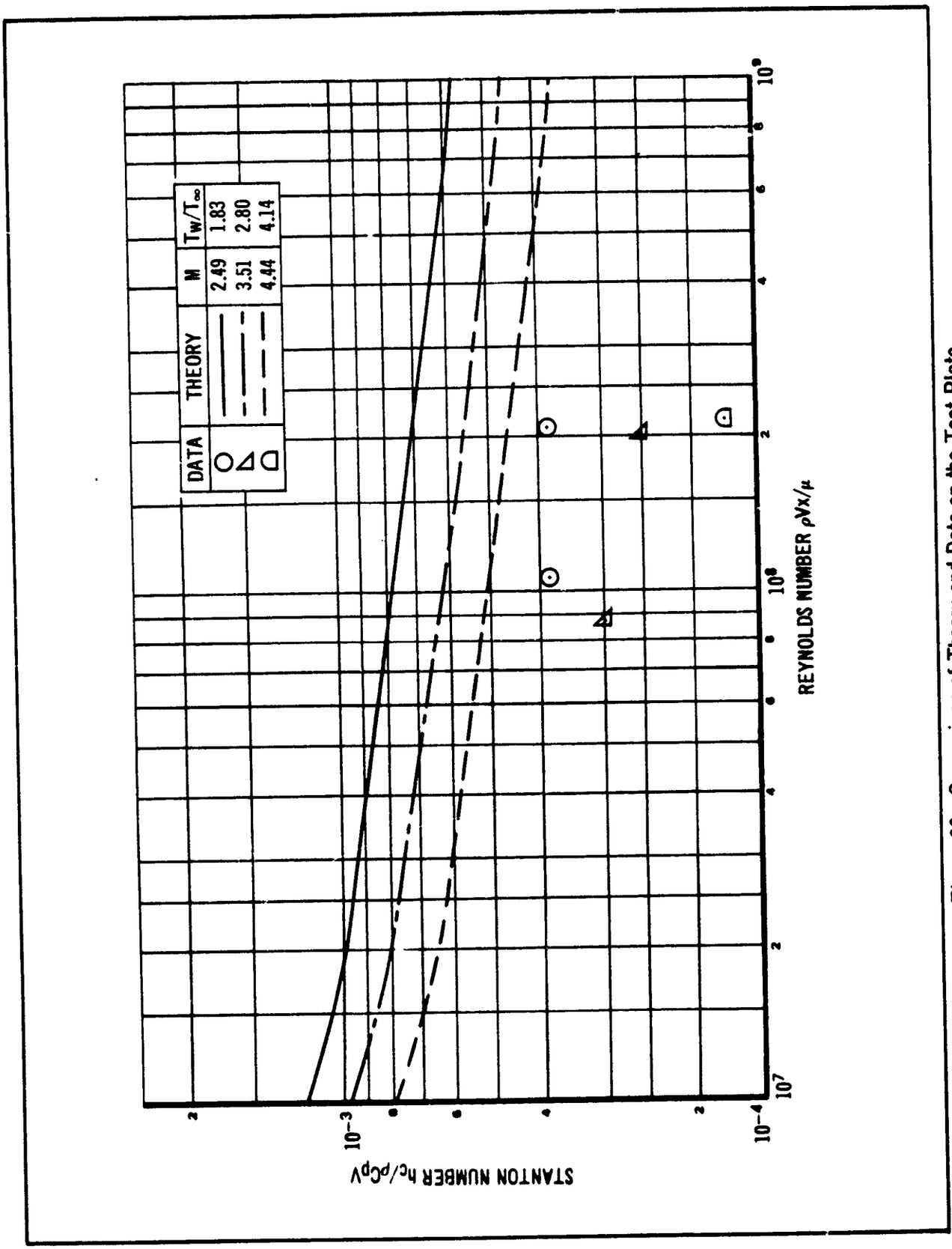

Figure 86. Comparison of Theory and Data on the Test Plate

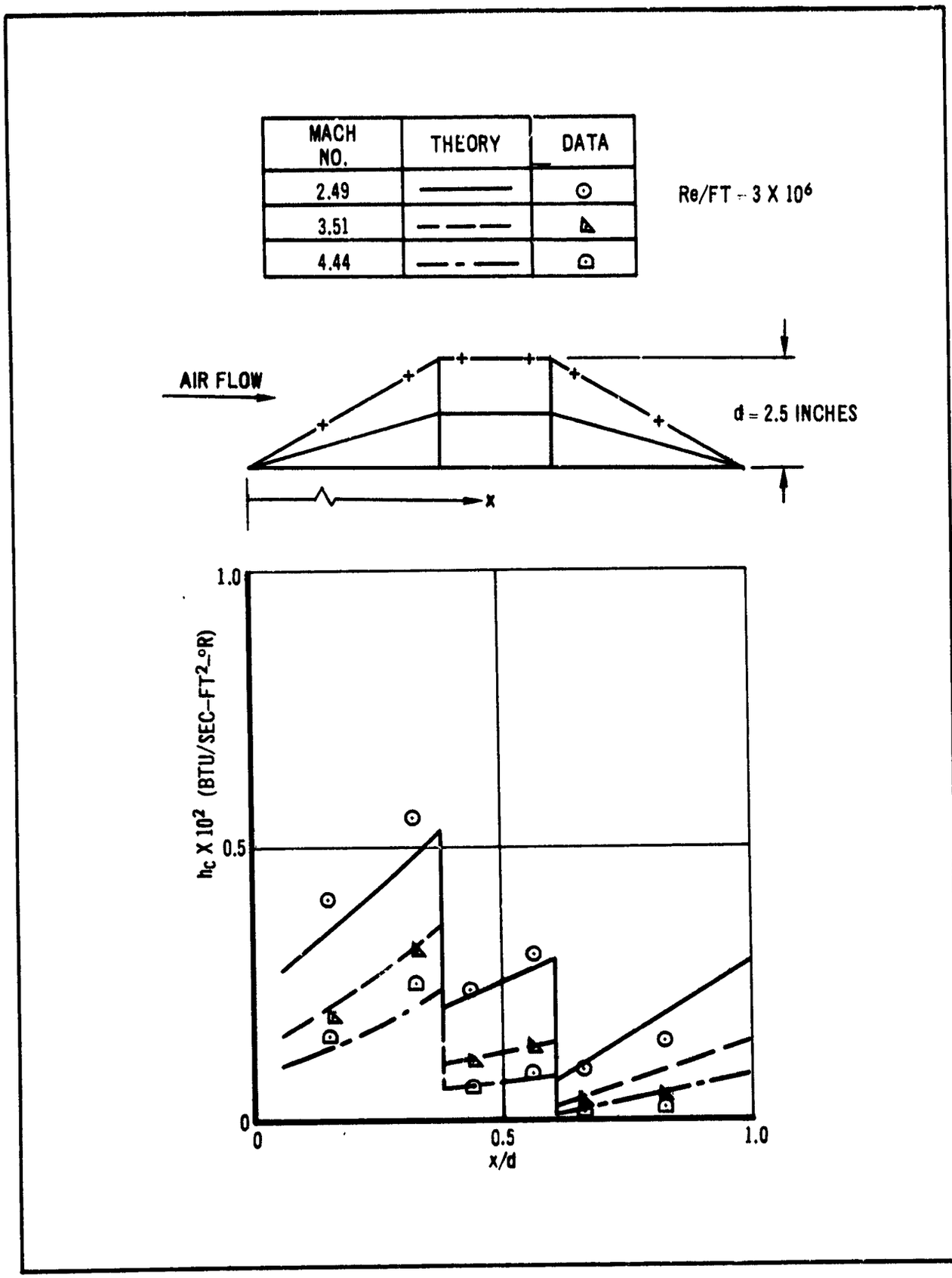

Figure 87. Comparison of Theory and Data on the Centerline Surfaces of Model No. 9

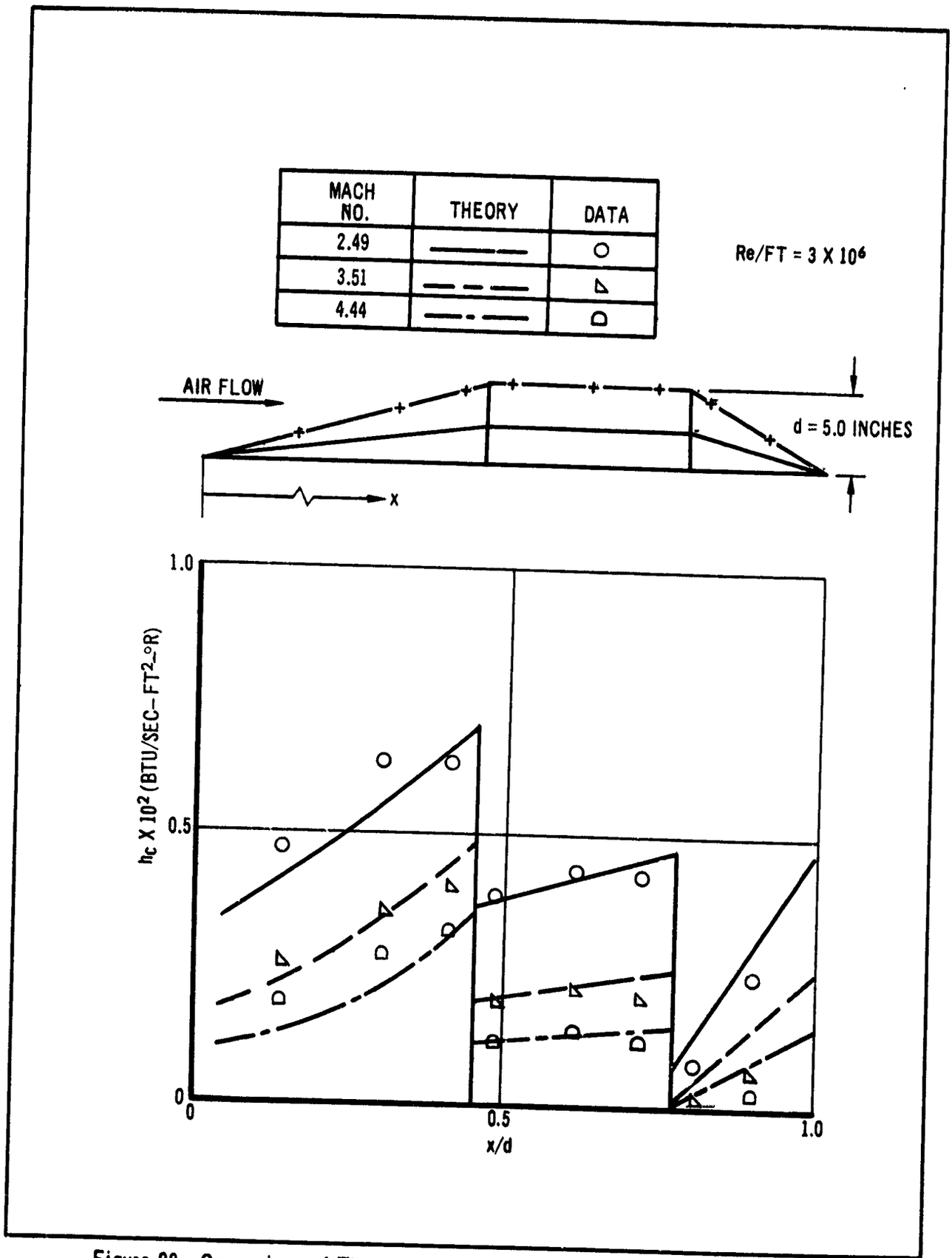

Figure 88. Comparison of Theory and Data on the Centerline Surfaces of Model No. 2

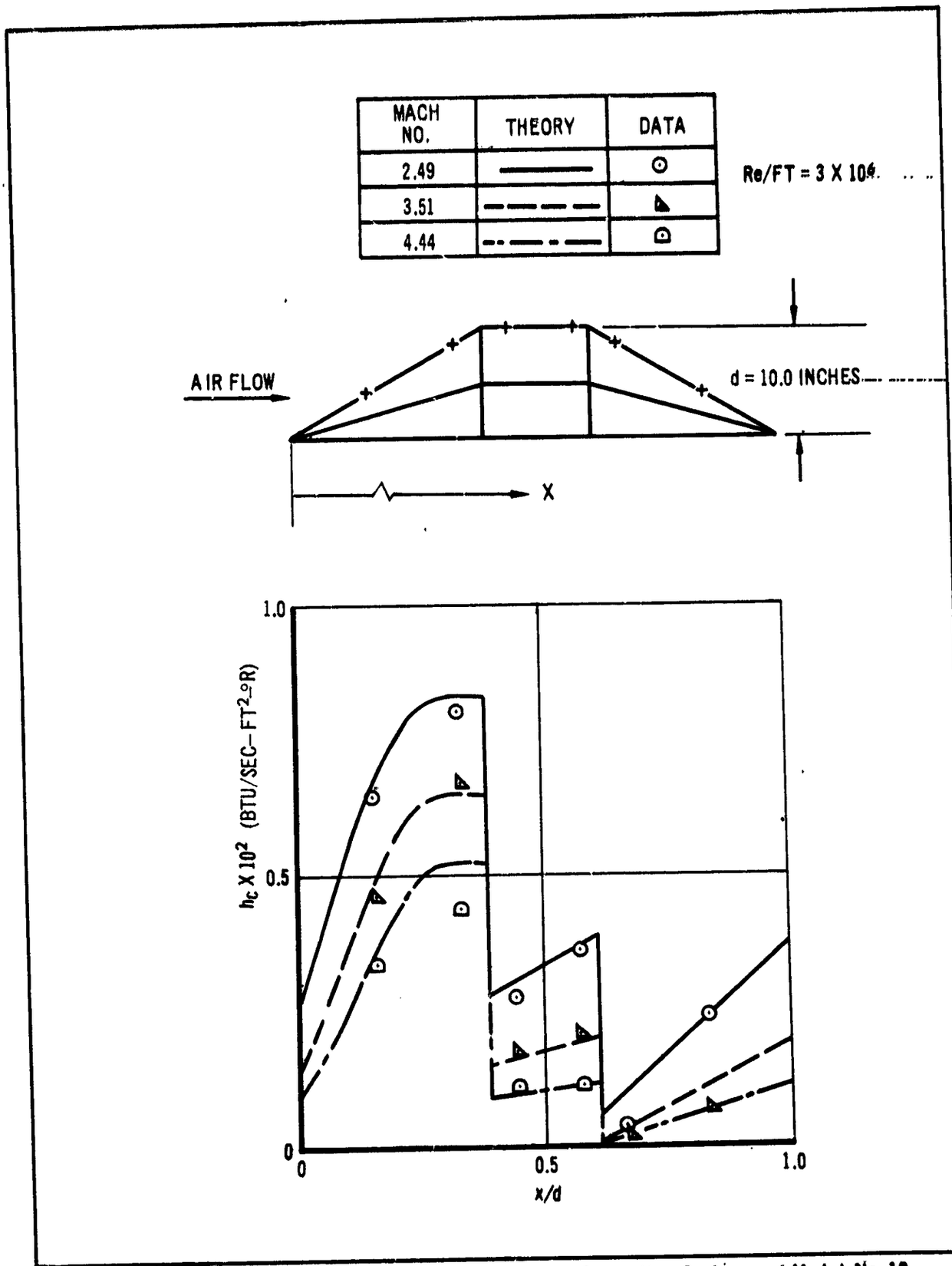

Figure 89. Comparison of Theory and Data on the Centerline Surfaces of Model No.10

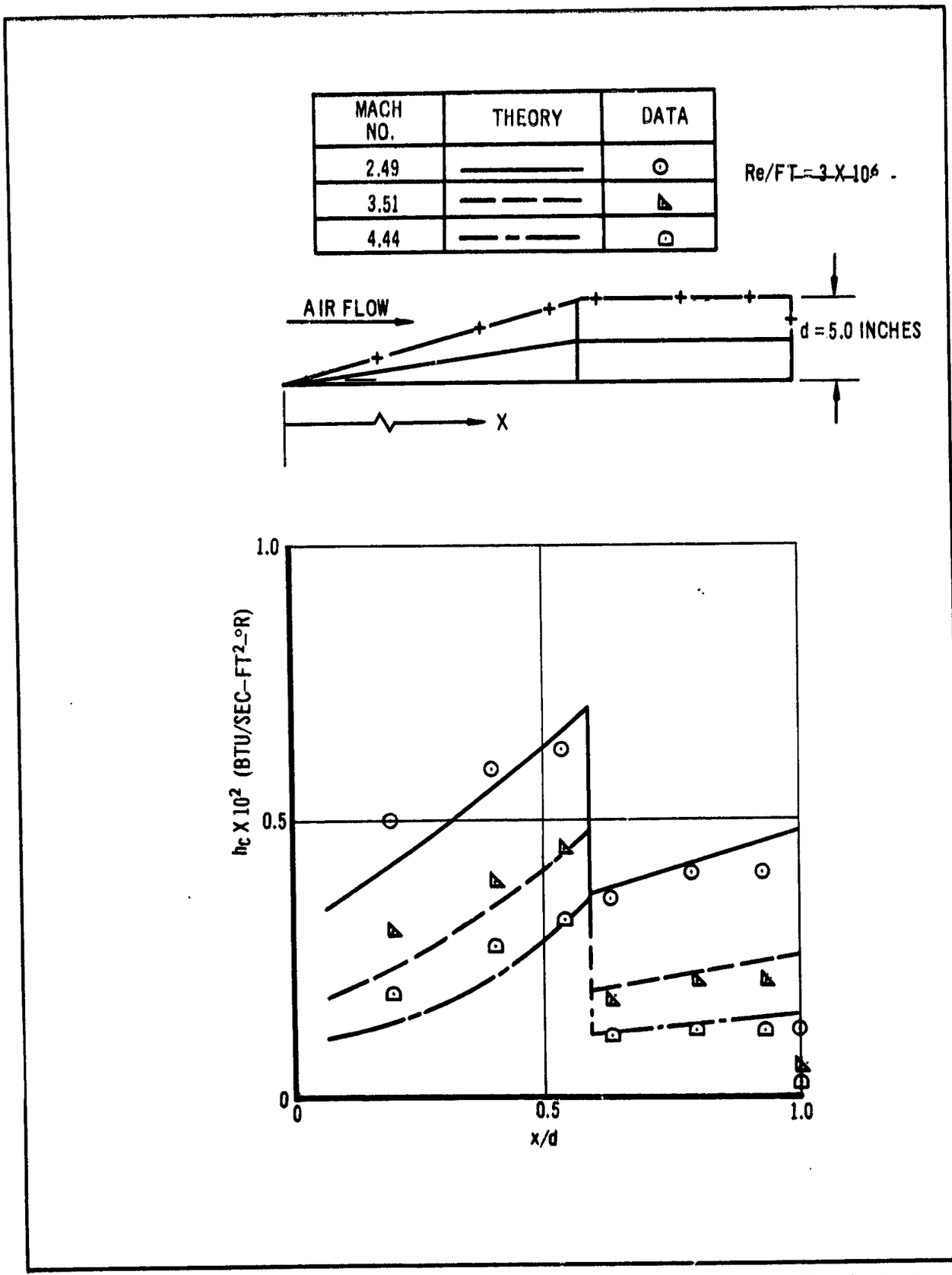

Figure 90. Comparison of Theory and Data on the Centerline Surfaces of Model No. 5

Material Properties

Nickel

Thermal conductivity	0.0136 Btu/sec-ft-^{o}R
Heat capacity	0.104 Btu/lb-^{o}R
Density	554.69 lb/ft^{3}

Stainless Steel

Thermal conductivity	0.0023 Btu/sec-ft-^{o}R
Heat capacity	0.108 Btu/lb-^{o}R
Density	501.12 lb/ft^{3}

APPENDIX (CALCULATION OF HEAT TRANSFER COEFFICIENTS)

The data were reduced by Langley Research Center using the method below. The material properties used in the computations were determined by Douglas.

Equations for Data Reduction

$$\dot{q}_{aero} = \dot{q}_{stored} + \dot{q}_{losses}$$

Neglecting losses the equation can be written:

$$h\,(T_e - T_w) = Wbc\,\frac{dT_w}{dt}$$

and by rearranging:

$$\frac{T_e}{T_o}\int_o^t T_o\,dt - \int_o^t T_w\,dt = \frac{Wbc}{h}\int_{T_{w,o}}^{T_{w,t}} dT_w$$

where $\frac{T_e}{T_o}$ is experimentally determined.

Thus

$$h = \frac{Wbc\,(T_{w,t} - T_{w,o})}{\frac{T_e}{T_o}\sum_o^t T_{of}\Delta t - \sum_o^t T_{wi}\Delta t}$$

Considering the data obtained from the previous test, the losses due to conduction were neglibible. Therefore, no conduction corrections were made on the data obtained from this test.

Equations for Data Reduction (Cont)

Symbols

W = density of skin lb/ft^3

b = skin thickness, ft

c = specific heat of skin material, $Btu/lb-^oR$

k = heat conductivity of skin, $Btu/sec-ft-^oR$

h = heat transfer coefficient, $Btu/sec-ft^2-^oR$

$\dot{q}$ = aerodynamic heat input, $Btu/sec-ft^2$

T_e = equilibrium temperature, ^oR

T_o = stagnation temperature, ^oR

T_w = model wall temperature, ^oR

X,Y = distance between adjacent thermocouples

Subscripts

o time zero, unless defined otherwise

t time greater than zero

n pertaining to thermocouple location

i at time interval